AD A048801

WIDEBAND SATELLITE OBSERVATIONS

SRI International

333 Ravenswood Avenue

Menlo Park, California 94025

June 1977

Final Report for Period 26 May 1976—31 May 1977

CONTRACT No. DNA 001-75-C-0111

APPROVED FOR PUBLIC RELEASE;
DISTRIBUTION UNLIMITED.

DDC FILE COPY

Prepared for

Director

DEFENSE NUCLEAR AGENCY

Washington, D. C. 20305

D D C

JAN 19 1978

B

REPORT DOCUMENTATION PAGE	READ INSTRUCTIONS BEFORE COMPLETING FORM

1. REPORT NUMBER	2. GOVT ACCESSION NO.	3. RECIPIENT'S CATALOG NUMBER
DNA 4399F	AD-E300 071	

4. TITLE (and Subtitle)	5. TYPE OF REPORT & PERIOD COVERED
WIDEBAND SATELLITE OBSERVATIONS	Final Report for Period 26 May 1976—31 May 1977
	6. PERFORMING ORG. REPORT NUMBER
	SRI Project 3793

7. AUTHOR(s)	8. CONTRACT OR GRANT NUMBER(s)
R. C. Livingston, C. L. Rino, M. D. Cousins, E. J. Fremouw, B. C. Fair	DNA 001-75-C-0111

9. PERFORMING ORGANIZATION NAME AND ADDRESS	10. PROGRAM ELEMENT, PROJECT, TASK AREA & WORK UNIT NUMBERS
SRI International 333 Ravenswood Avenue Menlo Park, California 94025	Subtask L25AAXHX631-26

11. CONTROLLING OFFICE NAME AND ADDRESS	12. REPORT DATE
Director Defense Nuclear Agency Washington, D.C. 20305	June 1977
	13. NUMBER OF PAGES
	90

14. MONITORING AGENCY NAME & ADDRESS(if different from Controlling Office)	15. SECURITY CLASS (of this report)
	UNCLASSIFIED
	15a. DECLASSIFICATION DOWNGRADING SCHEDULE

16. DISTRIBUTION STATEMENT (of this Report)

Approved for public release; distribution unlimited.

17. DISTRIBUTION STATEMENT (of the abstract entered in Block 20, if different from Report)

18. SUPPLEMENTARY NOTES

19. KEY WORDS (Continue on reverse side if necessary and identify by block number)

20. ABSTRACT (Continue on reverse side if necessary and identify by block number)

The Wideband Satellite (P76-5) was launched on 22 May 1976 and data have been recorded at three receiving stations since that time. The unique nature of the Wideband signals (coherent transmissions covering VHF to S-band) and the geophysically interesting locations of the receiving stations (covering auroral and equatorial latitudes) have led to a number of new and significant results. These results pertain to both scintillation phenomenology and the physics of striation formulation.

DD $^{FORM}_{1 JAN 73}$ 1473   EDITION OF 1 NOV 65 IS OBSOLETE

20. ABSTRACT (Continued)

This report presents the results of the first year of Wideband opera-
tions. Work described previously in detailed bimonthly progress reports
is only summarized here. Emphasis in this report is placed on aspects not
previously described, including: (1) evidence for a geometrical scintilla-
tion enhancement due to east-west sheet-like irregularity structures in the
auroral zone; (2) spaced-receiver measurements of the diffraction pattern
anisotropy and apparent drift motion; (3) total electron content measure-
ments of the poleward boundary of the ionospheric trough; (4) characteris-
tics of equatorial scintillations, particularly the gigahertz scintillation
that develop during extremely active periods; and (5) results from the
equatorial scintillation campaign conducted in Peru during March 1977.

Using the Wideband data base with theoretical work and systems
analysis, it ultimately should be possible to develop a self-consistent
model relating a simple parameterization of the irregularity structure
and strength to the observed phase and amplitude scintillations.

PREFACE

The success of an extensive field experiment, such as Wideband,
depends critically on the support personnel who operate and maintain
the field stations, assist in processing and organizing the data, and
help in maintaining communication. We therefore gratefully acknowledge
the contributions of the engineers and programmers: R. Long, R. Winkelman,
G. Durfey, J. Moore; the contributions of the site personnel: C. Code,
R. Evans, H. Jacobs, D. Lee, R. March, S. Matthews, R. Panton, L. Porath,
G. Roach, R. Schledewitz, and J. Sheldon; the Instituto Geofisico del
Peru, who operate the Ancon station; B. Cotts, who has processed the
data and maintained our data library; and the clerical support of
J. Finck and C. Schlesing.

1

CONTENTS

ILLUSTRATIONS

4

I   REPORT SUMMARY AND CONCLUSIONS

This report summarizes the results obtained during the first year of data analysis and operations after the launch of the Wideband satellite (P76-5) on May 22, 1976.

The unique capability of the Wideband satellite to measure phase scintillation as well as amplitude scintillation at a number of widely spaced frequencies has led to a number of significant results pertaining to both the scintillation phenomenology and the physics of striation formation. A brief summary of these results is given below:

(1) Gcneral Results

- Ionospheric radio-wave scintillation is dominated by large but slowly varying phase scintillation that can be prominent even when there is essentially no associated amplitude scintillation. Thus, significant phase scintillation can be and often is present under conditions of very weak fading; however, such events seem to be confined to the auroral zone.

- The phase scintillation directly reflects the electron density irregularity structure integrated along the propagation path to scale sizes at least as small as 1 km at VHF. (For smaller scale sizes, diffraction effects must be taken into account.) For the scale sizes that are essentially unaffected by diffraction, the phase scintillation varies linearly with wavelength when corrected for the finite S-band reference frequency.

- The power spectral density of the phase scintillation has the power-law form, Tf^p, from the high-frequency point where the phase-scintillation power falls below the noise level to the lowest frequencies that are unaffected by the detrending operation ($f \gtrsim 0.1$ Hz). Spectral index values have been observed in the range $-4 < p < -2$, with the most commonly observed values lying between -3 and -2.5. The variations reflect genuine changes in irregularity structure that possibly result from differing physical mechanisms.

(2) Auroral Zone Results

- The auroral zone scintillation is characterized by very large phase excursions. Phase excursions in excess of 1 rad over periods of less than 10 s are often observed at L-band. Saturated VHF scintillation ($S_4 \sim 1$) generally accompanies propagation through active aurorally distributed regions. The spectral index, p, for the auroral phase scintillation is highly variable, with $p < -4$ occasionally observed.

- Prominent isolated scintillation enhancements are present in $\sim 80\%$ of the nighttime passes taken at Poker Flat. When these events are observed poleward of the TEC boundary, they can be completely explained as a geometrical enhancement due to field-aligned, sheet-like structures oriented in the east-west direction. When the enhancements occur at the TEC (total electron content) boundary, they cannot be explained as a geometrical effect occurring on an undeviated ray path.

- Weak phase scintillations are typically present in the region of the high-latitude plasma trough. However, local scintillation enhancements have been observed for these cases only when the propagation path comes within 10° of the magnetic zenith. Thus, in the plasma trough, the irregularities are evidently rod-like with no significant east-west elongation.

- Direct anisotropy measurements using the spaced-receiver system show an east-west elongation of the field structure associated with the aforementioned scintillation enhancements. A sheet model with a 10:10:1 elongation can explain both the elongation and orientation of the diffraction pattern as well as the very large pattern velocity shears that are measured.

- The high-latitude nighttime TEC data show a steep increase that is identified as the poleward boundary of the high-latitude plasma trough. During undisturbed passes the boundary is colocated with the equatorward edge of the diffuse aurora as identified in simultaneous Chatanika radar data. The boundary location also shows a simple dependence on local magnetivity activity as indicated by College, Alaska, magnetometer data.

(3) Equatorial Results

- The equatorial scintillation data show a pronounced seasonal dependence with activity peaks occurr during the local summer months. During the disturbed periods, there is evidence of anticorrelation with global magnetic activity.

8

- For a given level of amplitude scintillation at the equatorial stations, there is substantially less associated phase scintillation when compared to auroral zone data showing the same level of amplitude scintillation. This can be explained if the equatorial irregularities develop at higher altitudes than the auroral irregularities, which is very likely to be the case. Nonetheless, there is evidence of a systematic flattening of the spectra near the equator, which also acts to produce more amplitude scintillation for a given level of phase scintillation.

- During active periods, extremely intense scintillations often develop that persist into the gigahertz frequency range. In most of these events there is a definite flattening of the phase spectrum with increasing perturbation intensity. Indeed, spectral index values of $p > -2$ are observed in most of these events. Moreover, the intensity scintillation shows a significant decorrelation across the UHF comb of frequencies that occupies ~ 70 MHz.

Because of the broad interest in the experiment, both inside and outside the DNA community, detailed Bimonthly Progress Reports Numbers 1 through 6 have been made available to essentially all interested parties. Thus in this report we shall not reproduce in detail the material contained in those bimonthly progress reports (here after BPR). We will, however, describe in some detail those aspects of the project not previously reported.

The experiment has been quite successful. The first year's effort, however, necessarily included the development of a substantial amount of routine data reduction software and hardware. The data reduction procedures are reviewed in Section II, together with experimental findings that have shaped the form our routine data reduction operations have taken.

The experiment operations for the first year are summarized in Section III. Well over 700 passes have been detrended and summarized for detailed analysis. Thus we have acquired a varied and unique collection of high-latitude and equatorial ionospheric amplitude and phase scintillation data from which both the detailed structure of the scintillation and the conditions under which it occurs can be studied.

9

In Section IV we present a detailed summary of recent analyses of the auroral zone scintillation data that have not appear in the BPRs. We present evidence of a geometrical scintillation enhancement due to east-west sheet-like irregularity structures. Direct pattern anisotropy measurements made by using the spaced receivers further support the sheet hypothesis. We also present preliminary results of a study of the poleward boundary of the high-latitude trough as inferred from TEC data.

In Section V we summarize the characteristics of the equatorial scintillations that have been observed at both Ancon and Kwajalein, particularly the gigahertz scintillation that develops during very active periods. We also present some preliminary results from the equatorial scintillation campaign conducted in Peru during March 1977. A considerable amount of work remains to verify and fully develop the ramifications of these preliminary results. The important subject of the detailed relationships between the structure of the amplitude and phase scintillation and the irregularity structure has not been addressed in this report, although the subject is currently under active study by a number of researchers who are currently using or intend to use Wideband satellite data.

10

II OVERVIEW OF FIRST YEAR'S DATA ANALYSIS

The Wideband satellite operations conducted over the past 12 months
have provided a large and varied data base of measured radiowave pertur-
bations induced by propagation through regions of structured (striated)
ionospheric plasma. The satellite (P76-5), which is in a high-inclination,
sun-synchronous orbit, continuously transmits ten (VHF to S-band) phase-
coherent CW signals. At the receiving stations (now Poker Flat, Alaska;
Ancon, Peru; and Kwajalein Atoll in the Marshall Islands), the S-band
signal is used as a phase reference to synchronously detect all the
lower frequencies.

Synchronous detection automatically removes the geometrical Doppler
due to physical path changes. Thus, as long as the S-band signal is
not severely disturbed, the detected complex signal structure reflects
the combined effects of gross propagation-path changes (dispersive phase)
and small-scale ionospheric irregularities (amplitude and phase scintil-
lation). To analyze the scintillation data it is necessary to first
remove the slow trends.

The "detrending" procedure that was developed for this purpose is
described in BPRs 1 and 2. A digital recursive filter with a sharp
cutoff at 0.1 Hz is used to separately detrend the phase and amplitude
data that are first decimated to 100 Hz. Thus, amplitude and phase
variation. with periods greater than 10 s are processed as trends and
the faster variations as scintillations. It has been found that with
few exceptions (see Section V-A) the intensity data show no significant
refractive variations with periods greater than 10 s. This was the
primary reason for selecting the 0.1-Hz cutoff. For the phase data
there is no clear demarcation between trends and random perturbations.

The slow phase trends are processed to extract the ionospheric
total electron content. The procedure is described in detail in BPR 5.

11

The TEC data provide a considerable amount of information about the structure of the background ionosphere in which the irregularities develop.

The main objectives of the experiment, however, are to determine the detailed structure of signal perturbations and the physical processes that give rise to their occurrence, particularly very intense amplitude scintillation. It is well known that amplitude scintillation (fading) can seriously degrade the performance of satellite communication links. More recently, however, it has become clear that naturally occurring phase scintillation can impair the performance of satellite surveillance systems that use synthetic aperture processing to achieve high range resolution.

Indeed, one of the principal findings of the current Wideband satellite experiment, as well as the Navy Navigation Satellite and ATS-6 observations that preceeded it, is that naturally occurring phase scintillation is generally at least an order of magnitude larger than was expected on the basis of the conventional weak, single-scatter analysis of intensity scintillation data.

An example of the very large phase scintillation that can occur is shown in Figure 1, which is taken from BPR 2. The data are from a disturbed high-latitude pass. The VHF intensity scintillation is saturated ($S_4 = 1$) between 1220 and 1221 UT. The VHF phase scintillations exceed 2π radians over most of the pass. The UHF phase scintillations exceed 2π radians during the period of saturated VHF intensity scintillation. Moreover, the L-band scintillation exceeds 1 rad during the same period, even though there is no detectable L-band intensity scintillation.

In the absence of the phase data, one would likely invoke the weak single-scatter theory to explain the UHF data because of the small amplitude scintillation levels that are involved. Such an analysis would typically entail postulating an rms electron-density variation less than 10% of the average background electron density and an outer scale size comparable to the UHF Fresnel radius (≤ 1 km). This approach, however, invariably grossly underestimates the actual phase-scintillation level.

12
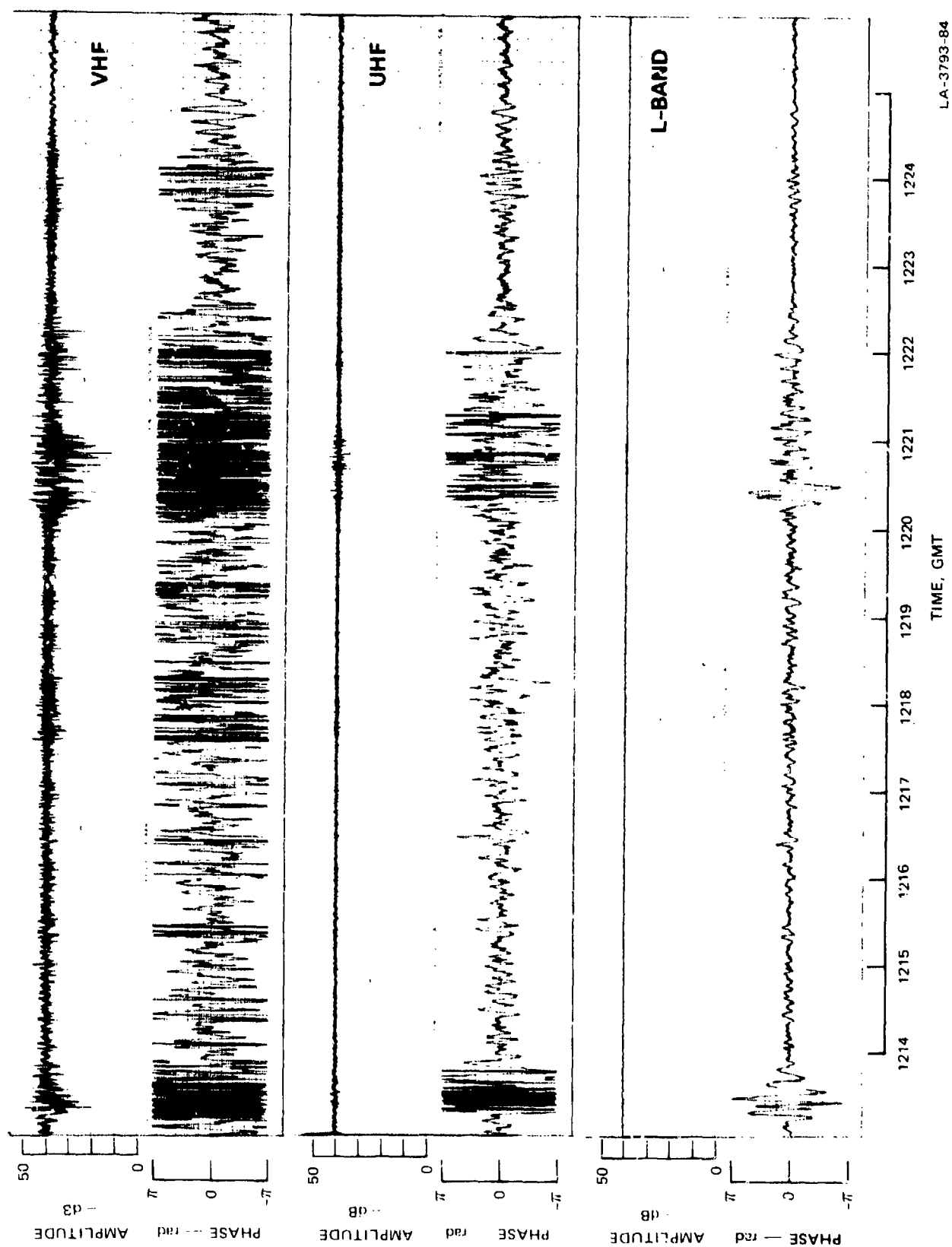
FIGURE 1   DETRENDED STRIP CHARTS FROM PASS 5-14 RECORDED AT POKER FLAT, 29 MAY 1976

LA-3793-84

TIME, GMT

13

To reconcile this discrepancy, a multiplicative two-component model has been developed. The single-scatter theory properly accounts only for the small but rapid scintillations that arise from diffractive scattering. The large but slowly varying phase scintillation and an associated weak amplitude variation occurs because of refractive focusing and defocusing. It is introduced into the model by postulating a second multiplicative component. This model is discussed briefly in BPR 3 and in more detail in Fremouw et al. (1976).[*]

The two-component model is very useful for characterizing the joint first-order statistics of amplitude and phase. However, a completely satisfactory theory must account for the structure of the scintillation without introducing imprecisely defined scale parameters. Indeed, in the power-law environment that characterizes ionospheric irregularities, there is a continuum of scale sizes with no well-defined outer-scale cutoff. Thus quantities, such as rms phase or rms electron density, cannot be uniquely determined. Our measured values of rms phase, for example, depend on the detrender cutoff.

To deal with this ambiguity, we have characterized the phase scintillation spectra in terms of a spectral strength parameter, T, and the usual power-law spectral index, p, so that $\varphi_\phi(f) = Tf^p$. Both parameters are obtained by performing a least-squares fit over the portion of the phase spectrum that is unaffected by noise at the high-frequency end and the detrending filter at the low-frequency end. Hence, the measured values of T and p are not influenced by the detrend period or, generally, the noise level.

The T and p parameters have been accumulated for all active passes taken during the 12-month period covered by this contract. A systematic study has just begun, but it is clear that p admits meaningful values from > -2 to < -4. At high latitudes p shows the most variability. Values between -2.5 and -3 are most commonly observed with steeper slopes ($p \lesssim -4$) generally persisting only for brief periods. At the equatorial

---

[*] References are listed at the end of this report.

14

stations there is evidence of a systematic flattening of the phase spectrum to values of p algebraically greater than -2 during very intense scintillation events (see Section V-A).

III   OVERVIEW OF FIRST YEAR'S OPERATIONS

The satellite and its payload have functioned nearly perfectly
throughout the entire year. Moreover, few receiver problems have
been encountered. The major problems have been with the antenna
systems, the various digital components, and the computer peripherals.
Specific problems have been documented in the bimonthly progress reports.
The most serious data loss occurred during November 1976 when the Ancon
antenna system failed.

To review the year's activity, we have plotted the number of passes
per month at each site in Figure 2. The large number of passes taken
during June reflects the fact that extra engineering and scientific
personnel were at Ancon and Poker Flat for the initial operations. The
increased activity during November at Poker Flat was in support of a
DNA rocket campaign. Preliminary results from the rocket campaign are
presented in BPR 4.

An "equatorial scintillation campaign" was conducted in Peru during
March 1977. M. D. Cousins assisted the Peruvian operators and provided
scientific support for the operation. A synopsis of the campaign is
contained in BPR 6. More recent results are discussed in Section V.

The number of detrends performed per month for each site is sum-
marized in Figure 3. The first version of the detrender program that
was used through the end of 1976 was not fast enough to allow routine
detrending and printer display operations to be efficiently carried out
at the field sites. Hence, the number of detrends consistently lagged
behind the total number of passes.

To alleviate this problem, writable control store memories were
added to the data acquisition systems at each of the sites and programmed
to perform the digital recursive-filtering operations. This greatly
speeded up the routine detrending operations so that the major portion

16
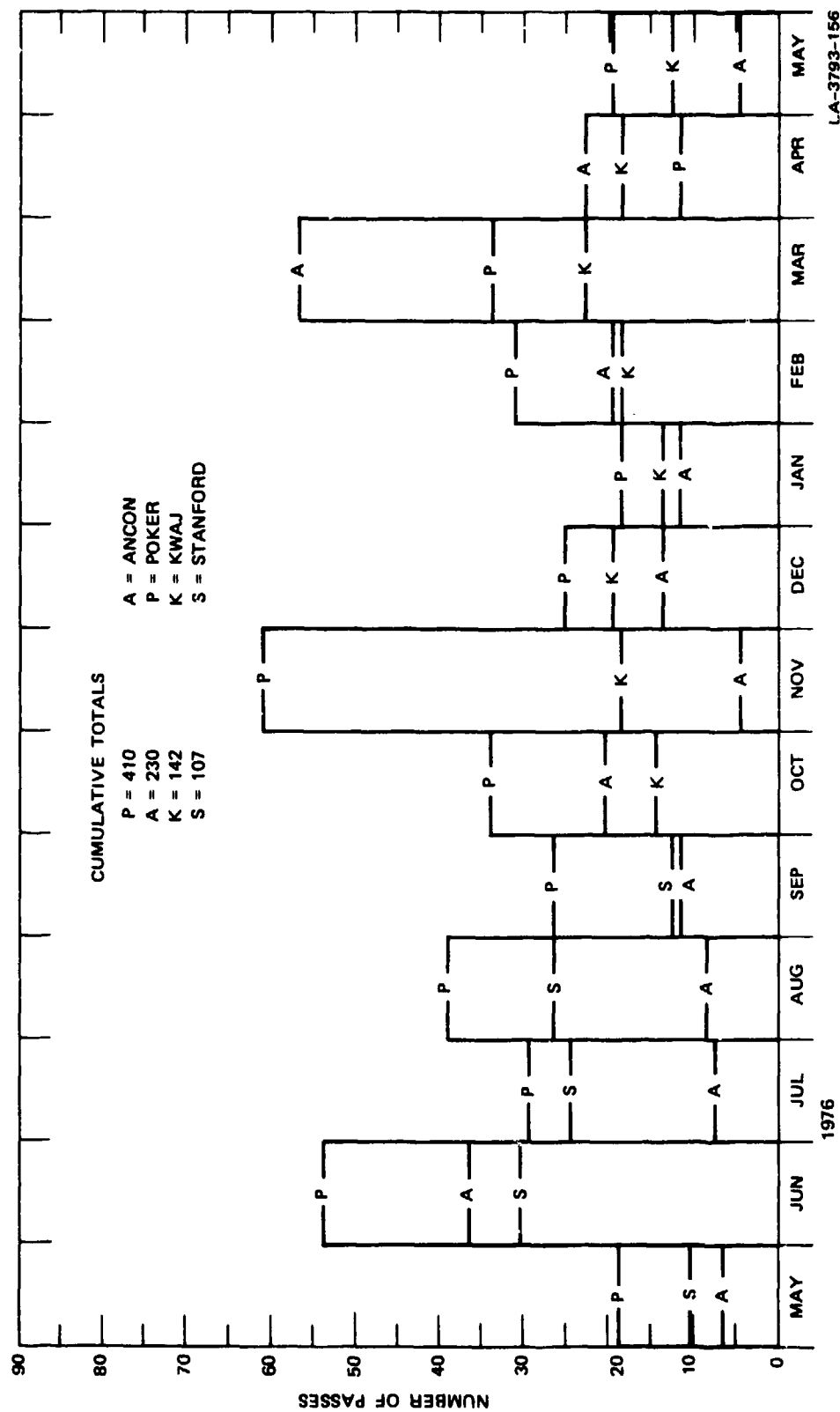
FIGURE 2   NUMBER OF PASSES BY MONTH PER SITE
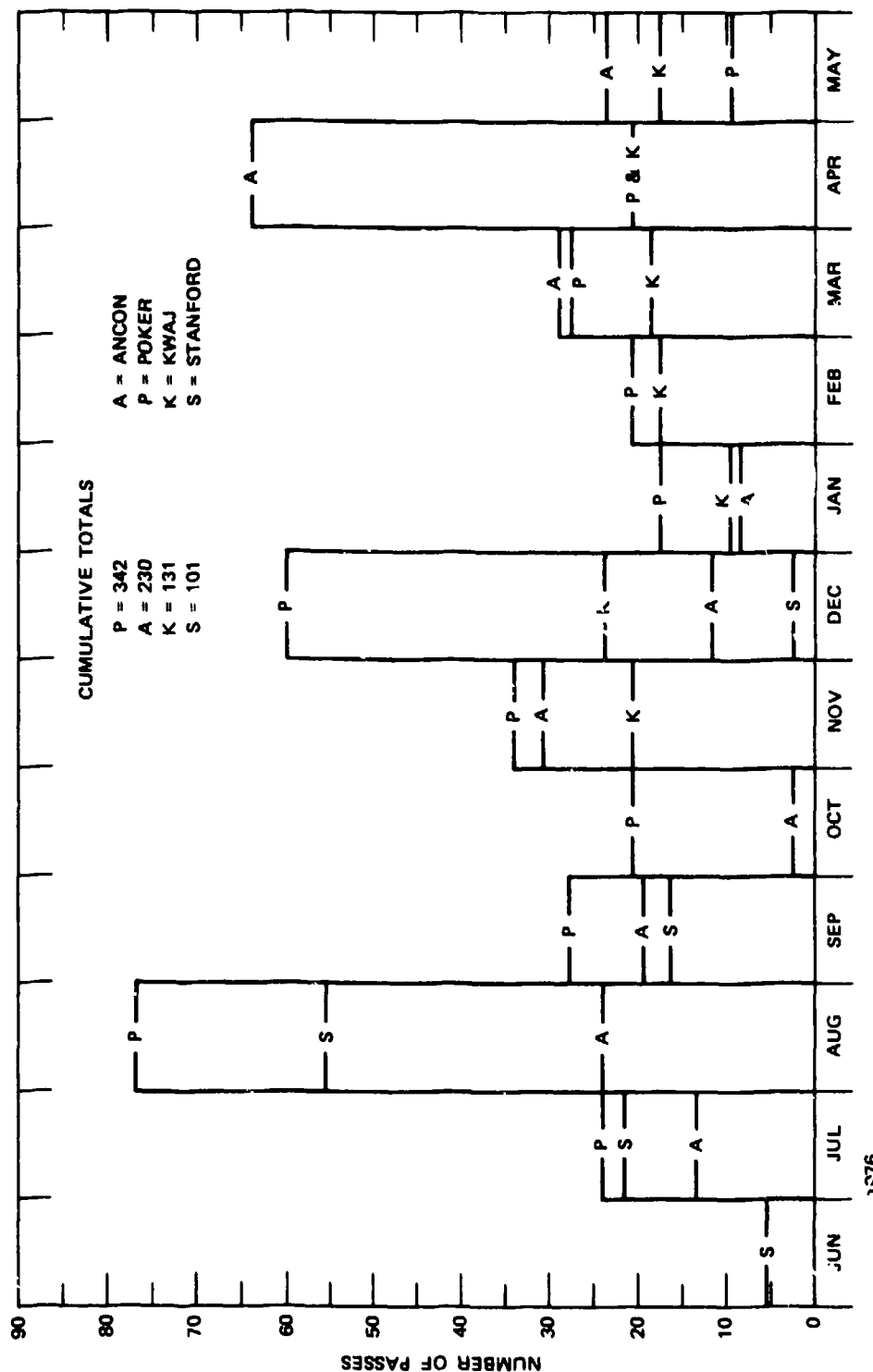
17

FIGURE 3   NUMBER OF DETRENDS BY MONTH PER SITE

LA-3793-157

18

of the data reduction (less the printer displays) could be performed between passes, that is inside of an hour's time.

The discrepancy between the total number of passes and the number of detrends is partly accounted for by engineering passes that were used for system checks. In the main, however, the discrepancy represents passes that were recorded with excessive parity errors. Many of these passes can be recovered although the procedure is costly. The nonrecoverable passes (~5%) typically develop through time periods when problems were being identified and diagnosed.

A scheme for categorizing the passes by activity level was developed (see BPR 3). Six activity levels from extremely quiet to very active have been used. The percentage of passes at each station in each category as of 23 May 1977 is shown in Figure 4. It is noteworthy that moderately active passes are most probable at Poker Flat, whereas very quiet passes are most probable at the equator stations. However, only the equator stations show both extremely quiet and extremely active passes.

The strong seasonal dependence at the equator stations accounts for the difference in the activity distribution between the auroral and equatorial stations. The equator stations appear to have a scintillation activity peak in the local summer. Thus, Ancon shows increasing activity through December whereas Kwajalein shows increasing activity beginning in late April.

Since data taking at Kwajalein began in October 1976, a quiet period, we have not observed as many very active passes as were observed at Ancon. Presumably this will equalize through this summer's operation when the activity at Kwajalein increases.

Nearly all of the detrended passes taken through May 1977 have been processed using the summary program described in BPR 4. The summary program generates the propagation angles at E- and F-region heights, a summary of the first-order signal moments, and parameters that characterize the VHF and UHF phase and intensity spectra. In addition, the amplitude and phase trends are preserved at a 1-Hz rate. These data

19
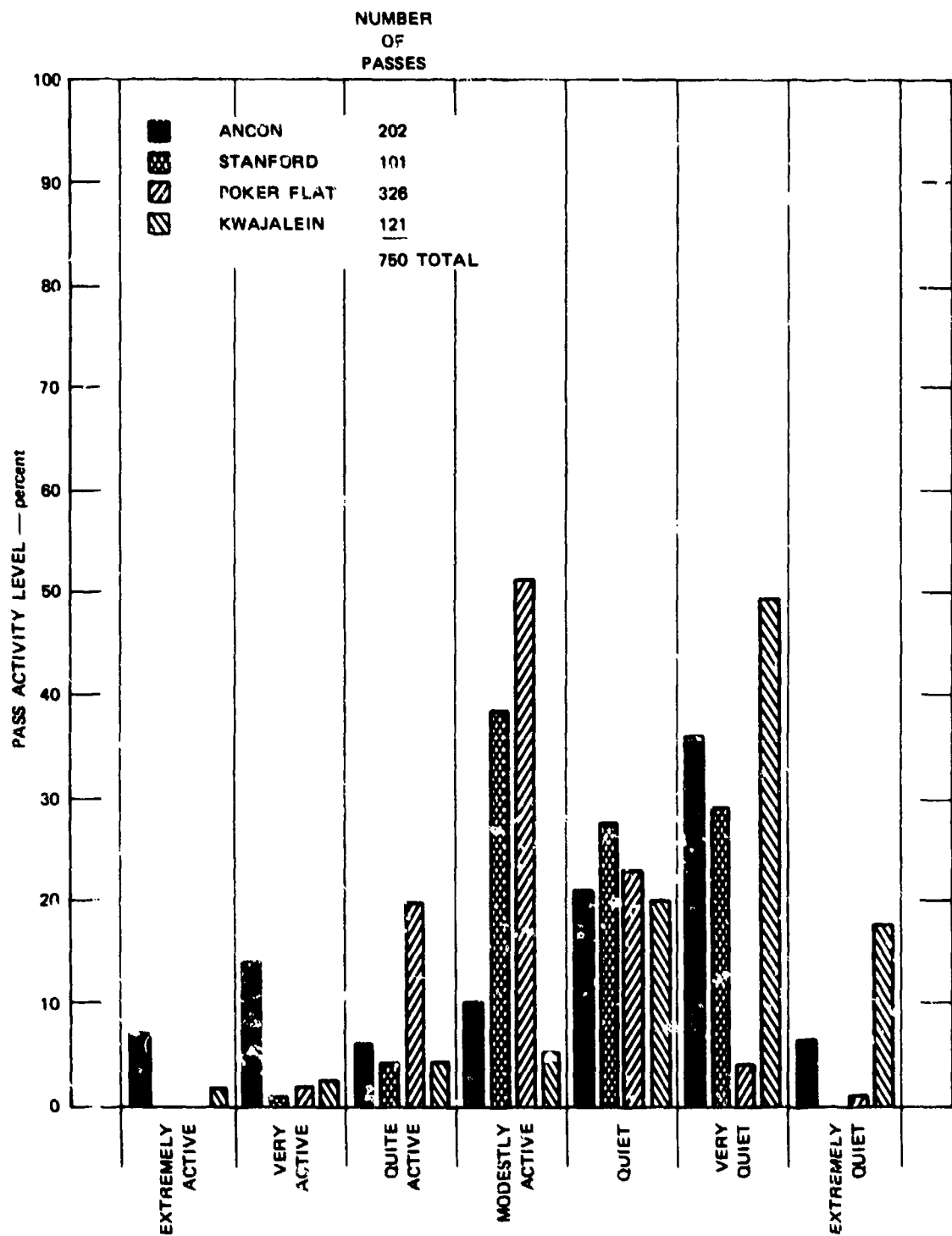
FIGURE 4   PASS ACTIVITY-LEVEL DISTRIBUTION FOR RECORDS INSPECTED AS OF 2? MAY 1977

20

are currently being used to study in more detail the morphology and structure of the scintillation data that have been accumulated through this past year.

IV AURORAL ZONE SCINTILLATION

A. Evidence for a Geometrical Enhancement

In BPR 6 a prominent auroral zone scintillation feature was described.
Indeed, it has been noted since the November rocket campaign that a narrow
burst of enhanced phase and amplitude scintillation occurs very near the
F-region line-of-sight intersection at $L = 5.5$. It was originally thought
that the enhancement was a genuine source variation because it occurred
over such a wide range of longitudes. More recently, however, we have
postulated a model in which the irregularities have a sheet-like anisot-
ropy that can explain this phenomenon as a purely geometrical enhancement.

Specifically, we have investigated a model in which the irregularities
have a high degree of coherence both along the magnetic field and trans-
verse to the magnetic field in the east-west direction. The theoretical
background for this study is developed in Rino and Fremouw (1977). Here
we shall only review the principal results, which also provide the basis
for the interferometer analysis presented in Part B of this section.
The analysis is considerably simplified if we treat only phase scintil-
lation in the linear-ray-optics approximation, i.e., we ignore diffraction
effects.

The justification for this simplification is the fact that the phase
scintillation, when corrected for the finite reference frequency, follows
a linear wavelength dependence under all but the most disturbed conditions.
An example is shown in Figure 5, which is a disturbed evening pass taken
at moderately low elevation angles. The data are plotted against Universal
Time with the angle between the propagation vector, the rms phase scin-
tillation, the magnetic field direction (the Briggs-Parkin angle) at
350 km, together with the dip angle, also given. The phase-scintillation
ratios in the middle frame are straight lines if the phase-scintillation
index, σ_ϕ, follows a linear wavelength dependence when corrected for the
finite reference frequency. We see that only the VHF phase scintillation

22
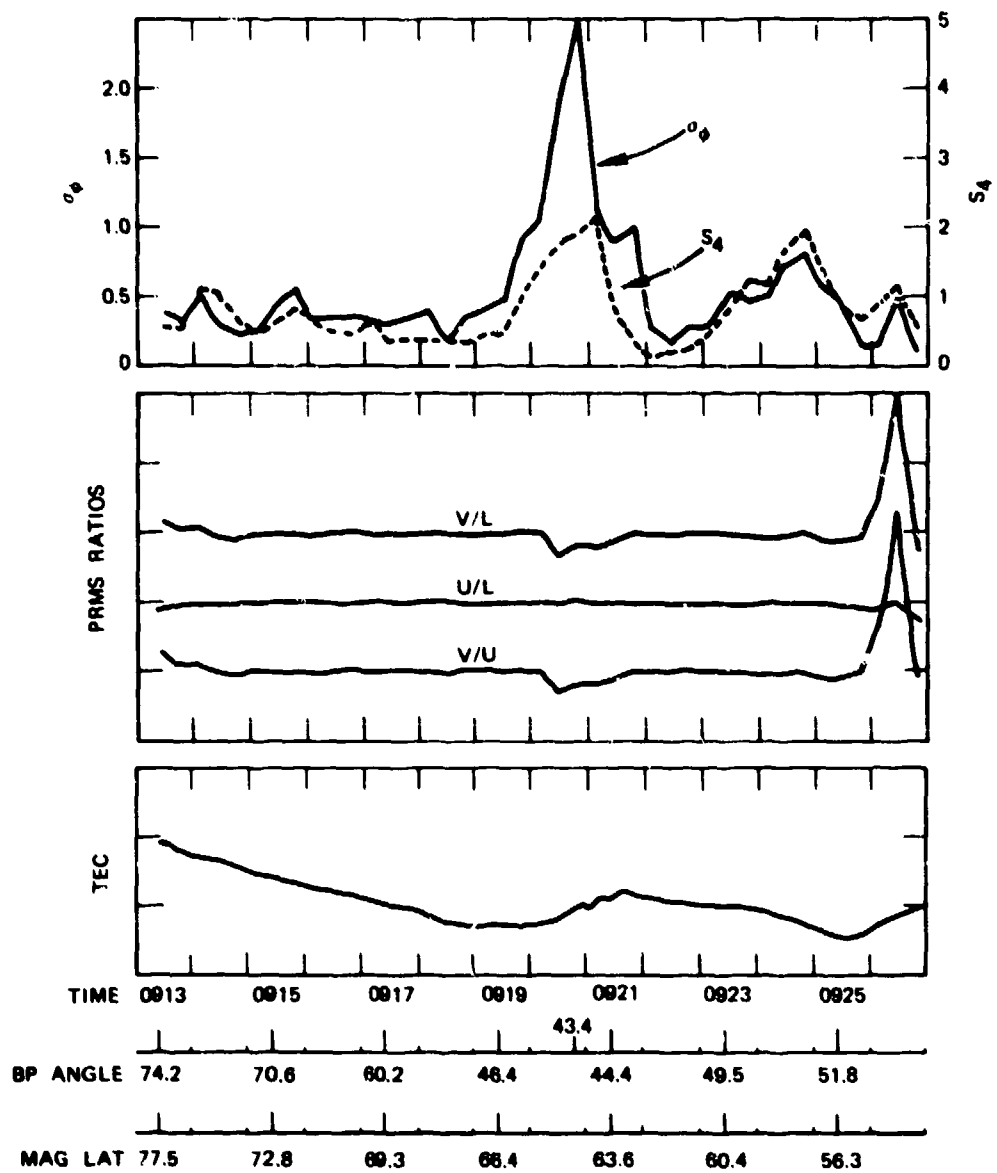
FIGURE 5   STANDARD SUMMARY DISPLAY FOR POKER FLAT PASS 6-36

23

shows any significant departure, and then only when S_4 is near unity.
(The variation at the end of the pass is due to ground multipath.)

To investigate the diffraction effects on phase scintillation in
more detail, we have compared a segment of the phase-scintillation data
for the highest UHF channel (UU3), the lowest UHF channel (UL3), and the
VHF channel. In Figure 6, we show the VHF phase scintillation. In
Figure 7(a) we show the phase difference between VHF and UU3 with the
latter scaled to the VHF using the corrected linear wavelength dependence.
The corresponding phase difference for UL3 and UU3 is shown in Figure 7(b).

The system phase noise is clearly evident in Figure 7. However, in
general the phase structure that can be attributed to diffraction effects
does not contain the low-frequency content that dominates the VHF phase
structure in Figure 6. To show this directly, in Figure 8 we have plotted
the VHF phase spectrum and the spectrum of the VHF-UU3 phase difference.
The spectra cross near 2 Hz, with the difference spectra showing a genuine
flattening to $\sim$2 dB below the VHF phase spectrum below 0.1 Hz. For the
high frequencies, the phase-difference spectrum is $\sim$3 dB higher than
the UHF phase spectrum, verifying that the high-frequency components are
uncorrelated.
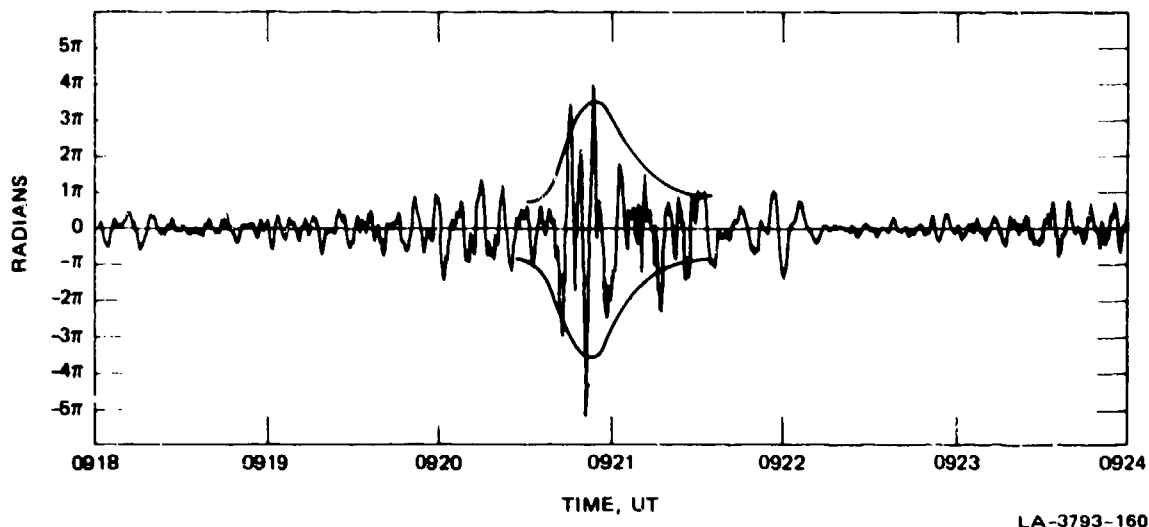
LA-3793-160

FIGURE 6   DETRENDED VHF PHASE FROM POKER FLAT PASS 6-36

24
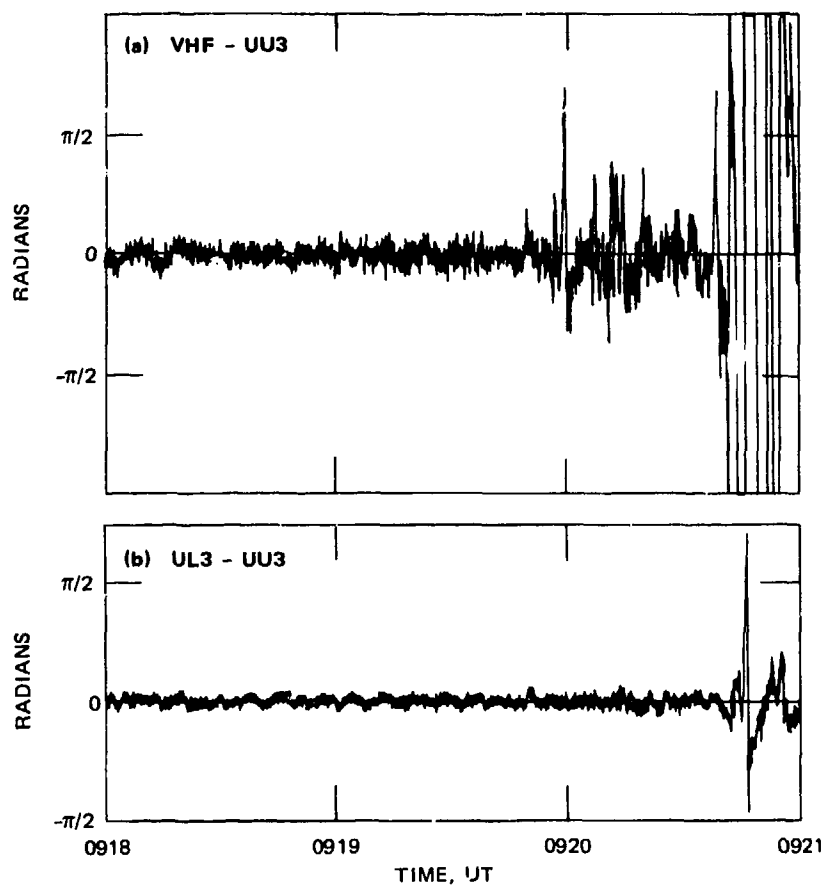
FIGURE 7   DIFFERENCE BETWEEN MEASURED PHASE AT LOW FREQUENCY
            AND SCALED PHASE FROM HIGHER FREQUENCY FOR SEGMENT
            OF POKER FLAT PASS 6-36:   (a) VHF-UU3, (b) UL3-UU3

25
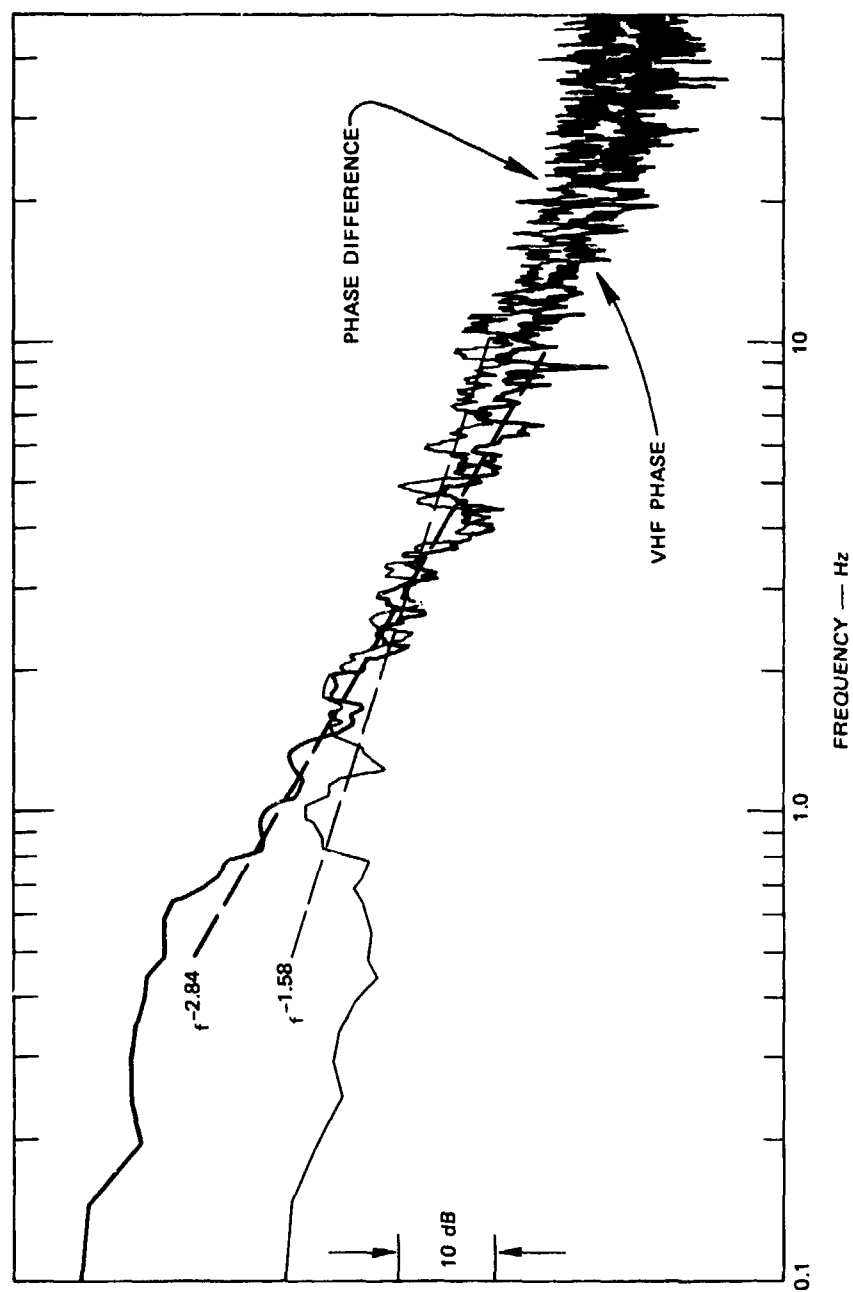
FIGURE 8   SPECTRAL DENSITY OF VHF PHASE AND PHASE DIFFERENCE FOR 20-s DATA RECORD FROM POKER
FLAT PASS 6-36 AT ~0919 UT

LA-3793-162

We conclude that, with the exception of the most disturbed cases, diffraction effects for phase are confined to the frequencies above 2 Hz. Since typically more than 90% of the contribution to σ_ϕ comes from the frequencies below 2 Hz, we are well justified in neglecting diffraction in our analysis of the geometrical dependence of phase scintillation.

In our analysis we have used the fixed coordinate system shown in Figure 9. Ignoring diffraction effects and any gross refractive effects, the signal phase is given by the straight-line ray-path integral

LA-3793-163
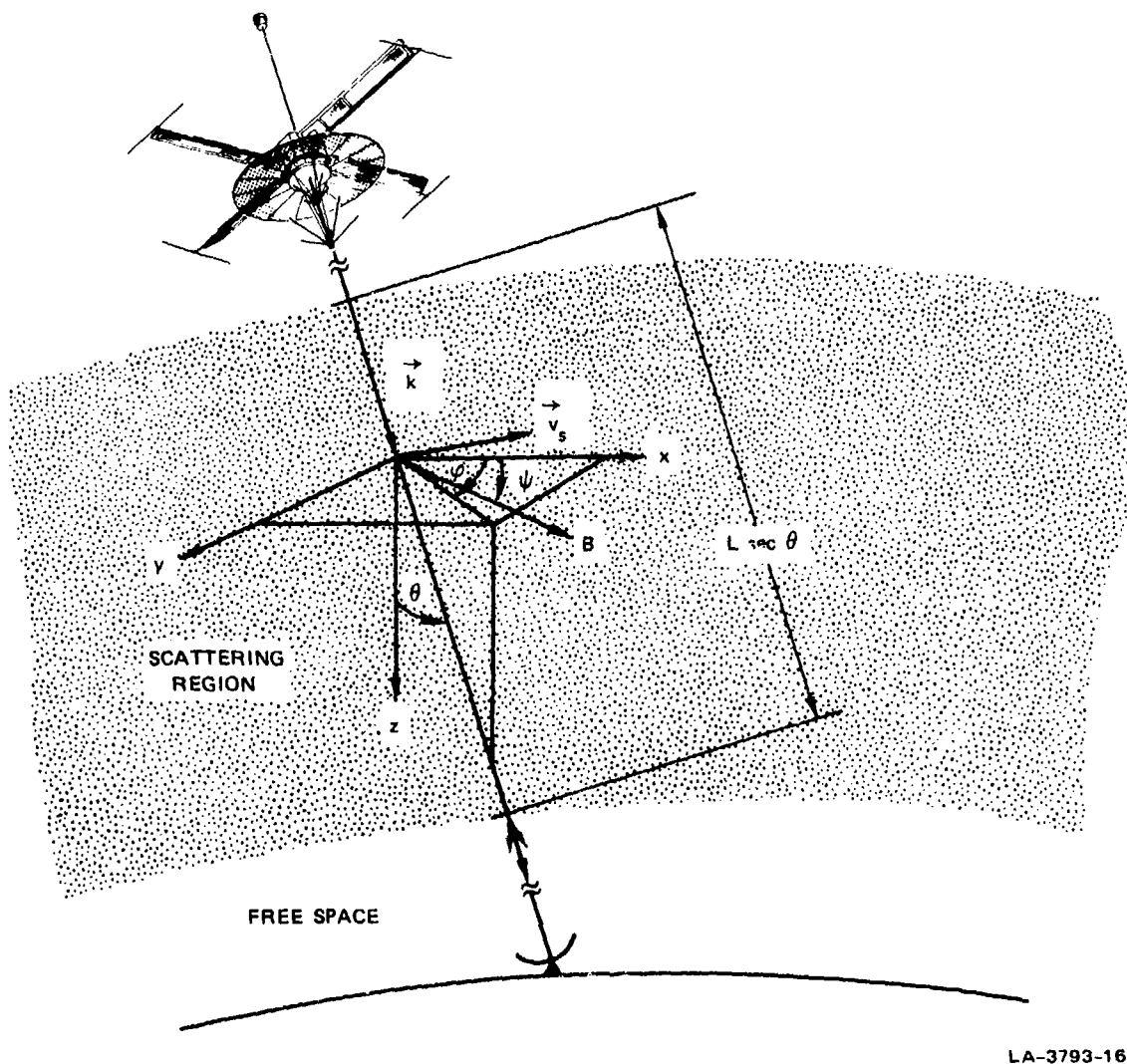
FIGURE 9   COORDINATE SYSTEM USED FOR THEORETICAL CALCULATIONS

27

$$\delta\phi(\vec{\rho}) = k \int_0^{\Delta L \sec\theta} \delta n(\vec{r})\,d\ell = -r_e \lambda \sec\theta \int_0^L \Delta N_e\left[\vec{\rho} + \tan\theta\,\hat{a}_{k_T}(\eta - z),\,\eta\right]d\eta \quad ,$$

(1)

where δn is the perturbation to the refractive index and $\hat{a}_{k_T}$ is a unit vector along the projection of $\vec{k}$ onto the xy plane. By direct computation from Eq. (1), we have

$$R_{\delta\phi}(\vec{\Delta\rho}) = r_e^2\lambda^2 \sec^2\theta\, L \int_{-L}^{L}\left(1 - \frac{|\eta|}{L}\right) R_{\Delta N_e}\left(\vec{\Delta\rho}_s + \tan\theta\,\hat{a}_{k_T}\,\eta,\,\eta\right)d\eta \quad ,$$

(2)

where $\vec{\Delta\rho}_s = \vec{\Delta\rho} - \tan\theta\,\hat{a}_{k_T}\,\Delta z$. The dependence on Δz accounts for the fact that the phase structure is generally not sampled in a plane parallel to the xy plane.

Equation (2) exhibits a complicated dependence on the layer thickness. However, if the correlation distance along z, ℓ_z, is small compared to L, then for $\eta > \ell_z \ll L$, $R_{\Delta N_e} \cong 0$. In that case

$$R_{\delta\phi}(\vec{\Delta\rho}) \cong r_e^2\lambda^2 \sec^2\theta\, L \int_{-\infty}^{\infty} R_{\Delta N_e}\left(\vec{\Delta\rho}_s + \tan\theta\,\hat{a}_{k_T}\,\eta,\,\eta\right)d\eta \quad .$$

(3)

The spatial Fourier spectrum of $R_{\delta\phi}$ is readily computed as

$$\Phi_{\delta\phi}(\vec{\kappa}) = r_e^2\lambda^2 \sec^2\theta\, L\Phi_{\Delta N_e}\left(\vec{\kappa},\,-\tan\theta\,\hat{a}_{k_T}\cdot\vec{\kappa}\right) \quad ,$$

(4)

where $\Phi_{\Delta N_e}(\vec{\kappa}, \kappa z)$ is the three-dimensional spectral density function of $\Delta N_e(\vec{\rho}, z)$.

The phase-scintillation index is given by the value of Eq. (3) at $\vec{\Delta\rho} = 0$ or the integral of Eq. (4) over all $\vec{\kappa}$. Thus,

28

$$\sigma_\phi = r_e^2 \lambda^2 \sec^2 \theta L \int_{-\infty}^{\infty} R_{\Delta N_e} \left(\tan \theta \; \hat{a}_{\hat{k}_T} \; \eta, \eta \right) d\eta \qquad (5a)$$

$$= r_e^2 \lambda^2 \sec^2 \theta \; L \iint_{-\infty}^{\infty} \Phi_{\Delta N_e} \left(\vec{\kappa}, \; -\tan \theta \; \hat{a}_{k_T} \cdot \vec{\kappa} \right) \frac{d\vec{\kappa}}{(2\pi)^2} \qquad (5b)$$

It is clear from the form of Eq. (5a) and (5b) that σ_ϕ can exhibit a complicated dependence on the propagation angles. For isotropic irregularities, however, $R_{\Delta N_e}$ depends only on $(\Delta \rho^2 + \Delta z^2)^{1/2}$, with a similar result for $\Phi_{\Delta N_e}$. In that case, it follows from Eq. (5a) or (5b) by a simple change of variables that $\sigma_\phi \propto \sec \theta L$.

It is instructive to compare these results with the case in which $\ell_z \gg L$. Then, Eq. (2) gives

$$R_{\delta\phi}(\vec{\Delta\rho}) \cong r_e^2 \lambda^2 (L \; \sec \; \theta)^2 R_{\Delta N_e} (\vec{\Delta\rho}_s, 0) \quad . \qquad (6)$$

Thus, for very large irregularities the geometrical dependence of σ_ϕ is simply $(L \sec \theta)^2$ independent of any anisotropy exhibited by $\Delta N_e (\vec{\rho}, z)$. However, such large structures are best treated as trends, and we shall not consider them further here.

To continue, we need to model the anisotropy of $\Delta N_e (\vec{\rho}, z)$. In Rino and Fremouw (1977) we used the extension of the Briggs-Parkin and Budden model developed by Singleton. In that model the irregularity structures are assumed to have extended spatial coherence along two mutually perpendicular axes. The principal axis is taken along the magnetic field. The second axis can be inclined at an arbitrary angle relative to the meridian plane.

When this model is used, Eq. (4) takes the form

$$\Phi_{\Delta N_e} \left(\vec{\kappa}, \; -\tan \theta \; \hat{a}_{k_T} \cdot \vec{\kappa} \right) = ab\langle \Delta N_e^2 \rangle \; Q \left(\left[A\kappa_x^2 + B\kappa_x \kappa_y + C\kappa_y^2 \right]^{1/2} \right) \quad ,$$

$$\qquad (7)$$

29

where a and b are the respective axial ratios along and transverse to the magnetic field and Q[q] is the mathematical form of the three-dimensional spectrum. The anisotropy coefficients A, B, and C, which are defined in Rino and Fremouw, 1977, are functions of a, b, θ, φ, the magnetic dip angle, ψ, and the orientation angle, δ, for the second elongation axis.

To study the geometrical dependence of the phase scintillation as well as the anisotropy of the diffraction pattern, it is unnecessary to specify $Q(q)$. Indeed, Eq. (2) can be shown to have the general form

$$R_{\delta\phi}(\vec{\Delta\rho}) = \sigma_\phi^2 \mathcal{R}[f(\vec{\Delta\rho}_s)] \quad , \tag{8}$$

where

$$f(\vec{\Delta\rho}_s) = \left[\frac{C\Delta\rho_{x_s}^2 - B\Delta\rho_{x_s}\Delta\rho_{y_s} + A\Delta\rho_{y_s}^2}{(AC - B^2/4)}\right]^{1/2} \tag{9}$$

$$\sigma_\phi^2 = r_e^2 \lambda^2 \langle \Delta N_e^2 \rangle \mathcal{L}(L \sec \theta) \varkappa \tag{10}$$

$$\mathcal{L} = \frac{ab}{\sqrt{AC - B^2/4} \cos \theta} \tag{11}$$

$$\varkappa = \frac{1}{2\pi} \int_0^\infty q\, Q(q)\, dq \quad , \tag{12}$$

and $\mathcal{R}(y)$ is the three-dimensional Fourier transform of $Q(q)$.

In this model, contours of constant phase correlation are ellipses with the axial ratio given as

$$AR = \frac{A + C + D}{A + C - D} \quad , \tag{13}$$

30

where

$$D = \sqrt{(A - C)^2 + B^2/4} \quad . \qquad (14)$$

The orientation angle, ϕ_R, is given as

$$\phi_R = \frac{1}{2} \, \text{atan} \left[\frac{B}{C - A} \right] \quad . \qquad (15)$$

To complete the model we need only introduce the scan velocity $\vec{v}$, which is the apparent velocity of the irregularities at the penetration point due to both the source motion and the true irregularity drift. Thus, the measured correlation function is obtained by substituting $\vec{\Delta\rho} - \vec{v}\Delta t$ for $\vec{\Delta\rho}$ in Eq. (8).

The temporal correlation function measured at a single receiver is obtained by setting $\vec{\Delta\rho} = 0$. Thus, by making the appropriate substitutions, we have

$$R_{\delta\phi}(\Delta t) = \sigma_\phi^2 \mathcal{R}(v_{eff}\Delta t) \quad , \qquad (16)$$

where

$$v_{eff} = \left[\left(C v_{x_s}^2 - B v_{x_s} v_{y_s} + A v_{y_s}^2 \right) / (AC - B^2/4) \right]^{1/2} \quad , \qquad (17)$$

with $\vec{v}_s = \vec{v}_T - \tan \theta \, \hat{a}_{k_T} v_z$. The velocity parameter v_{eff} accounts for the fact that the time structure of the scintillation depends critically on the anisotropy of ΔN_e. As an example, for the same scan velocity the time structure of the phase is slower when scanned along the principal axis of the diffraction pattern than when scanned across it. In this model we neglect any temporal change in the irregularities as the pattern is scanned.

Returning now to the geometrical dependence of σ_ϕ, we consider Eq. (10). We see that the angle dependence of σ_ϕ^2 is contained entirely in the product G sec θ. For isotropic irregularities, G = 1 as we have already noted. For field-aligned irregularities, G achieves its maximum value, a, for propagation along the principal irregularity axis and

31

reduces to unity for propagation angles well removed from the principal irregularity axis.

We show this effect in Figure 10 where $G \sec \theta$ is plotted against θ for different magnetic azimuth angles φ. We used a $= 50$ with $\psi = 76°$, the latter being the nominal dip angle for the Poker Flat receiving station. When $\varphi = 0$, there is a 50:1 enhancement at $\theta = 14°$, which is the field-aligned direction. The enhancement rapidly broadens and diminishes as $|\varphi|$ increases. The shape of $G \sec \theta$ ceases to change for axial ratios greater than ~ 20. Thus, if the abscissa in Figure 10 is scaled to unity at 50, then the curves are universal for a $\geqslant 20$.

Now, if the irregularities are elongated along the second axis ($b > 1$), say in the geomagnetic east-west direction ($\delta = 0$), $G \sec \theta$ achieves its maximum value ($G_{max} = a$) whenever the line of sight crosses the "sheet" axis. When $\delta = 0$, the sheets are aligned along the local
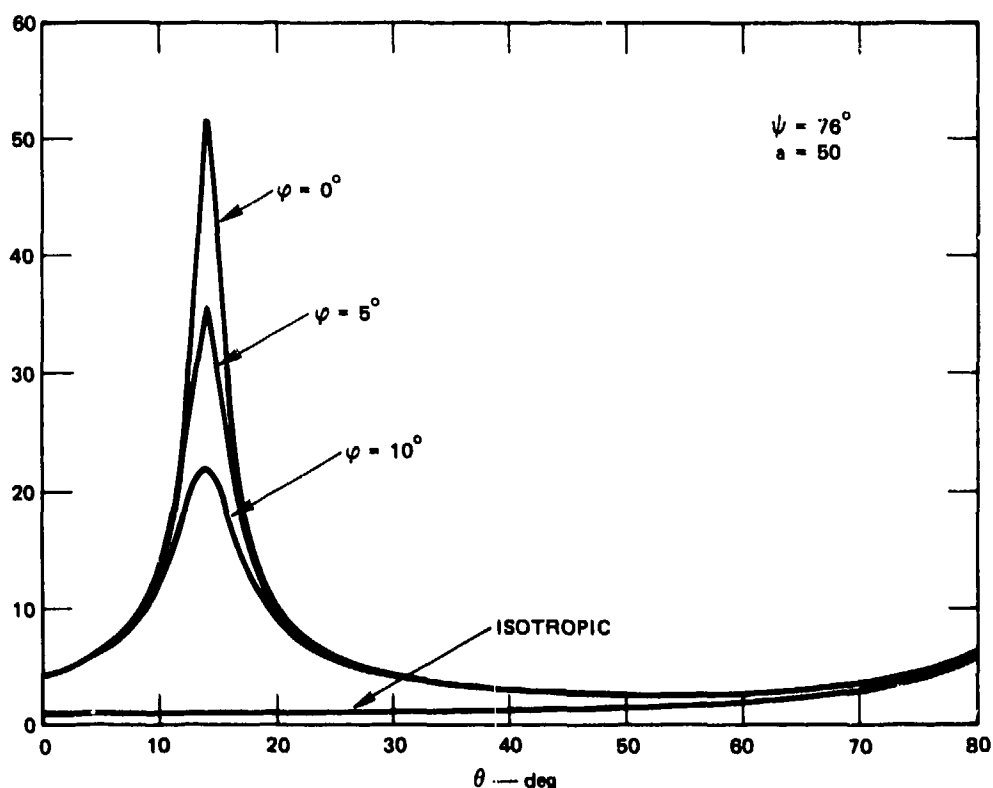
LA-3793-164

FIGURE 10 GEOMETRICAL DEPENDENCE OF PHASE SCINTILLATION FOR ROD MODEL

32

L-shell. The geometrical enhancement for such sheet-like structures is shown in Figure 11.
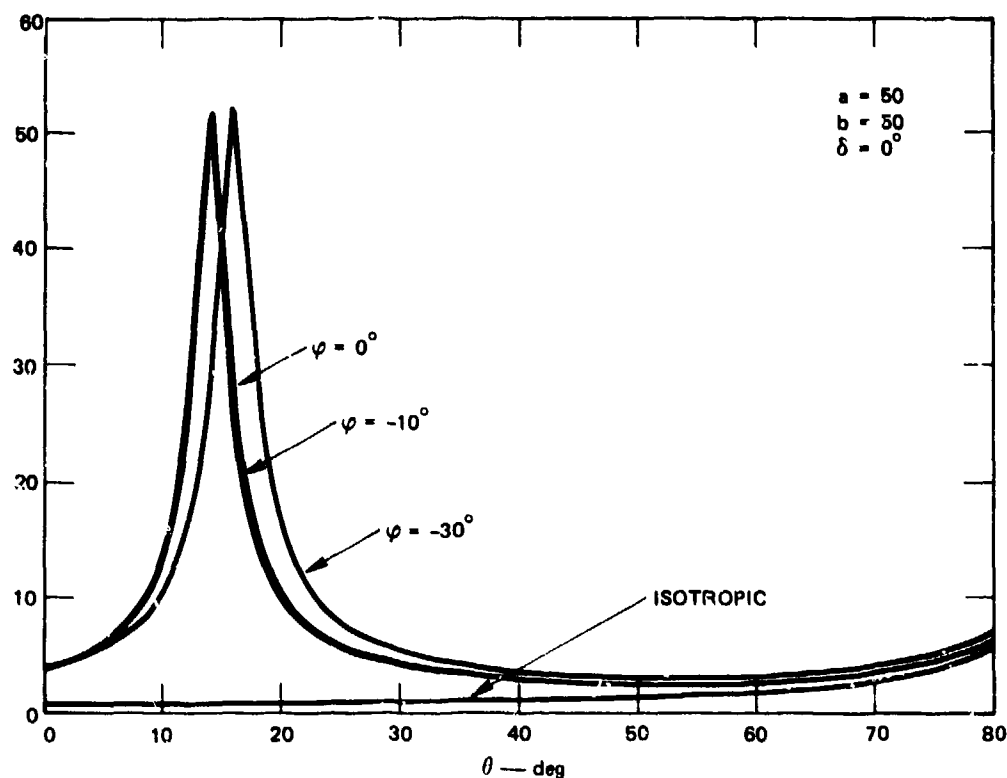
FIGURE 11   GEOMETRICAL DEPENDENCE OF PHASE SCINTILLATION FOR SHEET MODEL

It is clear from the outset, however, that from the observed phase scintillation variations alone we cannot separate a genuine source variation from a geometrical enhancement. On the other hand, if detectable enhancements consistently occur where the theory predicts, we can develop some confidence that we are seeing a geometrical effect. The spaced-receiver analysis described in Section B does not suffer from this ambiguity, but, owing to sensitivity and time-consuming processing, it is not feasible to fully process all the passes that show this effect.

To look for geometrical effects, we first isolated all the passes that came within 10° of the field-aligned propagation direction. These passes necessarily occur near local midnight and many are disturbed so that complicated source variations often mask any geometrical enhancement

33

that might be present. At the opposite extreme, a fair number of the midnight passes are quiet, with the field-aligned propagation point falling within the high-latitude plasma trough.

For these weak scintillation events, we have found that there is a well-defined enhancement whenever the line-of-sight comes within a few degrees of the field-aligned propagation direction. An example for which a clear enhancement is evident is shown in Figure 12. The phase-scintillation index is normalized to its local maxima and replotted in the lower frame. The dashed curve is the value of G sec θ separately normalized in the same way.
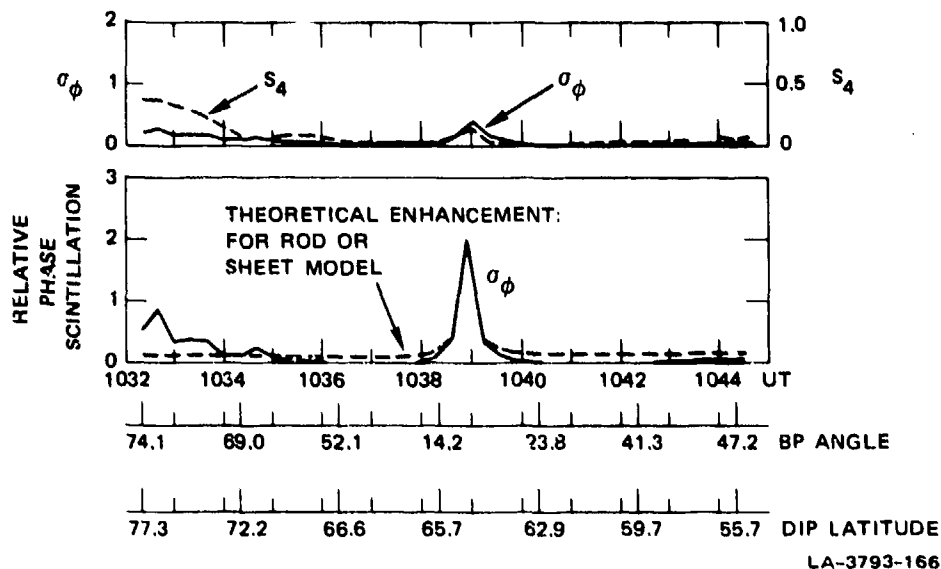
FIGURE 12   GEOMETRICAL ENHANCEMENT FOR POKER FLAT PASS 9-49 TOGETHER WITH CALCULATION OF THEORETICAL ENHANCEMENT

The fit is very good except near the "edges" of the enhancement where the theoretical curve does not fall off rapidly enough. We believe this effect can be explained and shall return to it shortly. For cases of weak scintillation in which the line of sight is not within a few degrees of the field-aligned direction, we find either no clear enhancement or a good fit to the rod model. Thus our tentative conclusion is that a weak background of irregularities exist in the plasma trough with a simple rod-like anisotropy.

34

For the more disturbed cases, which are generally poleward of the trough boundary and, therefore, in the region of the diffuse aurora, the rod model fails to characterize the enhancement. An example is shown in Figure 13. The rod model is clearly too broad for the 8.2° minimum Briggs-Parkin angle. The sheet model shown in the lower frame comes much closer, but it fails to drop off rapidly enough as we noted with Pass 9-49 shown in Figure 12.

To explain this effect, we note that the power spectrum of phase is the Fourier transform of Eq. (10), which has the general form

$$\varphi_\phi(f) \propto \frac{2\pi C_s}{v_{eff}\left[\kappa_o + (2\pi f/v_{eff})^2\right]^{\gamma+1/2}} \qquad (18)$$
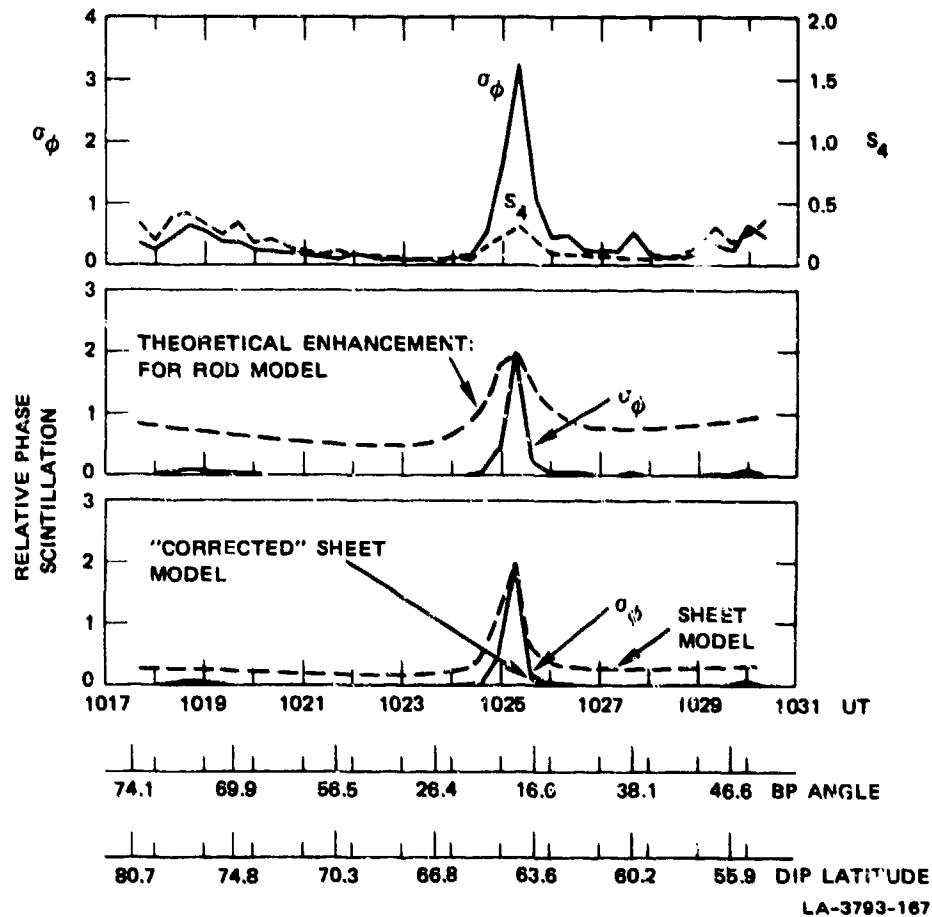
FIGURE 13   GEOMETRICAL ENHANCEMENT FOR POKER FLAT PASS 7-31 TOGETHER WITH CALCULATED THEORETICAL ENHANCEMENT AND CORRECTION FOR DETRENDER CUTOFF

35

However, since we have not observed the outer scale within the detrender cutoff f_c, we conclude that $2\pi f_c / v_{eff} \gg \kappa_o$. Thus the measured phase scintillation index, $\hat{\sigma}_\phi$, is given as

$$
\hat{\sigma}_\phi = r_e^2 \lambda^2 \ G \ \sec \ \theta L \kappa \ C_s \int_{-f_c}^{\infty} \left(\frac{2\pi_f}{v_{eff}}\right)^P d\left(\frac{2\pi_f}{v_{eff}}\right)
$$

$$
= r_e^2 \lambda^2 L \kappa C_s \left[G \ \sec \ \theta \ v_{eff}^{-(p+1)} \right] \ (2\pi f_c)^{-(p+1)} \quad , \tag{19}
$$

so that $\hat{\sigma}_\phi \propto G \ \sec \ \theta \ v_{eff}^{-(p+1)}$.

In the curve in Figure 13 marked "corrected" sheet model, we have used $G \ \sec \ \theta \ v_{eff}^{-(p+1)}$ with v_{eff} calculated from Eq. (17). The corrected curve fits the observed enhancement very well. In Figure 14, we have summarized the location of the enhancement for a number of typical midnight passes. In all the cases shown, the sheet model fits very well.

To show that the sheet model works for larger Briggs-Parkin angles, in Figures 15, 16, and 17 we show a sequence of enhancements for progressively increasing Briggs-Parkin angles. In Figure 16, the rod model predicts no local enhancement at all. Figure 17, in which only the sheet model is plotted, is interesting because there is evidence of a localized enhancement within an aurorally disturbed region. A summary of the enhancement location for a selected set of morning and evening passes is shown in Figure 18. The scatter around the L = 5.5 contour is evidently due to the 20-s sample interval.

All nighttime passes taken through December 1976 have been analyzed for geometrical enhancements. In ~60% of those passes, there is a localized phase- and amplitude-scintillation enhancement that can be completely explained by the east-west ($\delta = 0$) sheet model. Since the shape of the geometrical enhancements saturates, we can only put a lower bound on the axial ratios at ~10:10:1 or greater. Now, of the remaining

36
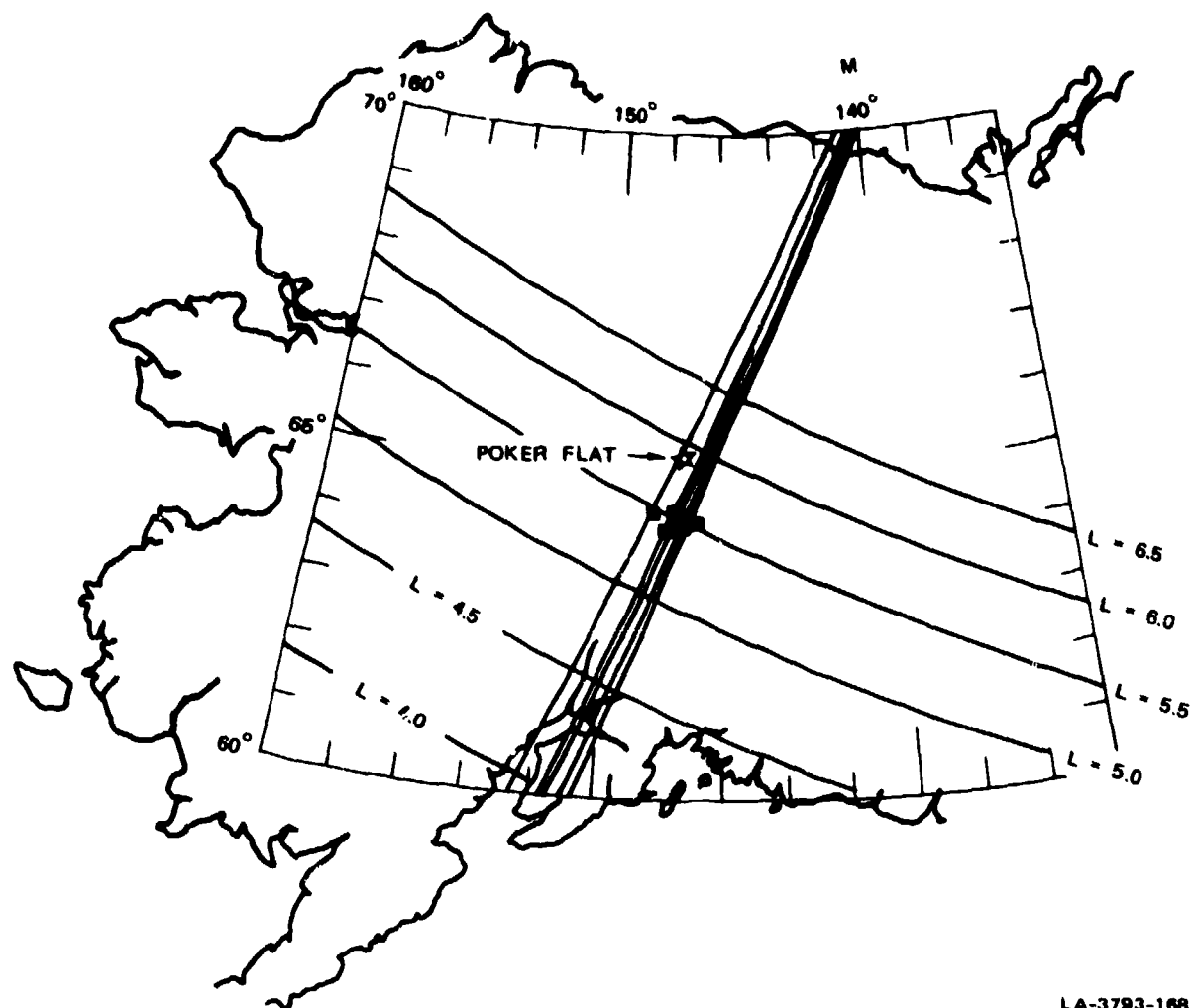
LA-3793-168

FIGURE 14   LOCATION OF GEOMETRICAL ENHANCEMENT FOR SELECTED SET OF
MIDNIGHT HIGH-ELEVATION PASSES
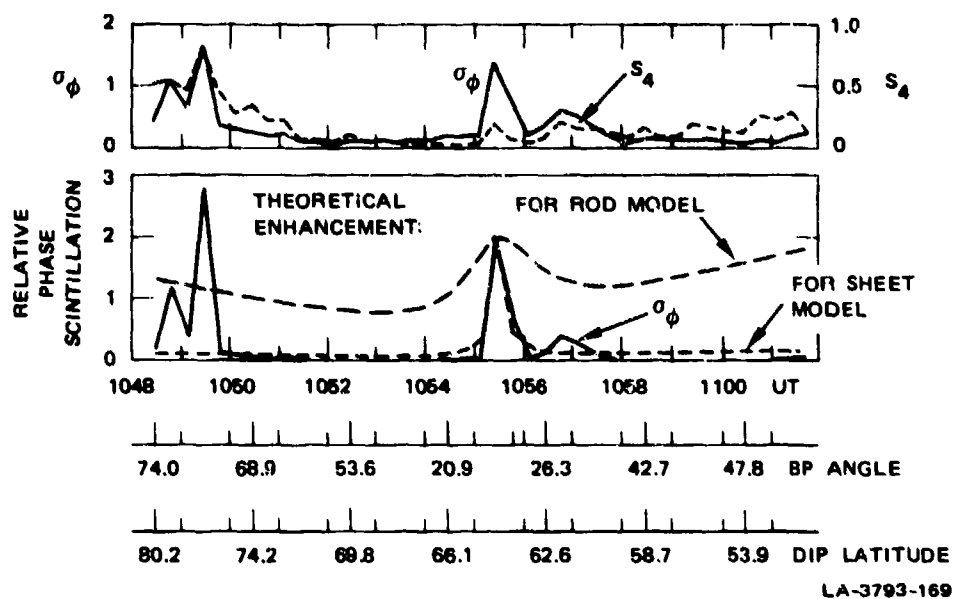
FIGURE 15   GEOMETRICAL ENHANCEMENT FOR POKER FLAT PASS 5-42 TOGETHER
WITH CALCULATED THEORETICAL ENHANCEMENT
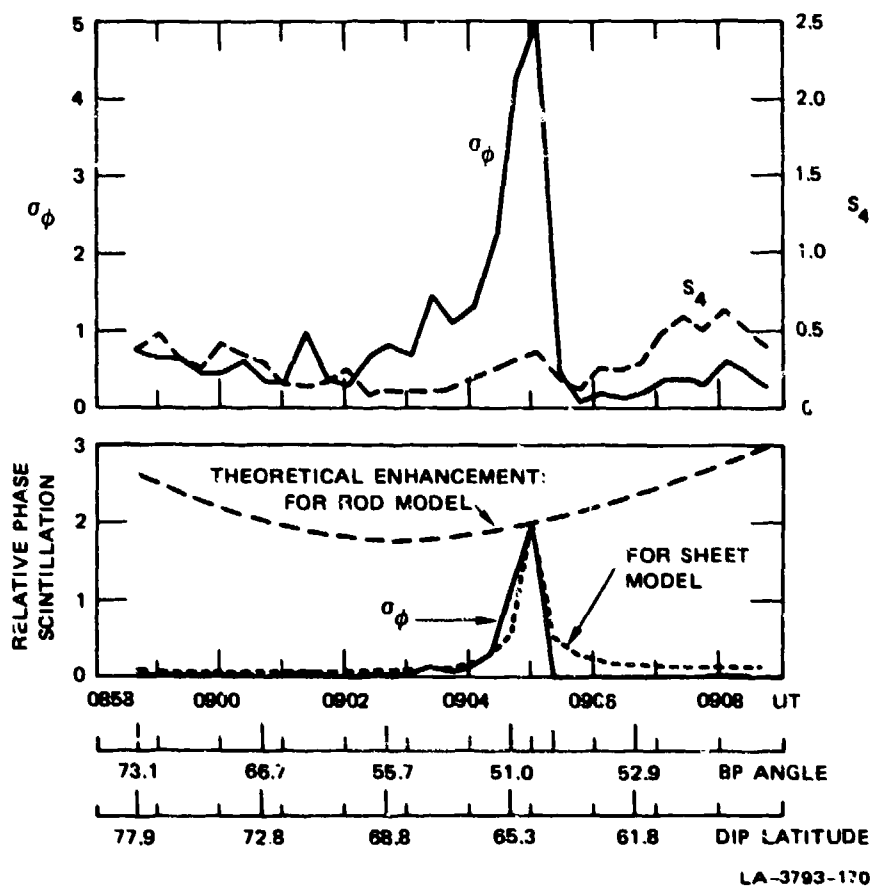
FIGURE 16   GEOMETRICAL ENHANCEMENT FOR POKER FLAT PASS 9-36 TOGETHER
WITH CALCULATED THEORETICAL ENHANCEMENT

38
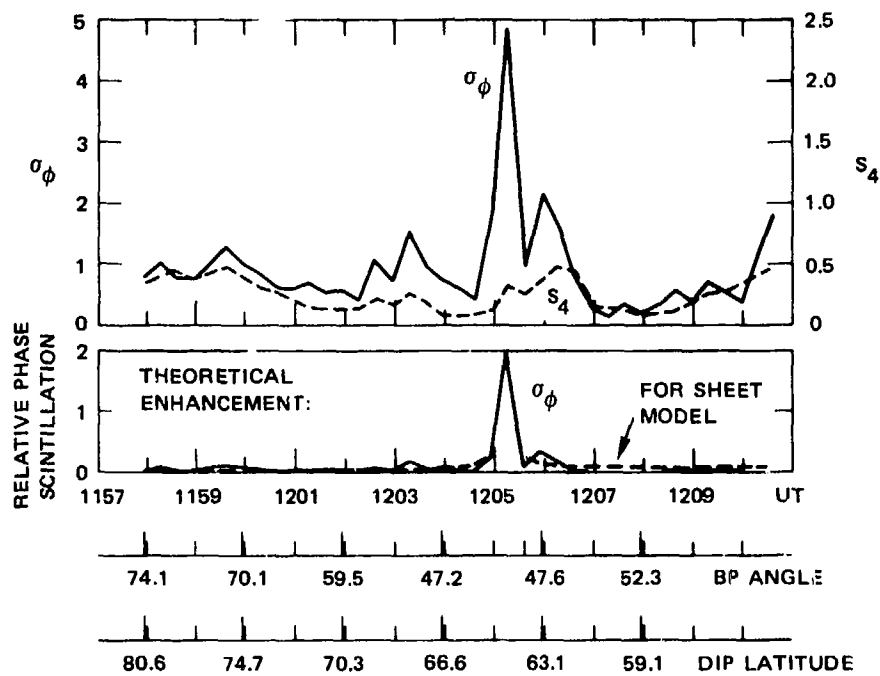
FIGURE 17   GEOMETRICAL ENHANCEMENT FOR POKER FLAT PASS 5-54 TOGETHER
WITH CALCULATED THEORETICAL ENHANCEMENT
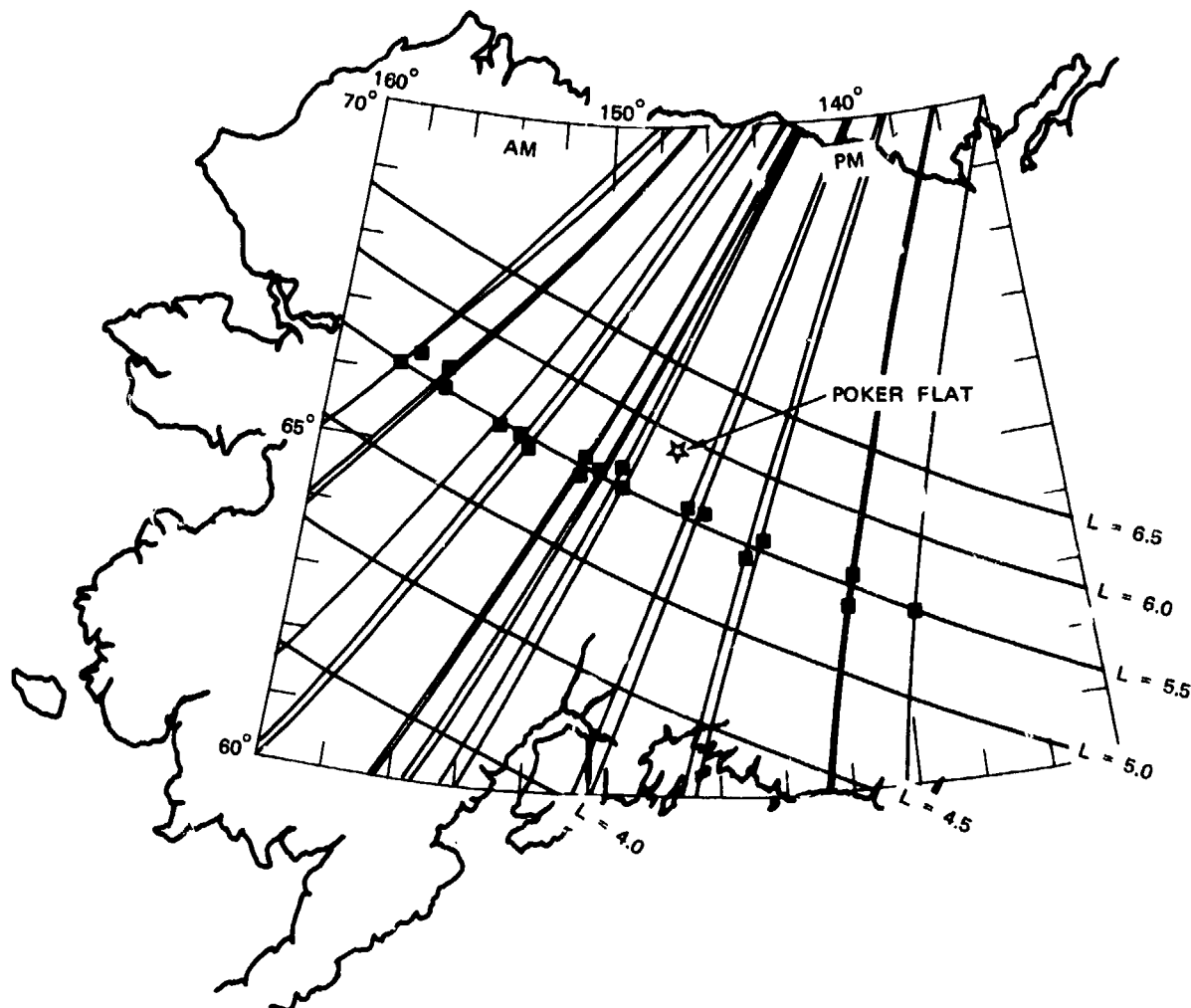
LA-3793-172

FIGURE 18   LOCATION OF GEOMETRICAL ENHANCEMENT FOR SELECTED EVENING
            AND MORNING PASSES

40% of the passes, half were either very quiet or very disturbed, so
that the geometrical enhancement is not prominent. We have already
noted that the weak irregularities in the trough appear to be rod-like.

The final 20% of the passes show a localized enhancement that is
generally displaced from the predicted point of occurrence of the geo-
metrical enhancement. As noted in BPR 6, a true source enhancement is
possible for these cases. On the other hand, there is no obvious dif-
ference in the structure of the phase or amplitude scintillation when
compared to other passes where the model fits. However, in each of the

40

cases where this discrepancy occurs, the enhancement is at or very near the TEC boundary that indicates the poleward wall of the plasma trough. Such events are described in BPR 6.

By comparing near simultaneous elevation scans taken with the Chatanika radar, it has been found that on many occasions a column of ionization extends through the F-region at the equatorward edge of the diffuse aurora. An example is shown in Figure 19 where the TEC and VHF scintillation are shown for Pass 12-15 together with contours of constant electron density obtained from the Chatanika radar. For this particular pass, the predicted enhancement for the sheet model occurs on the poleward edge of the observed scintillation enhancement.

Indeed, a TEC enhancement is coincident with the scintillation enhancement. The TEC enhancement is readily explained by the column ionization in the Chatanika radar data, and it is tempting to associate the scintillation enhancement with a true source enhancement within the column. However, an extended column of ionization can cause significant refractive effects at VHF, particularly at grazing incidence angles. Since only straight-line ray paths are considered in our analysis to date, it is possible that our calculation of the location of the geometrical enhancement is incorrect.

To summarize, we have found good agreement with the sheet model in ~60% of high latitude nighttime data, that is for all cases that were observed poleward of the diffuse aurora. Only ~20% of the passes showed isolated scintillation enhancements that were not explained by the model. However, we have noted that refractive bending of the propagation path may be important in these cases. In Subsection B, we present an analysis of interferometer data that unambiguously verifies the sheet model for at least a limited number of passes.

B.   Spaced-Receiver Measurements of Ionospheric Irregularity
      Anisotropy and Motion

The multiple-spaced receiver system used in conjunction with the main receiver at the Poker Flat Station allows us to measure the anisotropy of the diffraction as well as the apparent pattern motion. These

41

FIGURE 19   COMPARISON OF WIDEBAND SCINTILLATION AND TEC DATA FOR POKER
FLAT PASS 12-15 AND CHATANIKA RADAR MERIDIONAL ELECTRON
DENSITY MEASUREMENTS

42

measurements can, in turn, be used to infer the true anisotropy and drift motion of the ionospheric irregularities. We describe the method and present our preliminary results in this subsection.

As the satellite passes overhead, the propagation path scans through the irregular medium, and at our receivers we observe the projected time-changing diffraction pattern as shown schematically in Figure 20. In an ideal case, with multiple receivers we should be able to determine the correlation surface in this projected pattern. Then, knowing the propagation geometry, the correlation function in the medium can be determined.
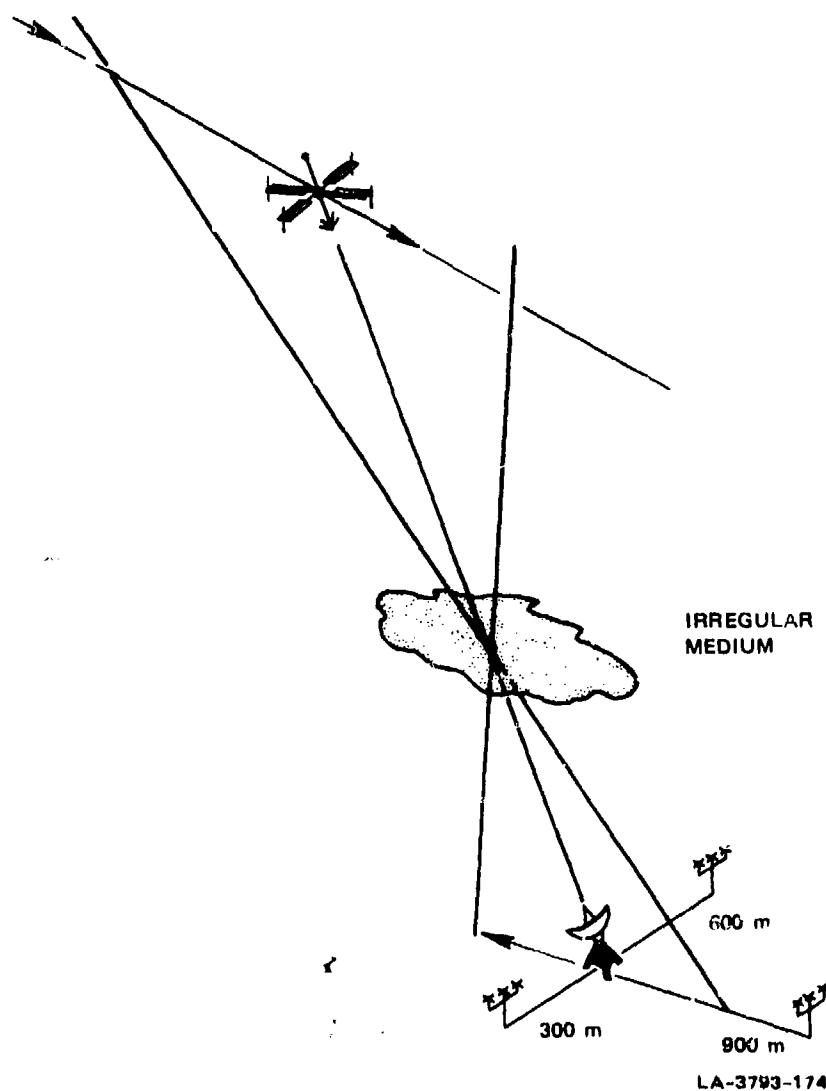

IRREGULAR
MEDIUM

600 m

300 m

900 m

LA-3793-174

FIGURE 20   POKER FLAT SPACED-RECEIVER GEOMETRY

43

Similarly, we should be able to measure the total drift of the irregularity pattern on the ground by using correlation methods. Since the contribution to the drift due to the satellite scan can be removed from this total, we can obtain an estimate of the irregularity velocity in the ionosphere.

When the spaced-receiver analysis effort began, we first developed methods to determine the pattern drift in the hope of determining irregularity drifts that could be compared with the plasma drifts measured by the Chatanika radar and other direct or indirect methods. The analysis method and some early results were reviewed in BPR 3. These early results showed some very striking features, in particular a large east-west shear that consistently appeared in conjunction with the scintillation enhancements discussed in Section IV-A. We have since found that the velocity features can be explained as signatures of sheet-like density structures in the medium. The apparent velocity is one of the parameters we are using to compare theory with measurement, and it is worthwhile to review the methods currently being used to derive this velocity in the analysis.

1. Apparent Velocity Method

A straightforward and intuitively satisfying application of the correlation method can be made to determine the pattern drift velocity if we assume that our multiple receivers are seeing the projection of a temporally unchanging irregularity structure, moving with a constant velocity, $\vec{V}$. If we compute the cross correlation of the signals at two receivers separated by a baseline $\vec{\Delta\rho}_j$, the resulting cross-correlation function maximizes at the time delay τ_j as shown in Figure 21. From measurements of τ_j obtained from signals taken on two orthogonal baselines, both the direction and magnitude of the pattern drift can be determined. A velocity derived in this way from the maxima of cross correlation functions is known as the apparent drift velocity in the terminology of Briggs et al., (1950), whose methods have provided the basis for most spaced-receiver correlation analyses.

In practice the irregularities are never strictly frozen. Moreover, the propagation geometry changes with time. This tends to make the true and apparent pattern velocities diverge. The method of

44
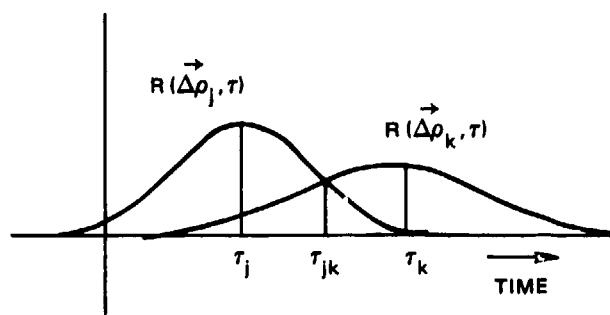
LA-3793-175

FIGURE 21   MEASUREMENT OF APPARENT VELOCITY
AND THE INTERSECTION OF TWO CROSS-
CORRELATION FUNCTIONS

Briggs et al., was extended by Phillips and Spencer (1955) to take into
account a temporarily changing pattern to yield the true pattern-drift
velocity from the measured cross-correlation functions. This is discussed
briefly in BPR 3. A further extension of one method mentioned by Briggs
et al., which is closely related to our method of estimating the pattern
anisotropy, is the method we propose to use to estimate the true irregu-
larity drift velocity. The method will be discussed in Subsection B-2.

        We can estimate apparent pattern velocity using the correlation
methods as outlined above. In fact, for Wideband, such methods can be
applied to both signal intensity and phase. The main shortcoming of the
correlation method is that it yields no information about the pattern
velocity as a function of spatial scale. Such information is important
if, for example, the irregularity motion is being driven by a dispersive
wave mechanism, such as ion acoustic waves. The dispersion information
could be extracted from the Fourier transform of the cross-correlation
function. Utilization of the cross spectrum in this manner has been
discussed in some detail by Gossard et al., (1967).

        The cross-correlation cross-spectrum transform pair can be
written as

$$R(\vec{\Delta\rho}_j - \vec{V}_s\tau) \leftrightarrows |\Phi_j(f)| \exp\{i\phi_j(f)\} \quad . \tag{20}$$

45

For the simplified case of a frozen pattern moving with constant velocity $\vec{V}_s$, it is clear that a shift in the correlation function due to $\vec{V}_s$ is recoverable from the phase of the cross spectrum. In particular

$$\vec{V}_s = \frac{2\pi f}{\phi_j(f)} \, \vec{\Delta\rho}_j \quad , \tag{21}$$

where $\phi_j(f)$ is the phase of a particular frequency component of the cross spectrum. Despite a 2π ambiguity in deriving the cross-spectrum phase, the spectral method requires no more effort than the time-domain method. Moreover, the spectral method gives a measure of the velocity dispersion.

During the course of the initial analysis, both the correlation and cross-spectral methods were applied to signal intensity and phase. Upon comparing the results, we found good agreement between the measured apparent velocities, particularly when the cross spectrum indicated non-dispersive motion. When the motion is dispersive, the apparent velocity derived from the cross spectrum agrees well with the velocity estimates obtained from the larger spatial scale portion of the cross spectrum.

An example of what we observed when the apparent velocity is calculated for a Wideband pass over Poker Flat is shown in Figure 22. This is a high-elevation pass (maximum elevation 79°) and what it shows is fairly typical of quiet geomagnetic conditions. The detrended VHF amplitude and phase [(a) and (b) of Figure 22] are quiet throughout the pass except for a burst of scintillation when the propagation path lies along the 1:. L-shell.

The apparent pattern velocities are shown in (c) and (d) of Figure 22. The orientation of the baselines at Poker Flat is such that the satellite scan is almost directly along the north-south baseline. Accordingly, � contribution to the observed signal-pattern drift from the satellite is primarily in a north-south direction, with a much smaller east-west component. In Figure 22(d), the observed northward velocity has the magnitude and behavior expected from a satellite scan through essentially stationary irregularities in the F-region. However, the
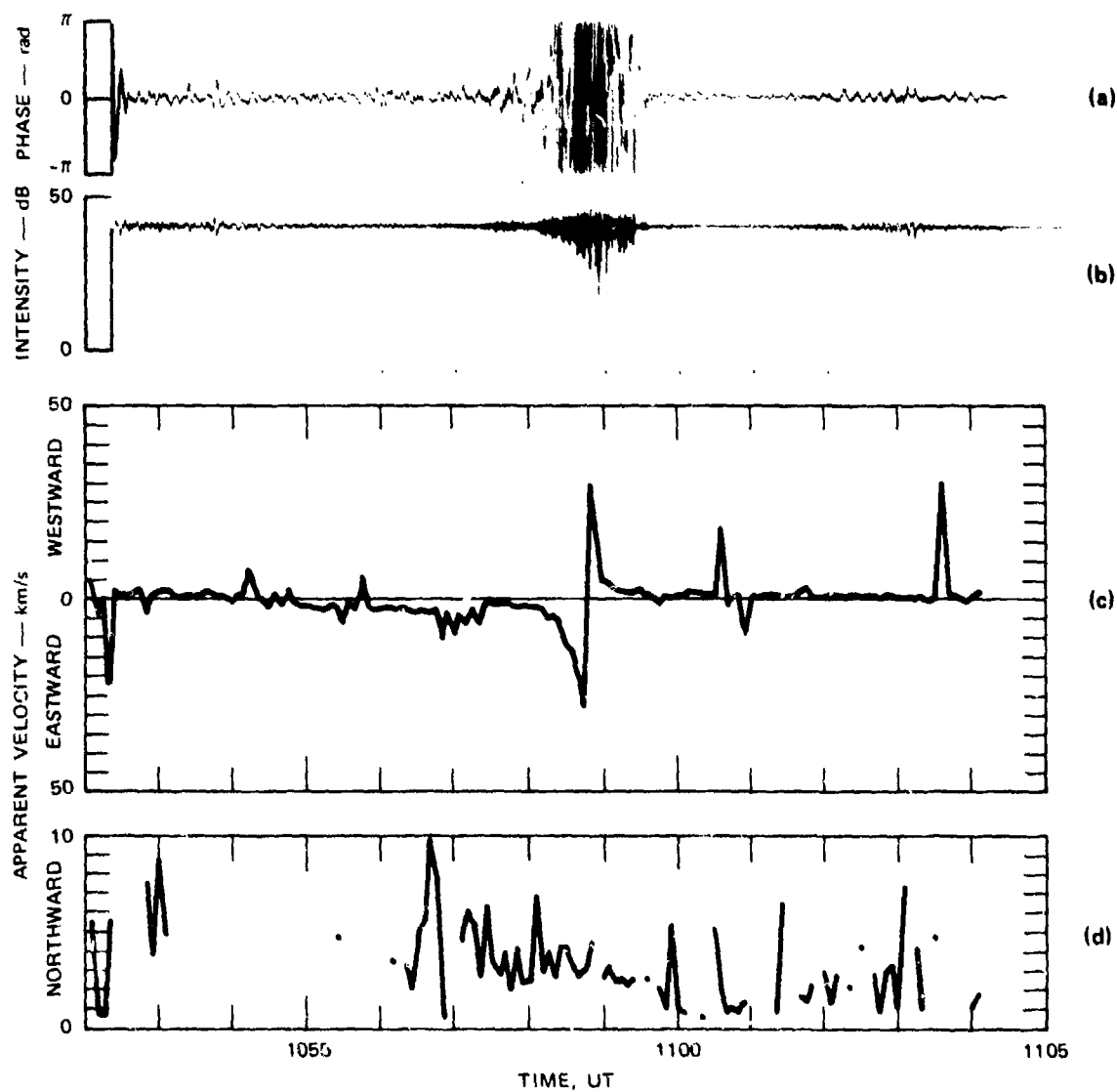
46

FIGURE 22   POKER FLAT PASS 15-34:   (a) VHF DETRENDED PHASE; (b) VHF DETRENDED
AMPLITUDE; (c) EAST-WEST MEASURED APPARENT PATTERN VELOCITY; AND
(d) MEASURED NORTH-SOUTH APPARENT PATTERN VELOCITY

LA-3793-176

47

east-west apparent pattern velocity in Figure 22(c) is dominated by a large velocity shear of magnitude ~30 km/s corresponding to the region of enhanced scintillation.

The east-west velocity shear, such as that shown in Figure 22, was initially attributed to irregularity motions. However, as more passes were analyzed and very large shears were observed in virtually every pass, it became clear that the observations had to be explained in another way, e.g., as being due to a rapidly changing anisotropy from the projection of highly elongated irregularities.

2. Anisotropy Method

There are a number of anisotropy estimation methods in the literature that use spaced receivers, but few are suitable for analyzing the Wideband data. In particular, our high data rates allow us to look at the data with high time resolution, and we often observe significant changes in the shape of the cross-correlation functions of intensity and phase in time. Therefore, we needed a method that minimized the restriction on correlation-function shape; such a method was used by Armstrong and Coles (1972) in their analysis of interplanetary scintillation.

The basic assumption of the method is that the lines of constant correlation in the irregularity diffraction pattern are concentric ellipses, or, more concisely, that they are of the general quadratic form:

$$R(\vec{\Delta\rho},\tau) = R[f(\vec{\Delta\rho}),\tau] \quad , \tag{22}$$

where $f(\vec{\Delta\rho}) = \vec{\Delta\rho}^T M \vec{\Delta\rho}$ and M is a 2×2 matrix whose elements define the orientation and anisotropy of the correlation ellipse [see Eq. (9)]. What we, as a stationary observer, really see is a correlation surface distorted by the satellite scan and any other irregularity motion. Thus, in place of Eq. (22), we have

$$R(\vec{\Delta\rho},\tau) = R[f(\vec{\Delta\rho} - \vec{V}_s\tau),\tau] \quad . \tag{23}$$

48

The basis for the method is that any two cross-correlation functions (indicated by the subscripts j and k) intersect when plotted on a common time axis (see Figure 21). At the point of intersection we must have

$$R[(\vec{\Delta\rho}_j - \vec{V}_s\tau_{jk}),\tau_{jk}] = R[(\vec{\Delta\rho}_k - \vec{V}_s\tau_{jk}),\tau_{jk}] \quad , \tag{24}$$

where τ_{jk} is the intersection time lag for the particular intersection. Equation (24) holds only if

$$(\vec{\Delta\rho}_j - \vec{V}_s\tau_{jk})^T M (\vec{\Delta\rho}_j - \vec{V}_s\tau_{jk}) = (\vec{\Delta\rho}_k - \vec{V}_s\tau_{jk})^T M (\vec{\Delta\rho}_k - \vec{V}_s\tau_{jk}) \tag{25}$$

or

$$\vec{V}_s^T M (\vec{\Delta\rho}_j - \vec{\Delta\rho}_k) = \frac{1}{2\tau_{jk}} \left[\vec{\Delta\rho}_j^T M \vec{\Delta\rho}_j - \vec{\Delta\rho}_k^T M \vec{\Delta\rho}_k \right] \quad . \tag{26}$$

This is the Armstrong and Coles result, but unlike their analysis in which isotropic irregularities were assumed so that Eq. (26) can be solved for $\vec{V}_s$, we need both M and $\vec{V}_s$. To estimate M we introduce another set of readily measured time parameters, namely the times at which the intersecting correlation functions maximize, τ_j, shown in Figure 21. If the general quadratic form is differentiated, we find that τ_j must satisfy the relation

$$\vec{V}_s^T M \vec{\Delta\rho}_j = \tau_j \vec{V}_s^T M \vec{V}_s = \tau_j V_e^2 \quad . \tag{27}$$

This and a similar expression for the $\vec{\Delta\rho}_k$ baseline can be combined with Eq. (26) to obtain the system of equations

$$\vec{\Delta\rho}_j^T \left[M/V_e^2 \right] \vec{\Delta\rho}_j - \vec{\Delta\rho}_k^T \left[M/V_e^2 \right] \vec{\Delta\rho}_k = 2\tau_{jk}(\tau_j - \tau_k) \quad . \tag{28}$$

From Eq. (28) the anisotropy parameter matrix M can be determined by using the three measurable time parameters and the known baseline vectors. In practice this is done using the least-squares method for up to 240

49

intersection pairs (including autocorrelations), which are available with
our four antennas.

Thus we have a method that solves for pattern anisotropy inde-
pendent of the particular shape of the correlation function; only
elliptical symmetry is required. In addition, we note that in Eq. (28),
although we solve for M/V_e^2, reinsertion of this parameter into Eq. (26)
does not upset the equality, and we can go one more step and solve for
the true pattern velocity $\vec{V}_s$. This portion of the analysis has just
recently begun, but it already shows considerable promise in yielding
true irregularity velocities.

3. Evidence for Sheet-Like Irregularities

With methods available to derive both the apparent pattern
velocity and the anisotropy of the observed diffraction pattern, we
applied the theoretical model described in Section IV-A to compute
these same parameters as a function of postulated in situ anisotropies
and the known geometry. That is, in addition to describing the temporal
behavior of the signal as a function of propagation geometry, the method
was expanded to include spatial behavior. To reiterate, the theoretical
predictions are based upon the Singleton/Budden generalized irregularity
model for which, in addition to an elongation, a, along the local magnetic
field line, an elongation, b, perpendicular to the field line can be
postulated.

Figure 23 is an example of the predicted apparent pattern
velocity and anisotropy as would be observed at the receivers for a
typical high-elevation satellite pass at Poker Flat. The postulated
in situ irregularities shown are 10:1:1 rods, 10:10:1 sheets, and
10:5:1 sheet-like structures, all for an assumed 350-km penetration
altitude. There are several important features to note:

- At the horizon, the axial ratio [Figure 23(b)] for the
  rod model is large. Intuitively this can be seen as
  a "shadow lengthening" as the line of sight becomes
  nearly perpendicular to the rods. For the sheet model,
  the axial ratios at the horizon are small, while at the
  intersection of the local L-shell we see a large east-west

50
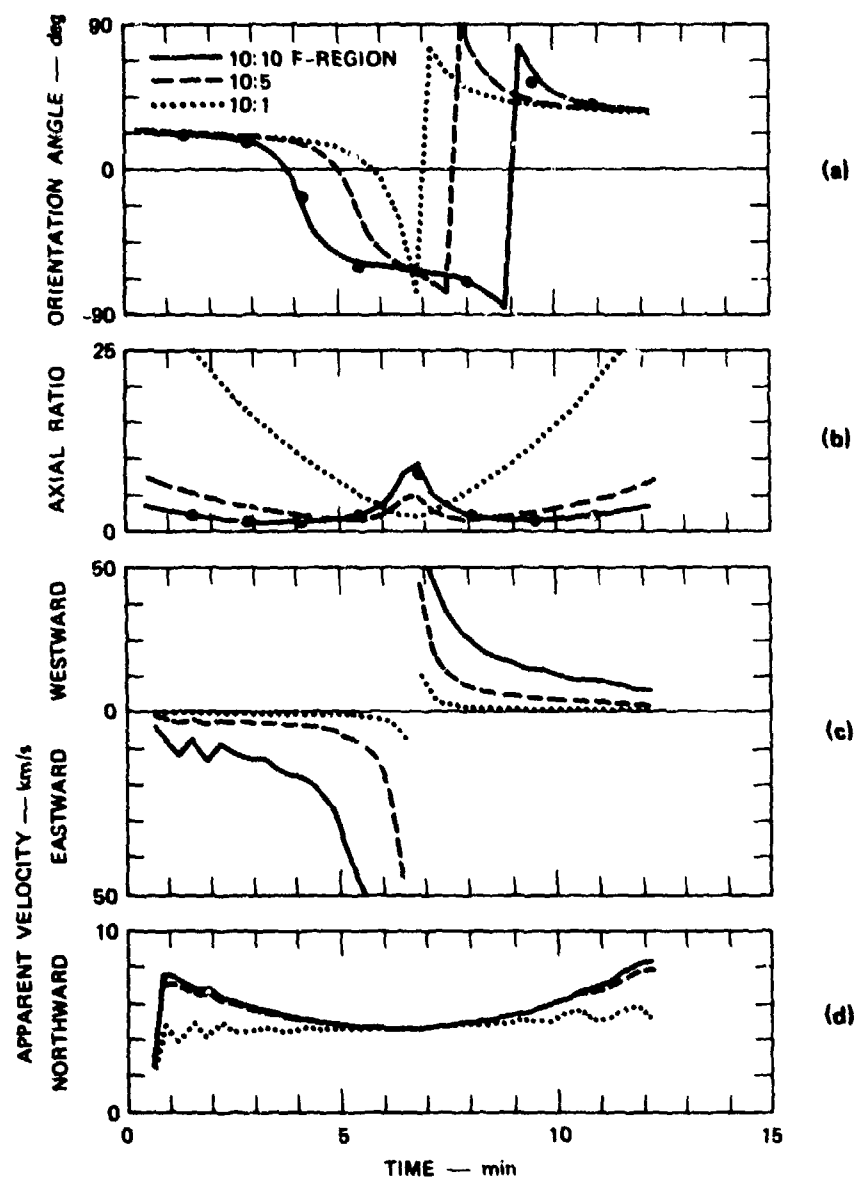
FIGURE 23   THEORETICAL ESTIMATES OF OBSERVED PATTERN ANISOTROPY (a), (b),
AND APPARENT VELOCITY (c), (d), FOR A HIGH-ELEVATION WIDEBAND
PASS AND THREE POSTULATED DENSITY IRREGULARITY STRUCTURES

51

elongation with an axial ratio peak of about 10:1. The
10:5:1 sheet-like structures produce something in between
these extremes.

- The observed correlation ellipse rotates as the line of
  sight comes into the L-shell plane [Figure 23(a)]. For
  rods this change is very rapid, for sheets it is less
  rapid.

- The apparent pattern velocity along the north-south
  baseline [Figure 23(d)], for which we see the prime
  contribution due to satellite motion, is essentially
  the same for both the rod and sheet models during the
  near overhead portion of the pass. At the horizon,
  the rapidly changing axial ratio for the rod model pro-
  duces a reduction in the apparent pattern velocity.

- The large east-west velocity shear due to rapidly chang-
  ing anisotropy [Figure 23(c)] is evident in the model
  calculations. The magnitude of the shear, and to some
  degree its location, is dependent upon the postulated
  anisotropy.

To summarize Figure 23, we have shown parameters measurable
from the observed diffraction pattern that are sensitive to the form of
the ionospheric irregularity structure. Thus, by observing the detailed
structure of these parameters, we can infer the anisotropy of the iono-
spheric irregularities.

At this point, it is important to note that the theoretical
model used to produce Figure 23 assumes homogeneity of the irregularity
structure over the entire region scanned by the satellite pass, some
2000 km. We might realistically expect homogeneity under most moderate
geomagnetic conditions over perhaps five minutes of the pass. Accordingly,
the emphasis in the following examples has been on the center portion of
the pass. Detailed comparison between the model calculations and the
data near the horizons must be made cautiously.

Figure 24 shows the anisotropy parameters and apparent velocities
for Poker Flat ass 12-11, which was recorded during the 1976 rocket cam-
paign. This was a relatively high-elevation pass (maximum elevation 57°)
during mildly disturbed geomagnetic conditions. Superimposed on the
measured axial ratio and orientation angle in Figure 24(a) and (b), are
the theoretical predictions for L-shell aligned 10:10 sheets. The agree-
ment is excellent, with the observed axial ratio enhancement well-matched
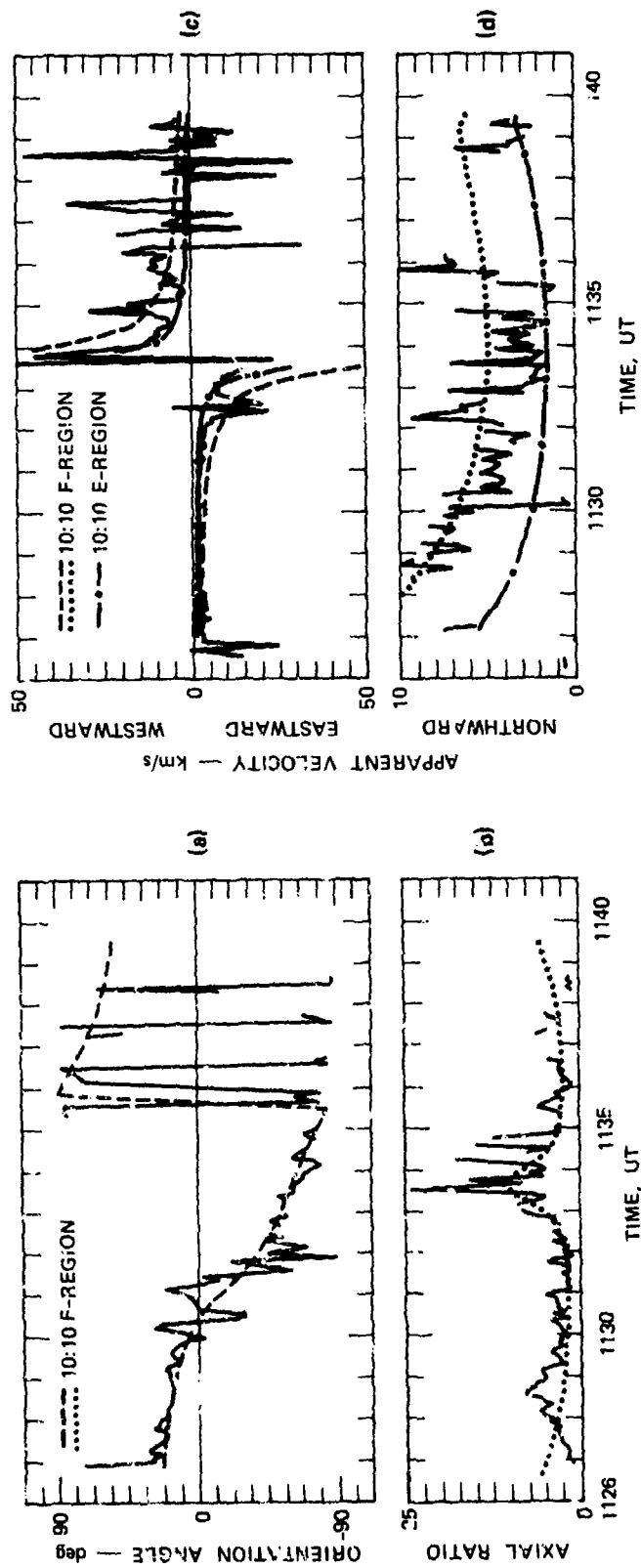
FIGURE 24   MEASURED/THEORETICAL COMPARISON OF OBSERVED PATTERN ANISOTROPY (a), (b), AND APPARENT
VELOCITY (c), (d), FOR POKER FLAT PASS 12-11, 10:10 SHEETS

LA-3793-17B

53

by the theory. Figure 24(c) and (d) shows the apparent east-west and north-south velocities for the same 10:10 sheets and penetration heights of both 120 and 350 km. The east-west shear is bracketed by the predictions for the two heights, although the north-south velocity is underestimated between 1129 and 1133 UT. The rod model, when applied to this case, shows poor agreement with both the axial ratio and orientation angle, and it significantly underestimates the magnitude of the east-west velocity shear.

Figure 25 shows a similar comparison for Pass 12-10 (maximum elevation 58°) earlier on the same evening as Pass 12-11. The comparisons are shown for the same 10:10 sheets as in Figure 24, but here we have also reduced the dimensions of the sheets to 8:4 to get a better agreement with the observed axial ratio and orientation. Figure 25(c) and (d) shows the observed and theoretical apparent pattern velocities for which the agreement is excellent for both the 10:10 and 8:4 models.

The data in Figures 26 and 27 are from two passes early in the experiment operation just before and just following, respectively, a magnetic substorm. For Pass 6-14 (maximum elevation 40°) the correlation orientation match is excellent for 10:10 sheets, and there is some evidence of an axial ratio enhancement near 0911, although the model fit is only fair in this region. The velocity agreements are generally good for 10:10 sheets with a notable exception between 0910 and 0911. Such a discrepancy in both the east-west and north-south directions may be evidence of a localized region in which the drift of the medium is significant enough to be comparable to that produced by the satellite motion. We might further speculate that a local inhomogeneity may also be the reason that the axial ratio match is not good over the entire pass.

Figure 27 is for a somewhat lower elevation (34°) pass to the west of Poker Flat, about an hour after the substorm recovery. The scintillation was close to uniform throughout the pass and we see excellent agreement between the measured anisotropy parameters and apparent velocities for 10:10 sheets. There is some departure, both in the axial
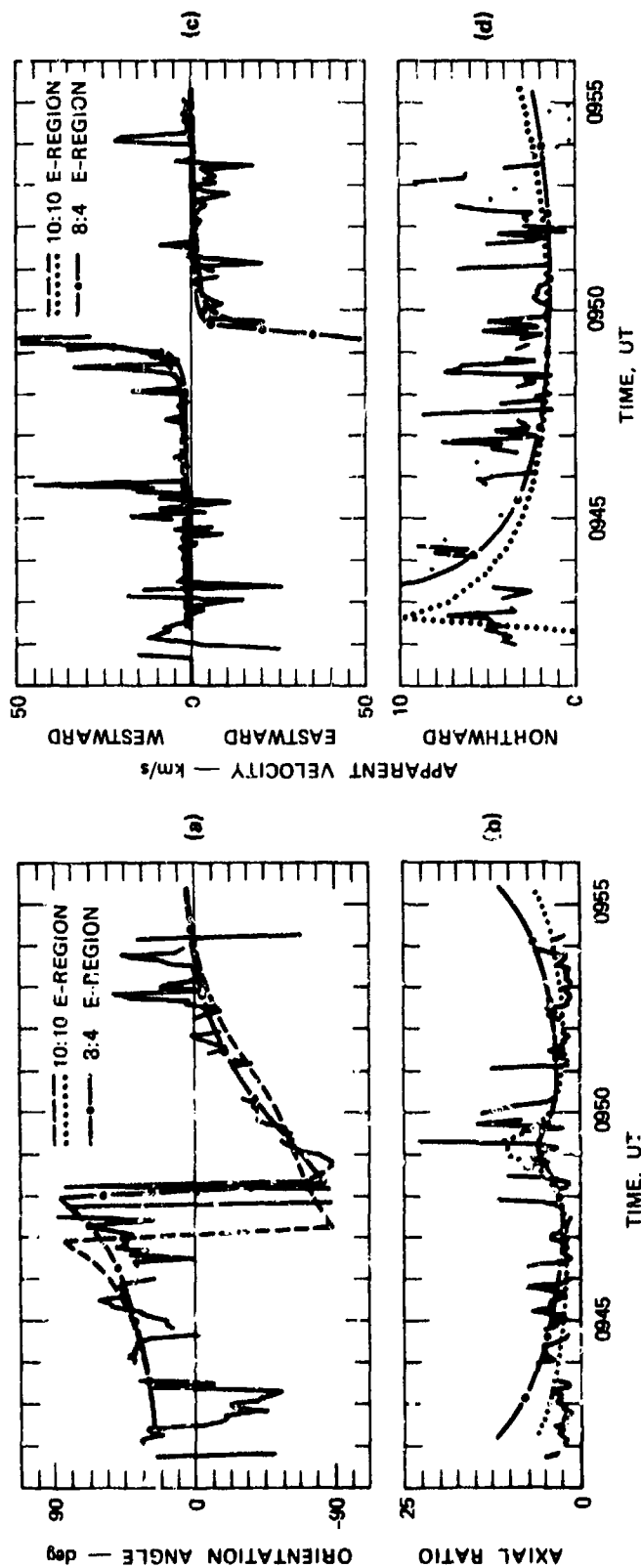
54

FIGURE 25   MEASURED/THEORETICAL COMPARISON OF OBSERVED PATTERN ANISOTROPY (a), (b), AND APPARENT VELOCITY (c), (d), FOR POKER FLAT PASS 12-10, 10:10 SHEETS, 8:4 SHEET-LIKE STRUCTURES

55
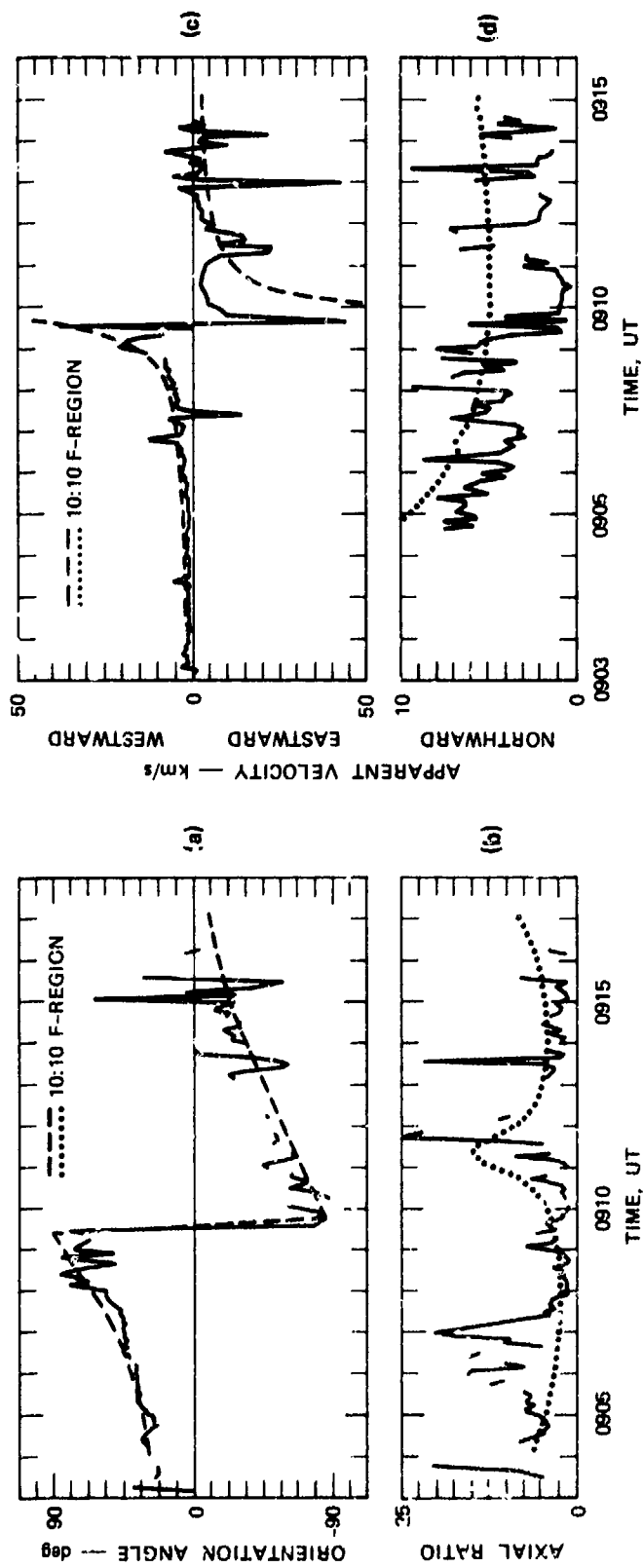
FIGURE 26 MEASURED/THEORETICAL COMPARISON OF OBSERVED PATTERN ANISOTROPY (a), (b), AND APPARENT VELOCITY (c), (d), FOR POKER FLAT PASS 6-14, 10:10 SHEETS
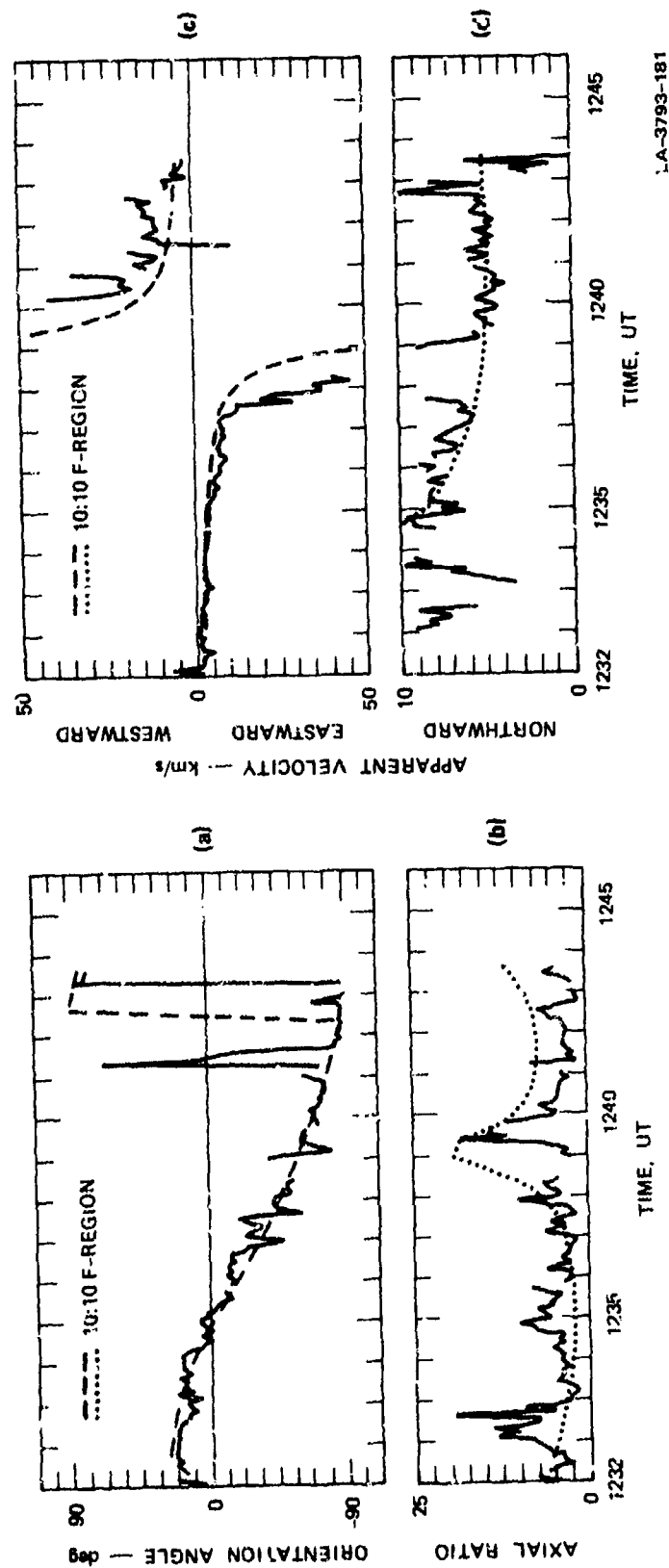
LA-3793-180

FIGURE 27   MEASURED/THEORETICAL COMPARISON OF OBSERVED PATTERN ANISOTROPY (a), (b), AND APPARENT
VELOCITY (c), (d), FOR POKER FLAT PASS 6-14, 10:10 SHEETS

57

ratio and velocities, between 1238 and 1239. This is likely to be another localized region in which the irregularity structure and motion differ from the surrounding medium.

4. Summary

In these passes, and in several more that have been analyzed in detail, there is strong evidence for L-shell-aligned, sheet-like irregularities at high latitudes. This evidence is seen both in the observed pattern anisotropy, i.e., axial ratio and orientation angle, and in the apparent velocity signature, both of which are sensitive functions of the in situ structure. So far, the detailed analysis has been completed only on passes recorded during mild-to-moderate geomagnetic activity. To develop a measure of the morphological dependence of the ionospheric structure, many additional passes will have to be analyzed, encompassing a variety of geomagnetic conditions. This work is currently underway.

C. Auroral Total Electron Content

The total electron content (TEC) boundary between the diffuse aurora and high-latitude plasma trough has been identified (BPR 6) as a repeatable feature that is often associated with scintillation. The relationship of the boundary and the geometry to enhanced scintillation has been discussed previously (BPR 6). The nature of the TEC boundary and its long-term behavior have been studied also. The poleward TEC boundary of the trough is evident in much of the Poker Flat data near local midnight. Wideband measurements of the trough from Poker Flat are especially well-suited to describing the details of the boundary, since it often is nearly over- head. Some 200 passes have been examined in terms of trough TEC behavior. Many of these were from summer and fall 1976.

The data are treated by displaying TEC corrected for ionospheric obliquity at an estimated height of 120 km compared to the L-value of

the assumed E-region intersection point. Typical results are given in Figures 28, 29, and 30. The three progressive passes of Figure 28 show a step change in content of a factor of 3 to 4 with an intersection point change of 325 km (L of 4.5 to 5.4). Much sharper boundaries are observed, as in Figure 29, but those of Figures 28 and 30 should be considered typical. It is also common to find an enhancement of TEC at the poleward edge of the boundary as shown in the earliest pass of Figure 28. The unusually stable position and details of the boundary sequence in Figure 29 for passes from east to west reinforces the idea of repeatability of the phenomena.

A search for magnetically quiet data found a small data set typified by that d splayed in Figure 30. When no magnetic activity occurs, then the boundary region drifts southward (to lower L-values) during the post-midnight hours. This behavior would be expected from the known pattern of the auroral oval as seen from Poker Flat. The few examples found all showed the equatorward drift in the expected magnitude. The boundary
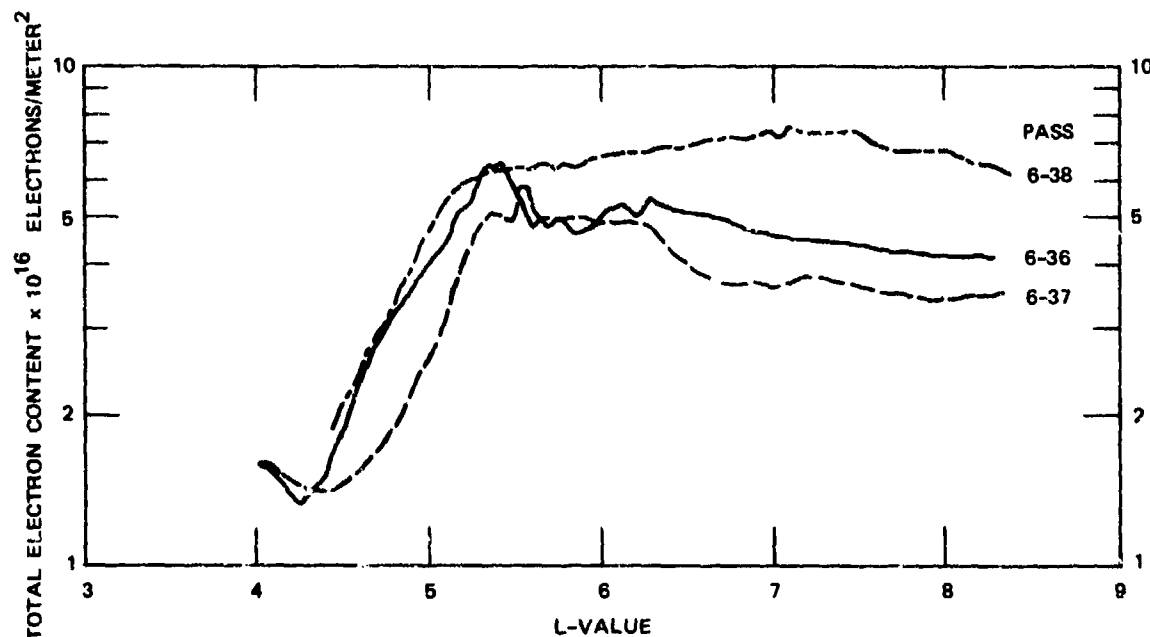
LA-3793-182

FIGURE 28   TEC BOUNDARY FOR NIGHTTIME WIDEBAND PASSES ON 17 JULY 1976
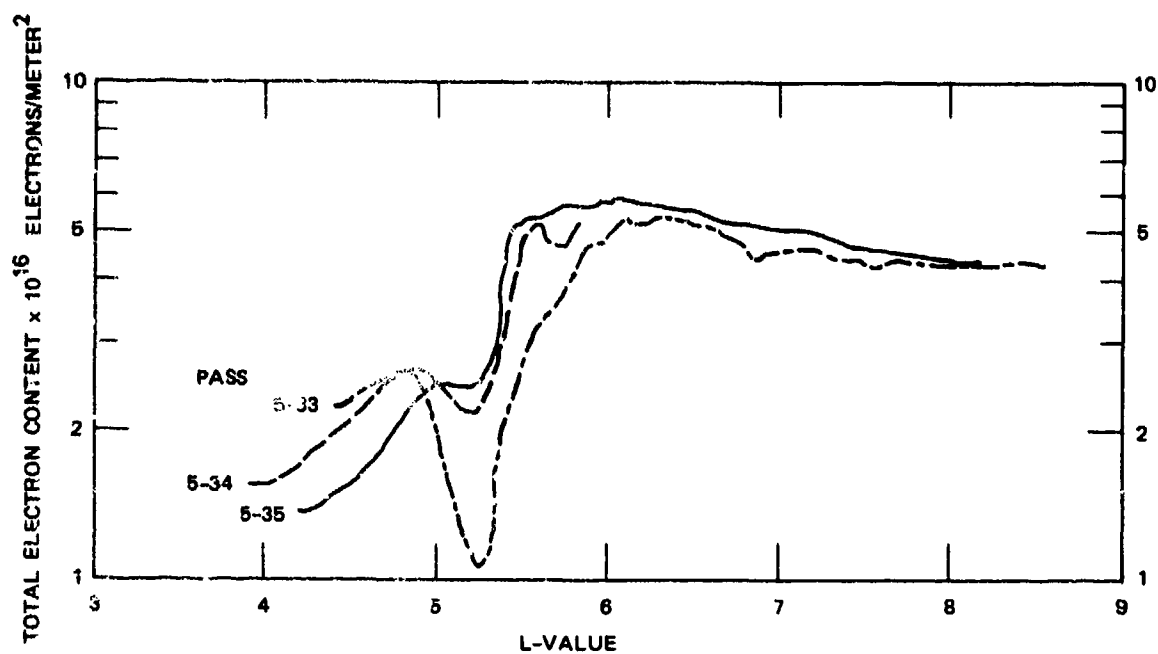
FIGURE 29   TEC BOUNDARY FOR NIGHTTIME WIDEBAND PASSES ON 4 JUNE 1976
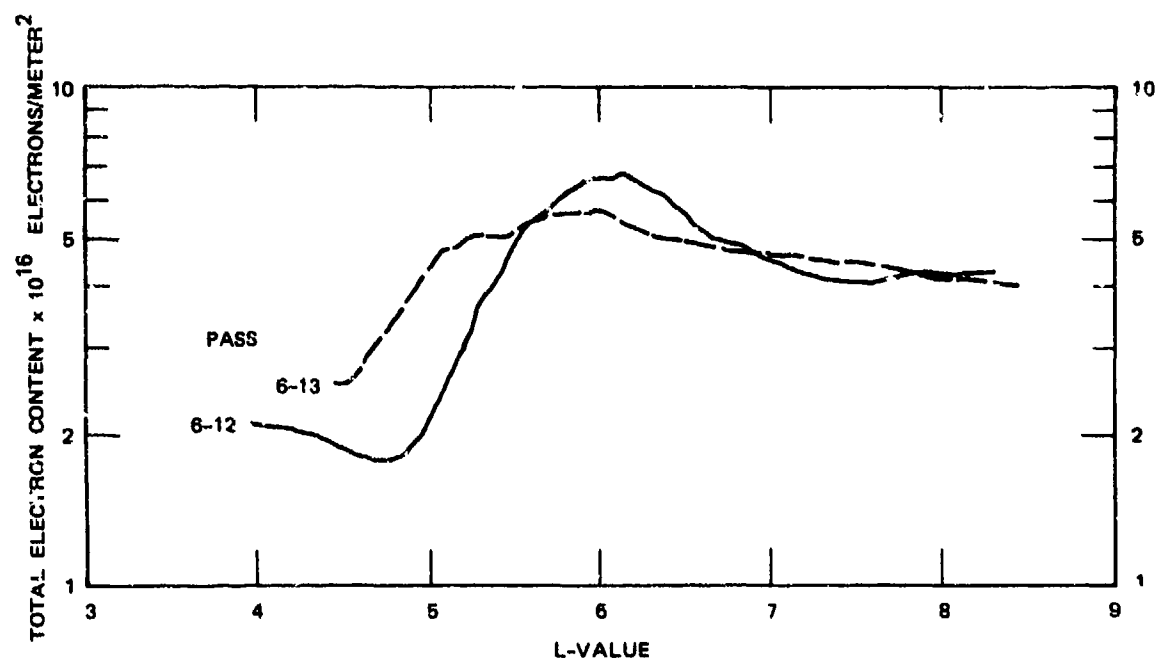
FIGURE 30   TEC BOUNDARY FOR NIGHTTIME WIDEBAND PASSES ON 26 JUNE 1976

positions as a function of time have been plotted in Figure 31 to illustrate this feature of the quiet-time data.

Consideration of magnetically active periods a' so reveals a not-unexpected result for the position of the poleward trough boundary. That is, higher magnetic activity pushes the boundary southward while lower activity allows an expansion or relaxation. Figure 32 plots the L-value of the boundary against magnetic activity scaled from the H-component College magnetogram at the time of the pass. The scaled values are proportional to deviation from the magnetometer zero line so that smaller values indicate greater activity. This very rough estimate of the immediate state of activity appears to connect closely with the observed boundary position. Seasonal variations are seen by comparing data from different months.
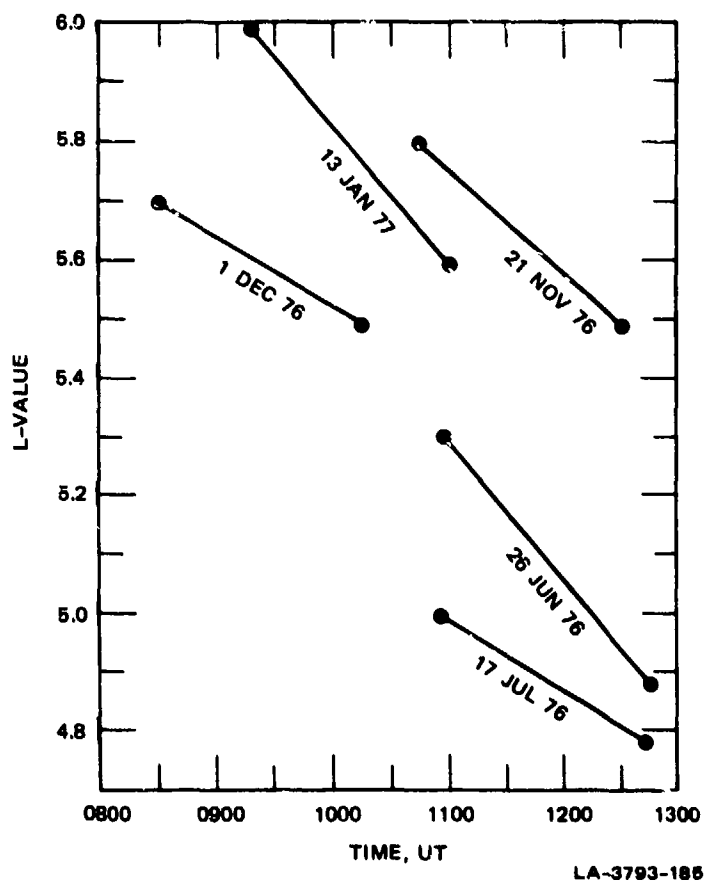
LA-3793-185

FIGURE 31   TEC BOUNDARY POSITION COMPARED TO TIME
FOR MAGNETICALLY QUIET CONDITIONS

61
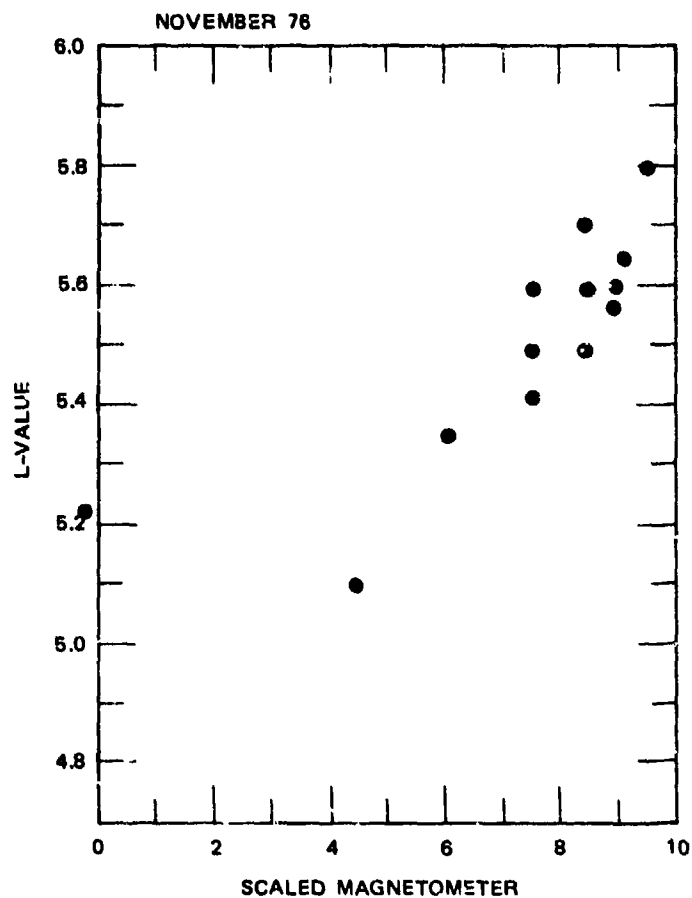
NOVEMBER 76

FIGURE 32 BOUNDARY POSITION COMPARED TO LOCAL
MAGNETIC ACTIVITY AS SCALED FROM
COLLEGE MAGNETOMETER DATA

Continued work will analyze more of the available data base to
further develop the quiet, active, and seasonal behavior of the boundary
as well as further details of its structure and its relation to auroral
scintillation.

V EQUATORIAL SCINTILLATION

A. General Characteristics

The most consistent feature in the equatorial scintillation is the
pronounced seasonal dependence, as noted in Section III. Scintillation
activity diminishes rapidly at Ancon around April, which marks the end
of the summer period in the southern hemisphere. Similarly, the scin-
tillation activity at Kwajalein diminishes rapidly around September.
The onset of the active period occurs around April at Kwajalein and
October at Ancon.

At the present time it is not clear if there is a genuine local
summer maximum at the equator stations or simply a filling in of the
activity between equinoctial maxima. The detailed morphology of the
equatorial scintillation remains, therefore, somewhat uncertain, and
the subject is currently being actively studied.

The structure of the equatorial scintillation itself is characterized
by the fact that for a given level of amplitude scintillation there is
less associated phase scintillation when compared with auroral scintilla-
tion of the same fading level. A good example of this effect is shown
in Figure 9 of BPR 3. We believe that this difference is real, although
it must be kept in mind that the level of phase scintillation is dependent
upon the detrender cutoff.

Indeed the fading rate is typically slower for the equatorial data
when compared with the high-latitude data. Thus, since we are using a
fixed detrend filter cutoff, more phase structure is removed in the
equator data than in the auroral data. Nonetheless, we expect the
equatorial irregularities to develop at higher altitudes than the
auroral irregularities. Moreover, there is some evidence of a "flattening"
of the equatorial phase spectrum, i.e., spectral index values $p \gtrsim -2.5$,
whereas the auroral data typically show $-3 < p < -2.5$. Both higher

altitudes and flatter spectra act to produce more amplitude scintillation for a given level of phase scintillation.

The equatorial data are of particular interest from the communications standpoint because of the extremely severe fading conditions that can occur. Slow deep fades with a high degree of spatial and frequency coherence are particularly troublesome because mitigation through diversity is quite difficult. Two examples of slow deep fading recorded at the Kwajalein station are shown in Figure 33. These are the only available examples of this phenomenon. Moreover, to characterize such events requires special processing, which will be done in the near future.

The more typical extreme equatorial scintillation event is the development of very intense and rapid scintillation that persists into the gigahertz range. An example from Ancon Pass 35-12 that has been analyzed in some detail was presented in BPR 5. It was found, however, that the very rapid phase scintillation was producing "phase jumps" when processed at the 100-Hz rate. The data have since been reprocessed at the 500-Hz rate. An example of the frequency decorrelations that can occur is shown in Figure 34.

To show the relative frequency of occurrence of gigahertz scintillation events, we have plotted as thin vertical lines the local time of all recorded nighttime passes compared to date for Ancon and Kwajalein in Figures 35 and 36, respectively. The shaded areas designate times at which the S_4 index exceeded 0.2 at 1239 MHz. The number of such events is somewhat higher at Ancon, although the longitudinal/seasonal dependence undoubtedly plays a role here. Some additional characteristics will be discussed in Section V-B.

To conclude this subsection, we show several examples of gigahertz scintillation events at Ancon, together with the standard spectral summary parameters. The data are shown in Figures 37 through 42. As a general rule, whenever the T parameter (measured at VHF) achieves a value of 0 dB or higher, there is a significant level of gigahertz scintillation present.

64
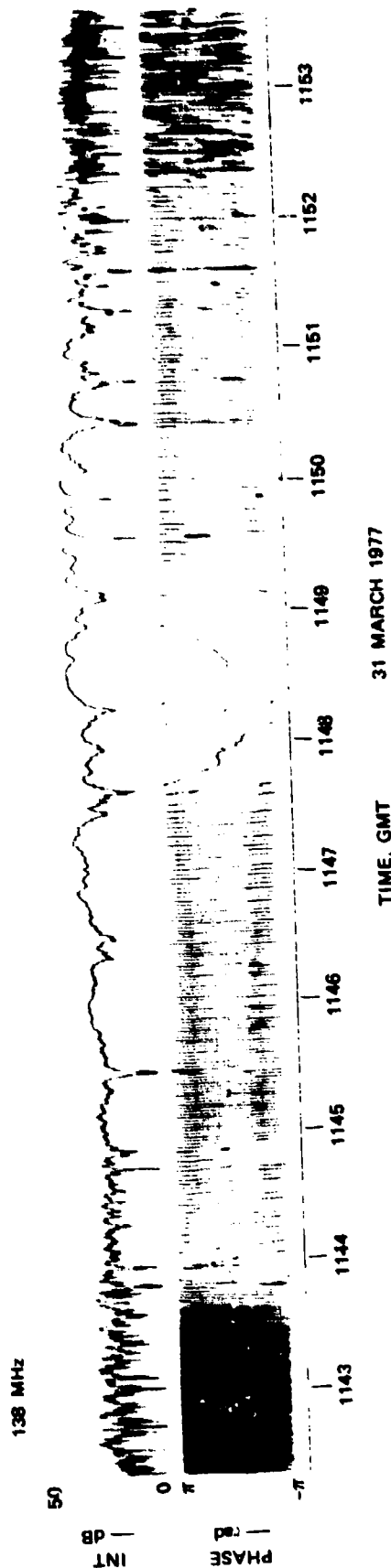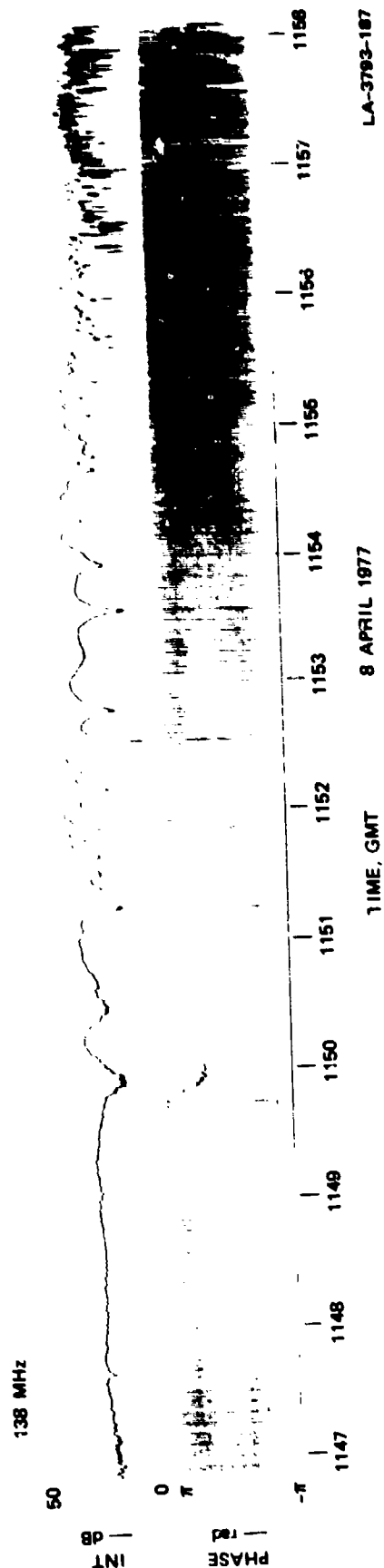
FIGURE 33   EXAMPLES OF UNUSUAL DEEP, SLOW FADING

$$\rho'_1 = \frac{\left\langle (I_a - \langle I_a \rangle)(i_b - \langle I_b \rangle) \right\rangle^{1/2}}{\sqrt{\sigma_{I_a} \sigma_{I_b}}}$$

0447:20
to
0447:40

$\Delta f = 11.5$ MHz

$\Delta f = 22.9$ MHz

$\Delta f = 34.4$ MHz

$(\Delta f = 57.4$ MHz)

$\Delta f = 45.9$ MHz

$\Delta f = 66.8$ MHz

FREQUENCY — MHz
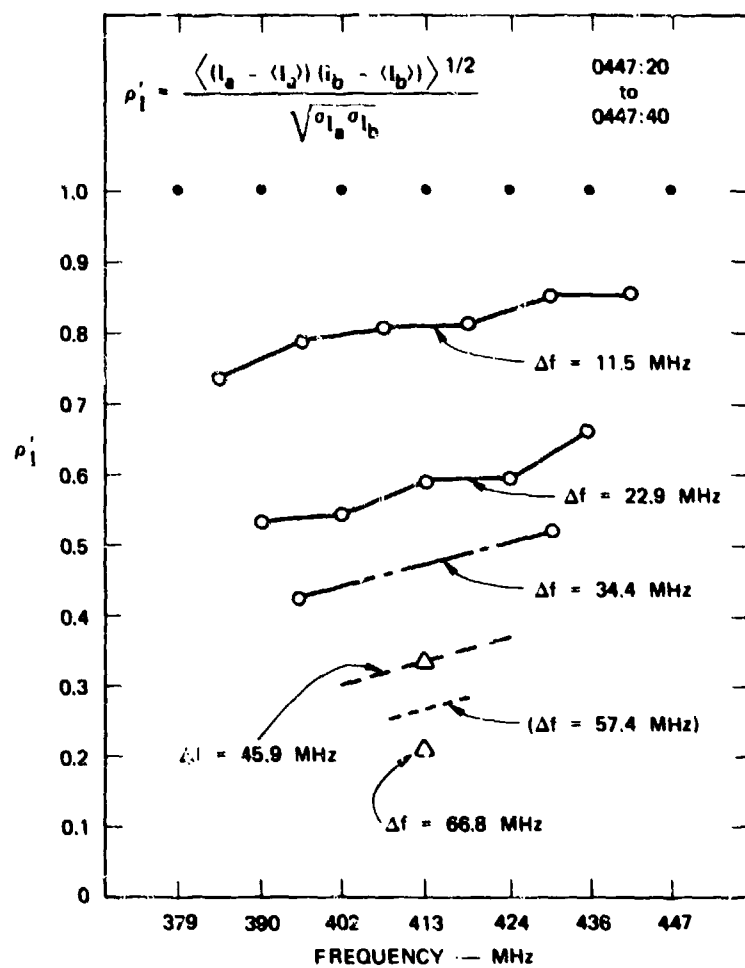
LA-3793-188

FIGURE 34   EXAMPLE OF INTENSITY DECORRELATION UNDER
CONDITIONS OF SEVERE EQUATORIAL SCINTILLATION
(Ancon Pass 35:12)

66
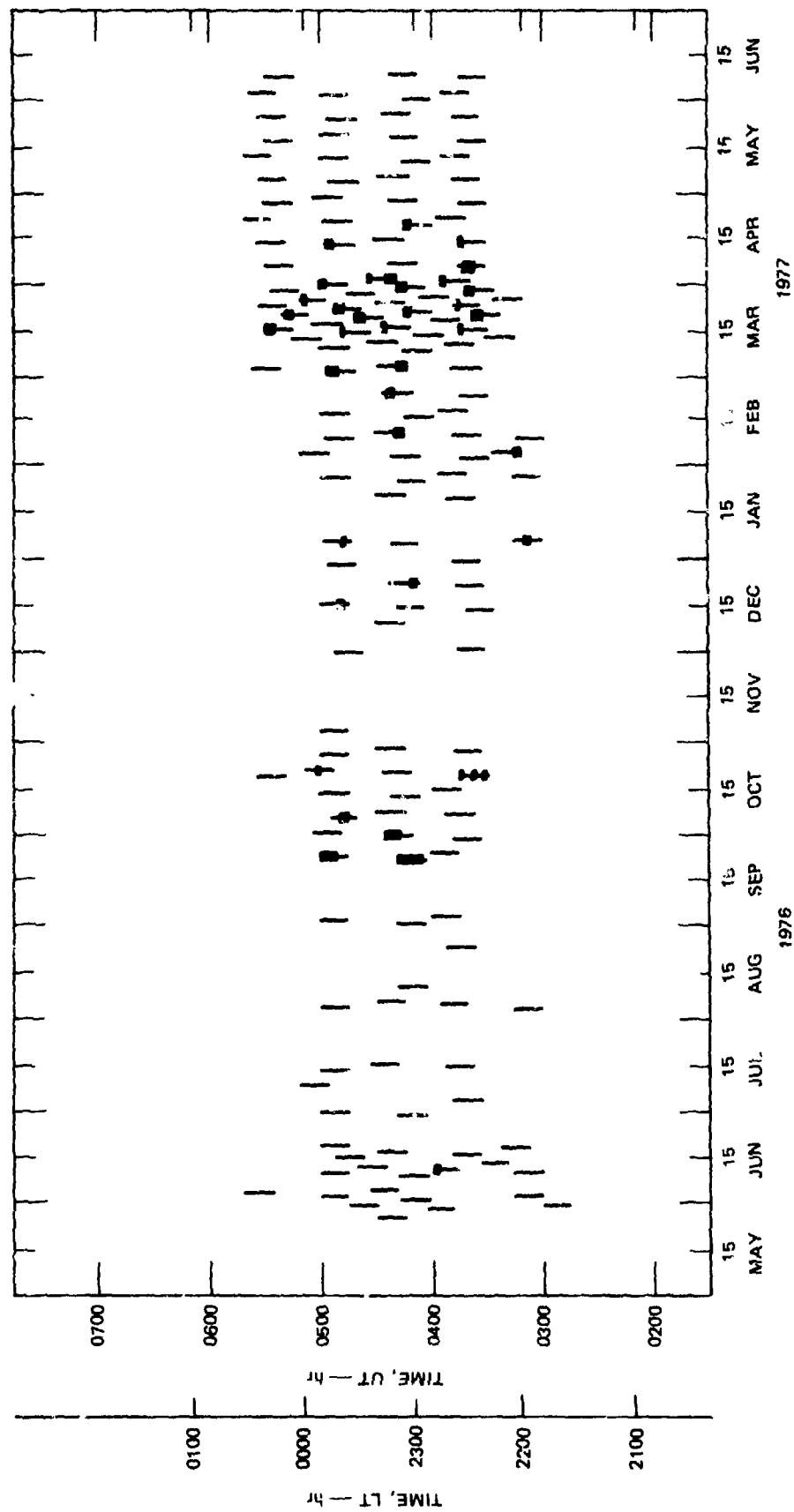
FIGURE 35   NIGHTTIME PASSES RECORDED AT ANCON.   The shaded times indicate $S_4 > 0.2$ at 1239 MHz.

LA-3793-139

67
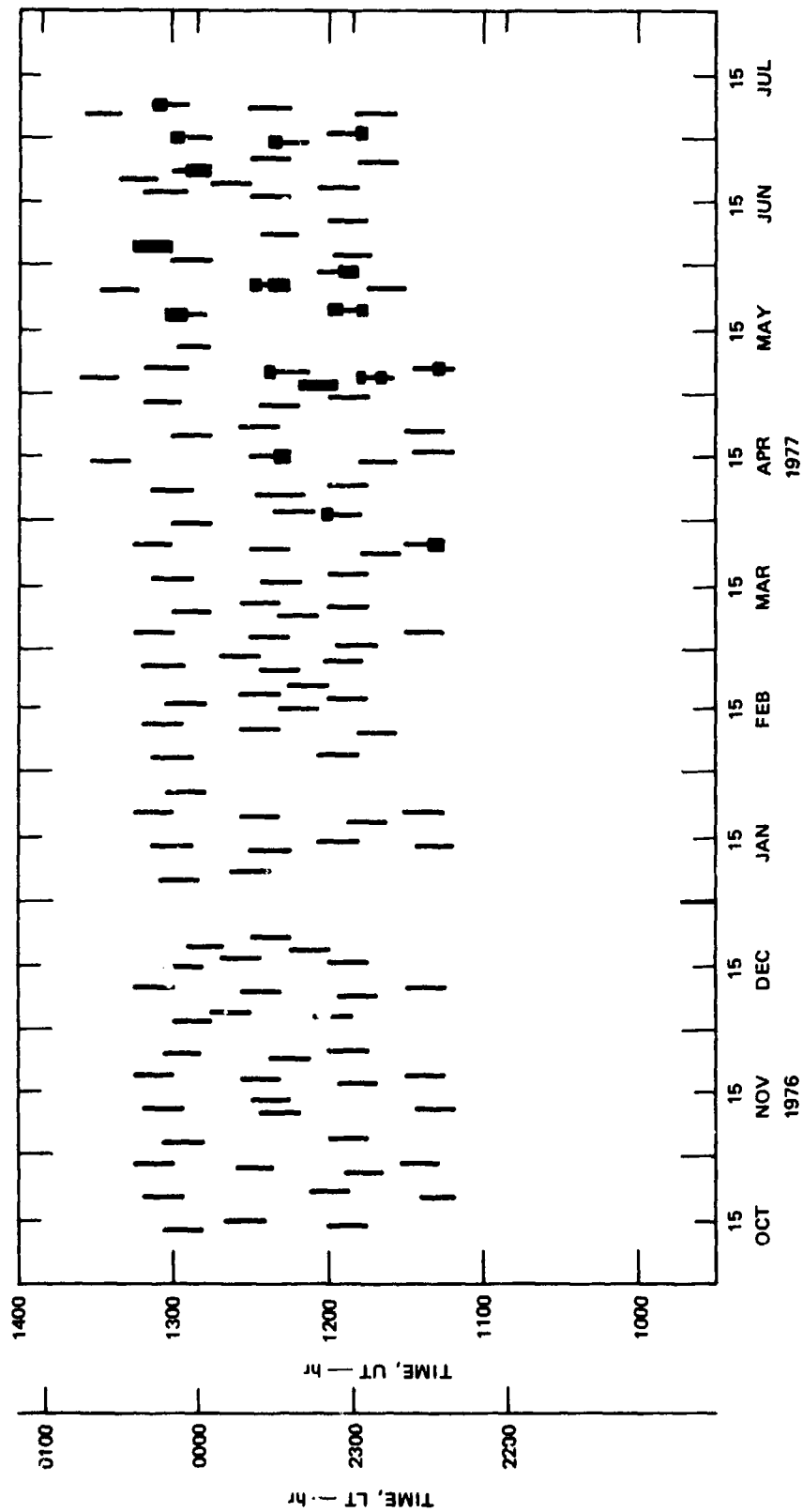
FIGURE 36 NIGHTTIME PASSES RECORDED AT KWAJALEIN. The shaded times indicate $S_4 > 0.2$ at 1239 MHz.

LA-3793-190

68
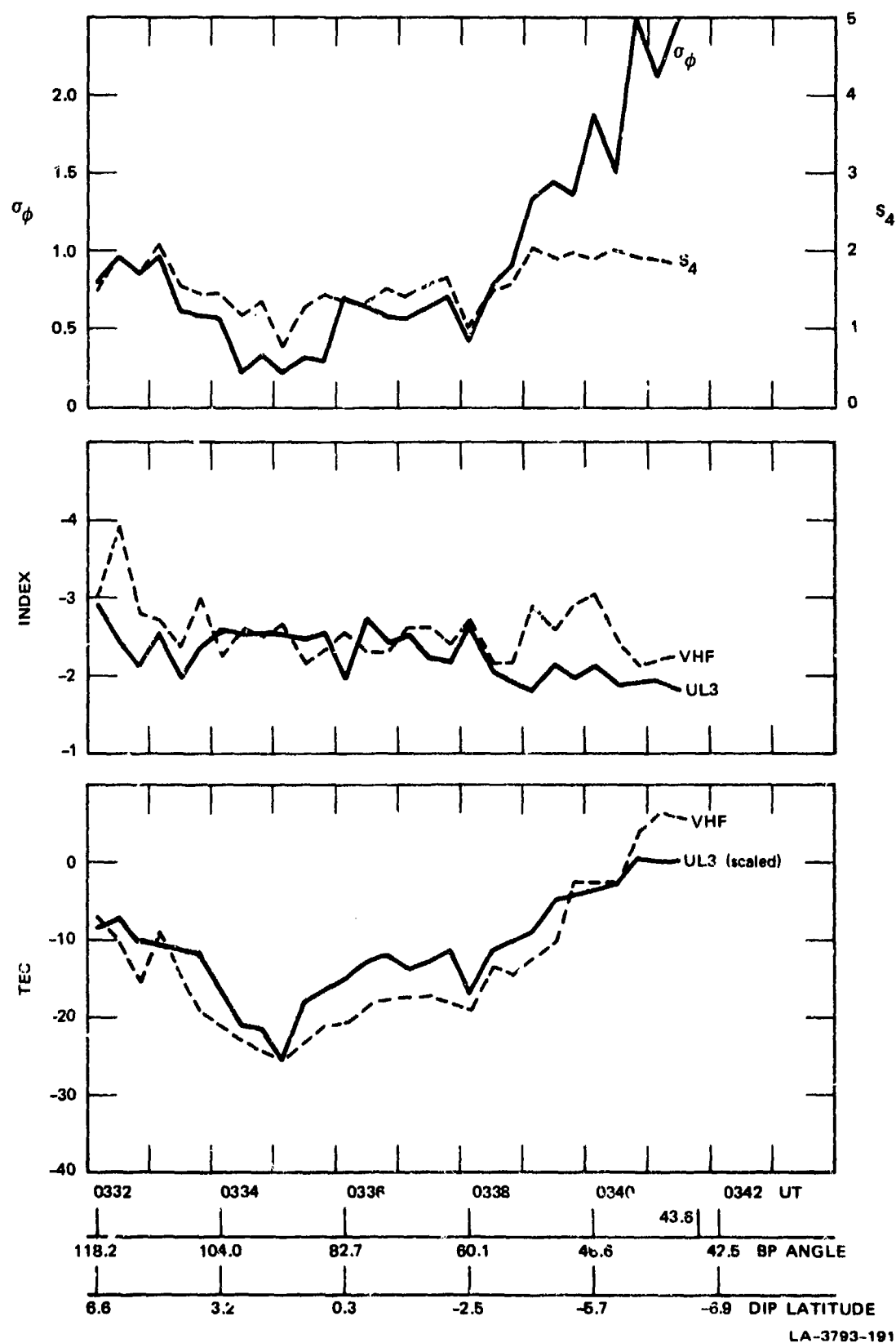
FIGURE 37   PHASE SPECTRAL SUMMARY PARAMETERS FOR ANCON PASS 28-39
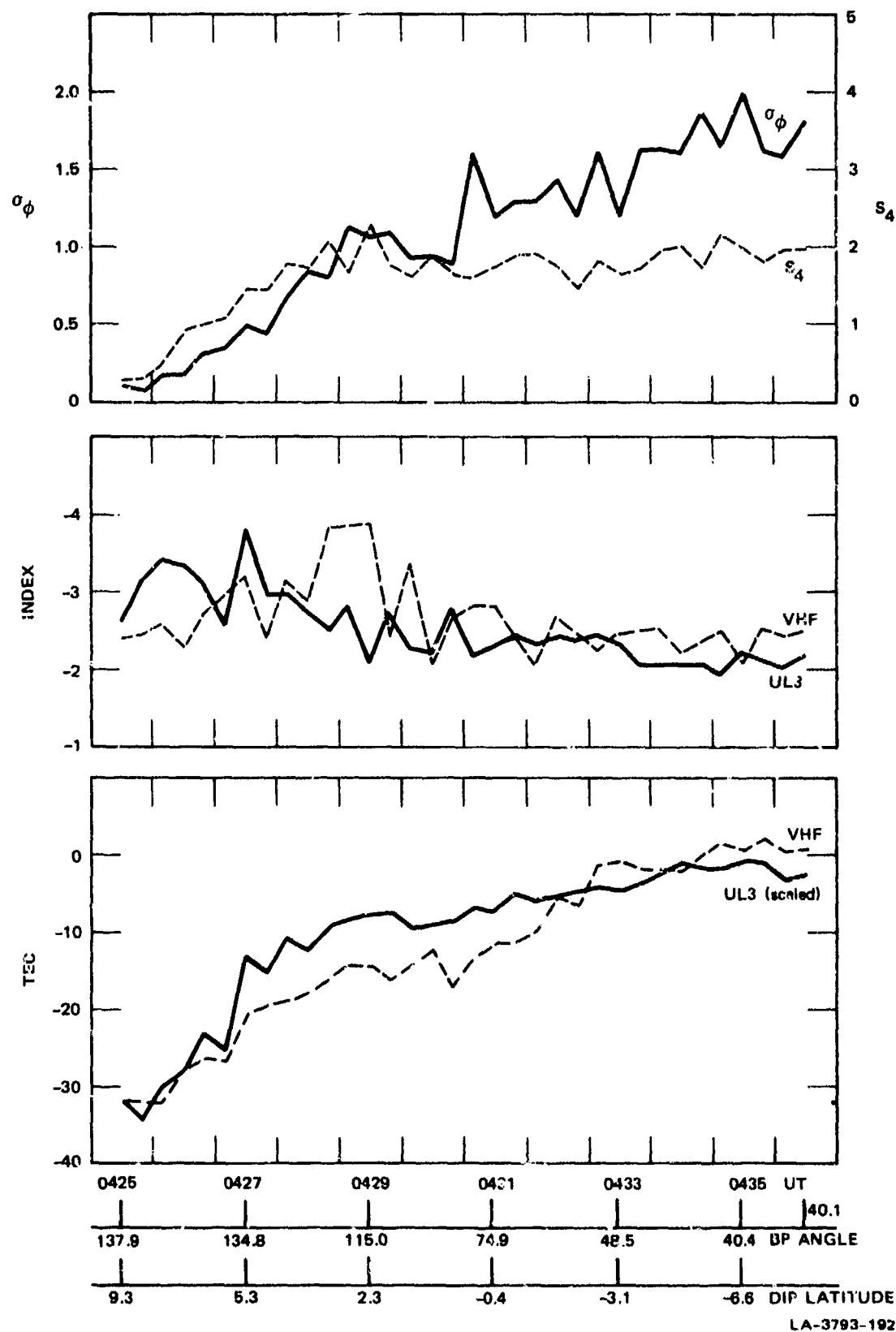
FIGURE 38   PHASE SPECTRAL SUMMARY PARAMETERS FOR ANCON PASS 28-49

70
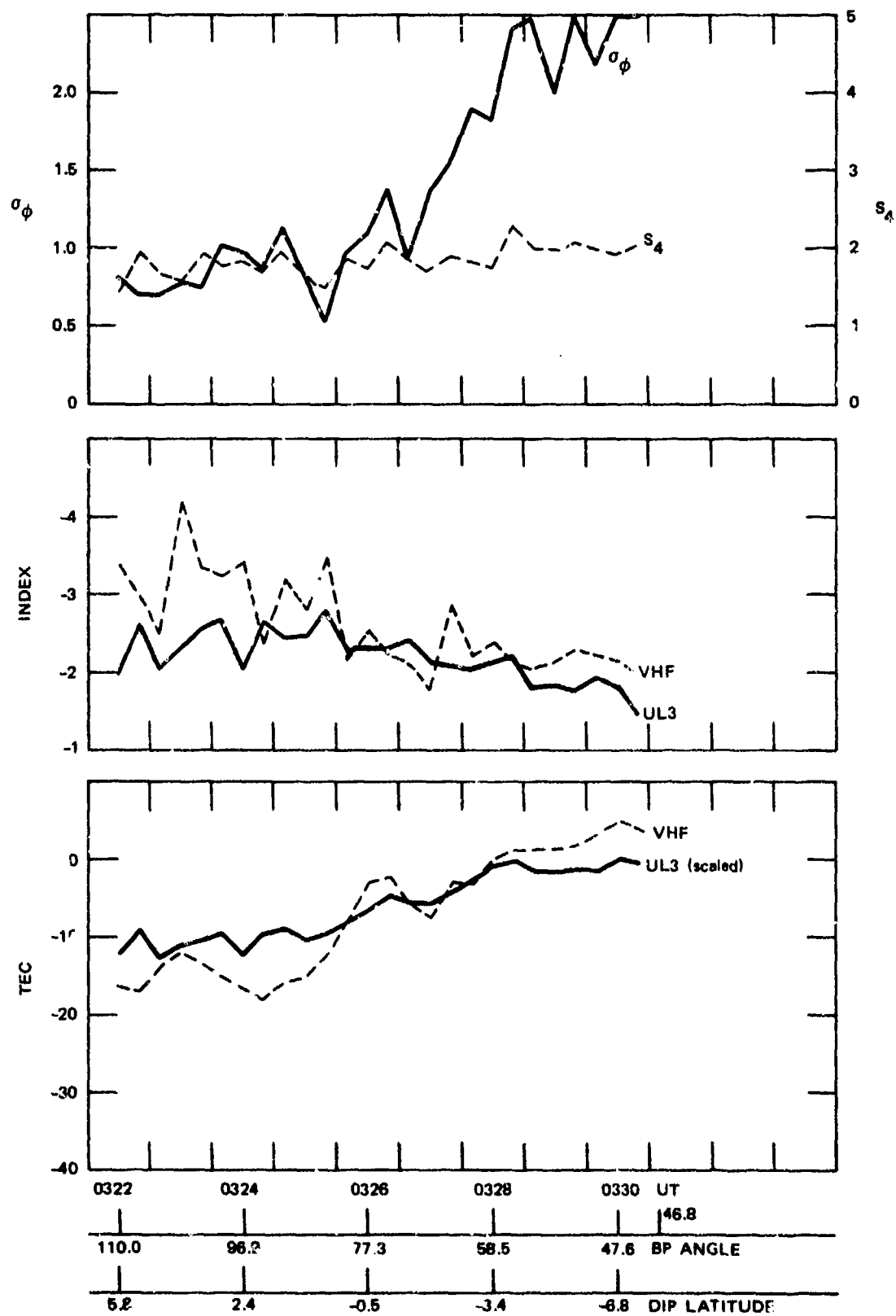
FIGURE 39   PHASE SPECTRAL SUMMARY PARAMETERS FOR ANCON PASS 28-50

71
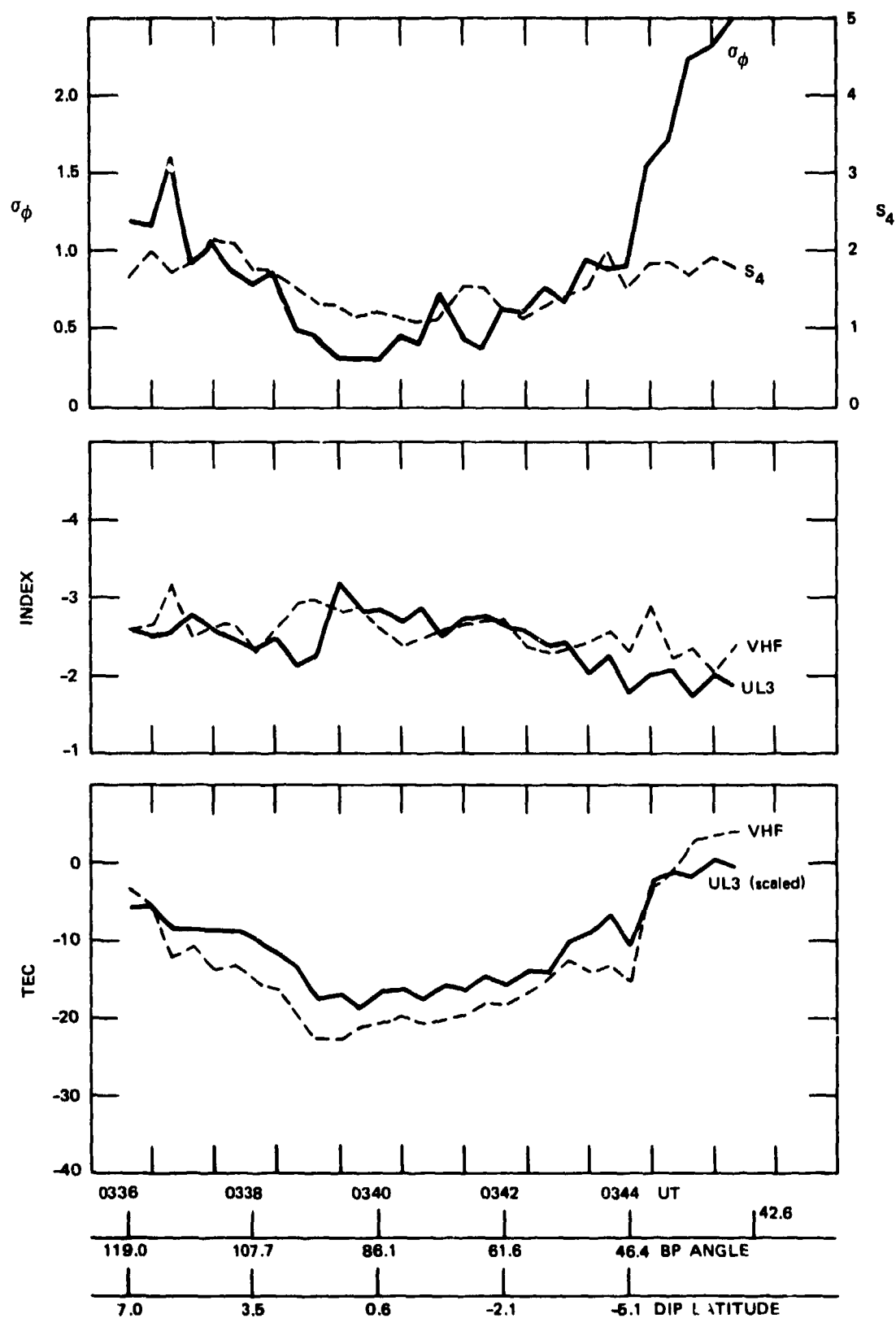
LA-3793-194

FIGURE 40   PHASE SPECTRAL SUMMARY PARAMETERS FOR ANCON PASS 29-7

72
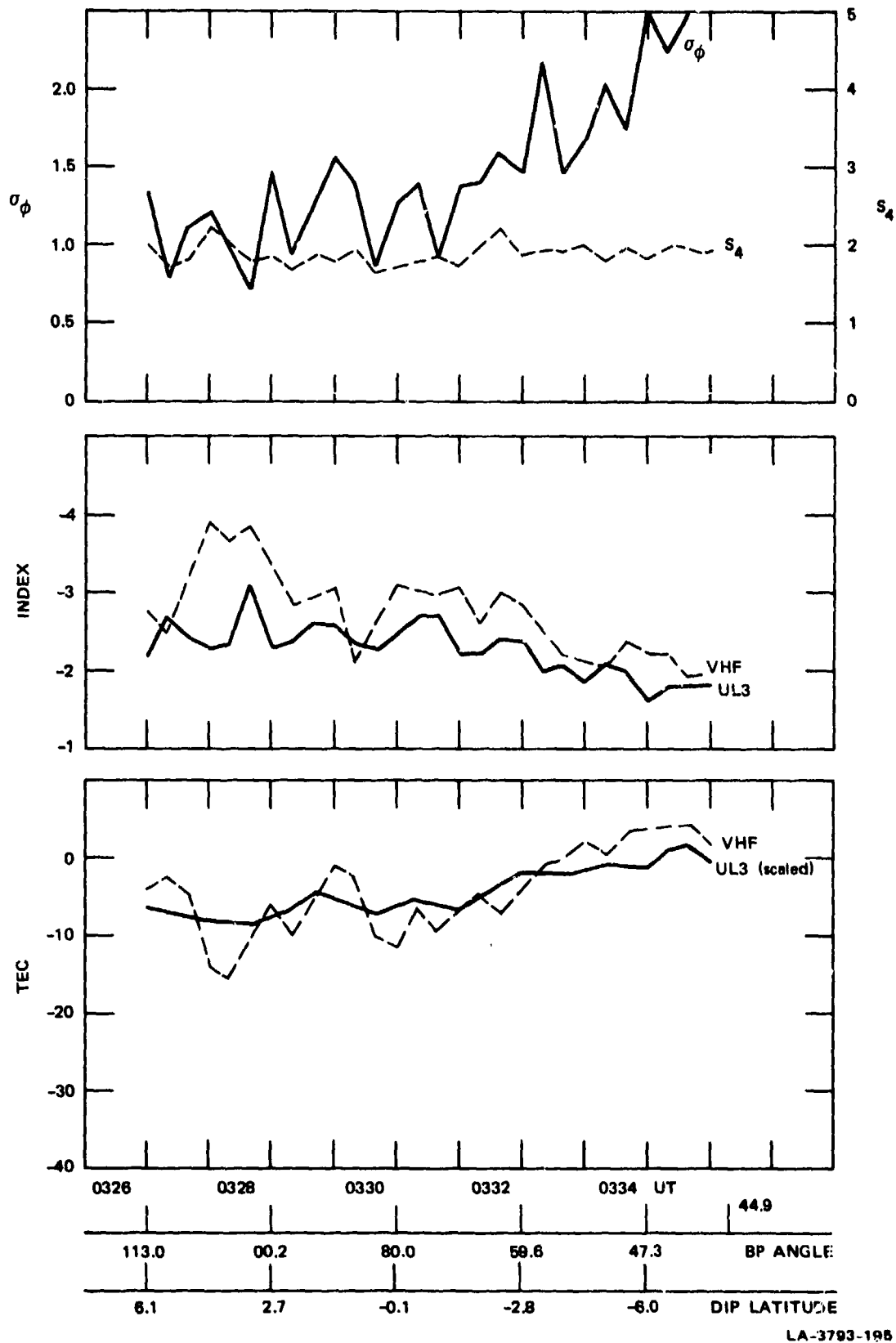
FIGURE 41   PHASE SPECTRAL SUMMARY PARAMETERS FOR ANCON PASS 29-18

73
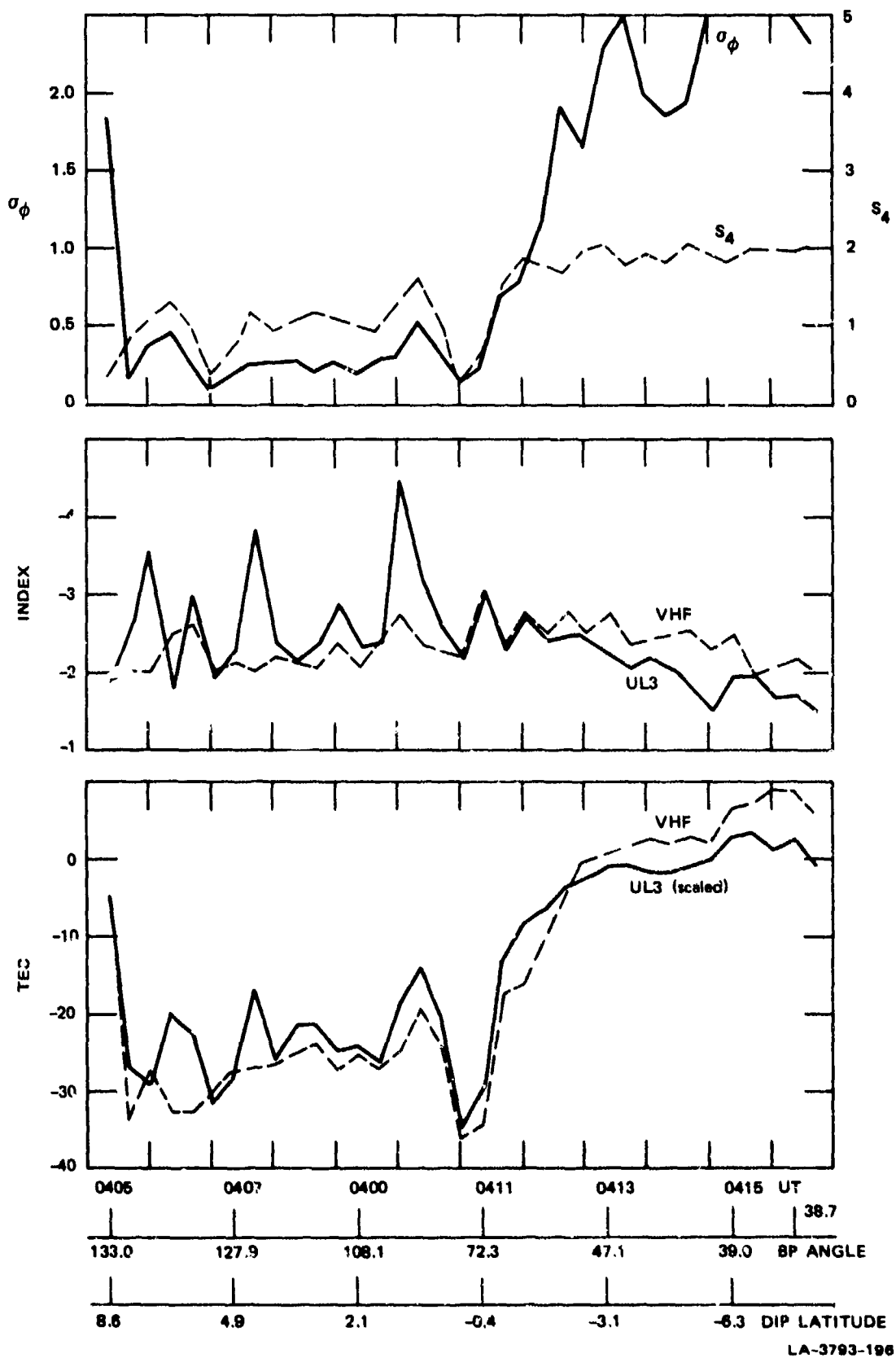
FIGURE 42   PHASE SPECTRAL SUMMARY PARAMETERS FOR ANCON PASS 29-21

74

In each case the slope of the phase spectrum systematically flattens such that $p \gtrsim -2$ as the intensity of the perturbation increases.

Now, while it is true that significant diffraction effects are present in both the VHF and UHF spectra, we believe that this flattening genuinely indicates the generation of more small-scale structures, relative to the larger structures when compared with less-disturbed cases. This conclusion is supported by the analysis in Section IV-A, where it was shown that even in the presence of obvious diffraction effects and/or phase jumps in the signal phase, the shape of the phase spectrum is preserved over the region where most of the spectral phase contribution occurs.

Thus, while a considerable amount of theoretical work has been applied to the equatorial gigahertz phenomenon, ultimately the parameters that control the spectral index of the turbulent irregularities must be considered. Indeed, flattening the spectral distribution of the irregularities is an intuitively satisfying way of generating amplitude scintillation in the gigahertz frequency range.

B.   The Equatorial Scintillation Campaign

All of the routine data processing through the display of summary tapes, including spectra, has been completed for the special operations at Ancon during March 1977 (see BPR 6). The several cases showing significant S-band scintillation and spectral decorrelation at UHF have been the focus of initial attention, since they represent the most extreme conditions. From additional processing of the entire data set, we have displayed scintillation index compared to the F-region propagation path intersection point in simple geographic coordinates. Several passes are illustrated in Figure 43, which also shows the intersection points for the geosynchronous beacons monitored by AFGL from Huancayo and Ancon during the March experiment. This is the first step in comparing coordinated measurements from Wideband, AFGL, and Jicamarca.
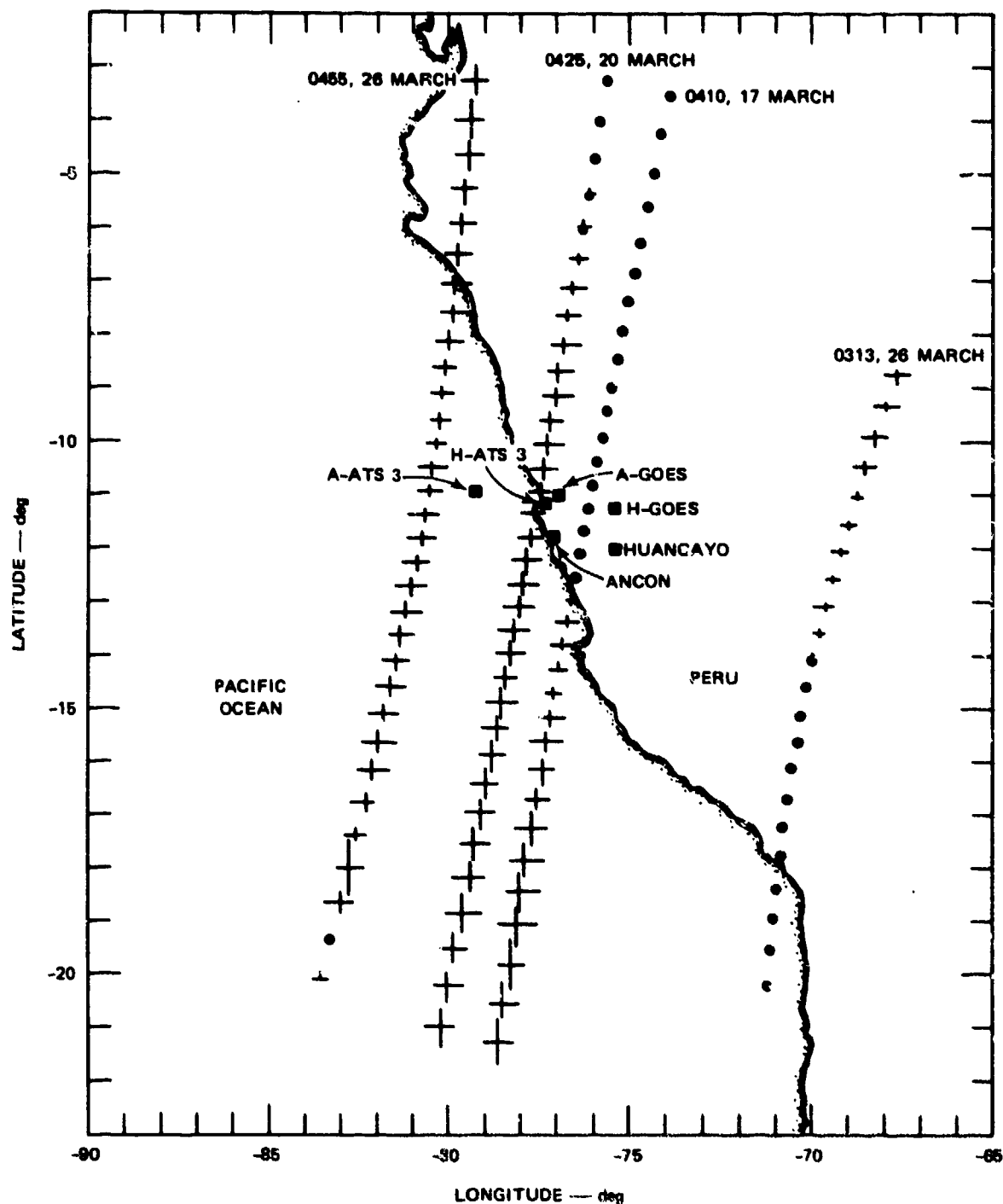
FIGURE 43   WIDEBAND PASS F-REGION INTERSECTION POINTS FOR THE SELECTED
             CASE STUDY PASSES

In putting together coordinated measurements, each participant must be aware of the strengths and weaknesses of the various data sets as well as their availability. For example, the Wideband data covers a short time period but takes a much broader spatial sample than the other ground-based instruments that excel in describing temporal variations of the scintillation-producing region. A similar consideration applies to comparisons of the AE satellite data and the Jicamarca radar data that describe the ionospheric composition compared to position, and irregularity structure compared to time, respectively. Data from the all-sky 6300 Å photometer system showed dark bands apparently connected with depleted ionization and disturbed propagation. These data promise to correlate well with the diverse scintillation and structure measurements.

A clear objective arising from the coordination is to coherently combine all available data for several case studies showing the nature and evolution of the disturbed ionospheric region. It is hoped that ultimately such a synthesis will be suggestive of the as-yet-not-understood physical processes occurring in the disturbed equatorial ionosphere.

The UT dates March 17, 20, and 26 have been selected for detailed case studies. These were selected because they show strong scintillation with on and off periods so that the progression of a clearly defined scintillation-producing region can be traced. Figure 44 illustrates the complementary relationship between the Wideband and AFGL scintillation data (provided to us by Dr. Aarons) in time, space, and intensity. The sequence of scintillation records clearly indicates a series of disturbed regions moving eastward at about 83 m/s (F-region, 350 km).

The longitudinal and temporal changes associated with scintillation changes in the Wideband data are very closely coupled to the AFGL obser-vations that fall mainly in the latitude range of 9° to 11° south. However, the Wideband pass probes the ionosphere from 3° to 21° south (see Figure 45). Thus a homogeneous latitudinally extended scintillating region is suggested by these data. Further analysis will involve the other coordinated data and will develop the time and space history of the definable regions. Figure 45 also suggests that a detailed comparison of
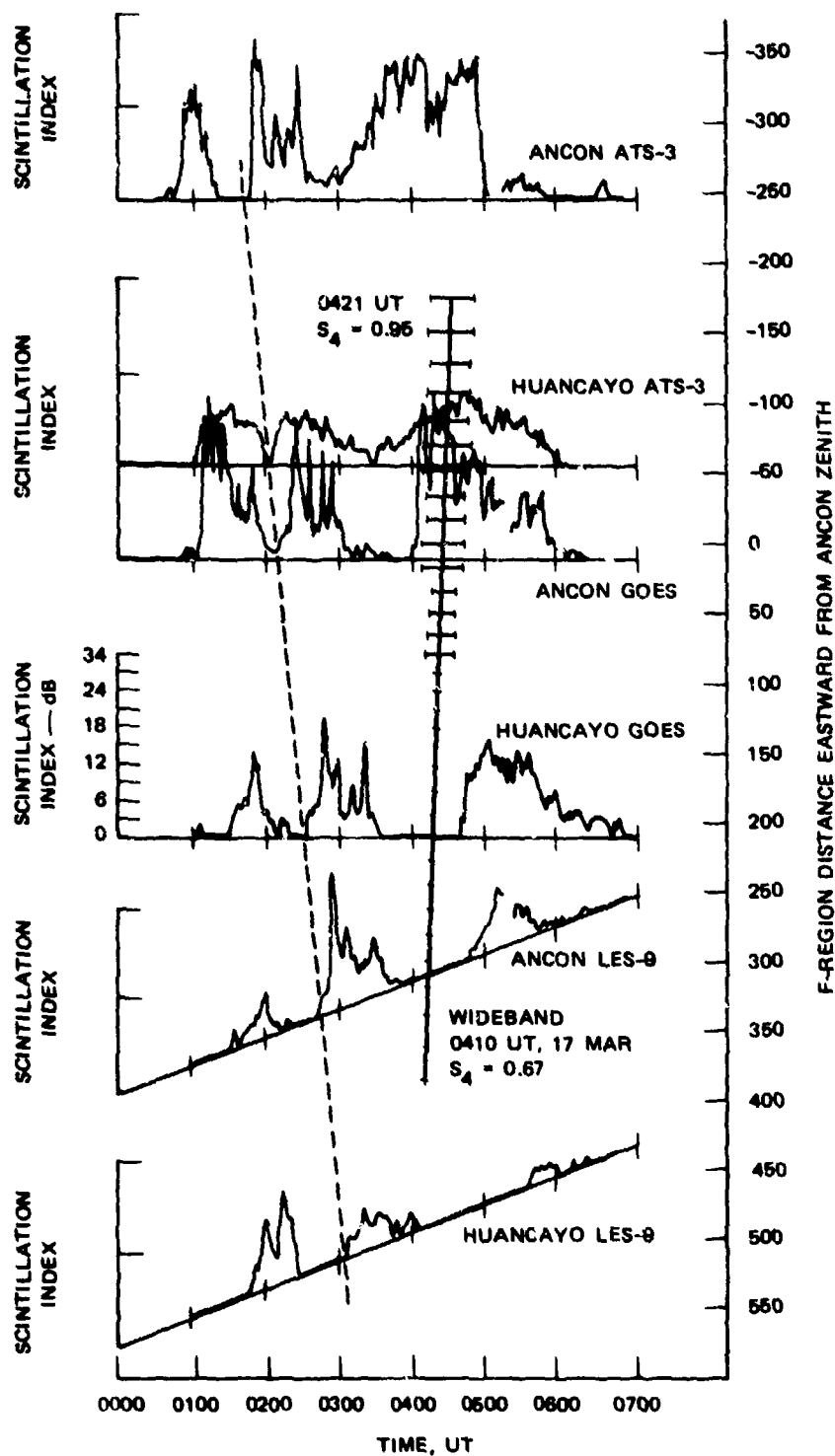
FIGURE 44 CASE STUDY 1 SCINTILLATION INDICES MEASURED FOR VARIOUS
PROPAGATION PATHS FROM ANCON AND HUANCAYO PLOTTED
AGAINST TIME AND F-REGION INTERSECTION DISTANCE FROM
ANCON

78
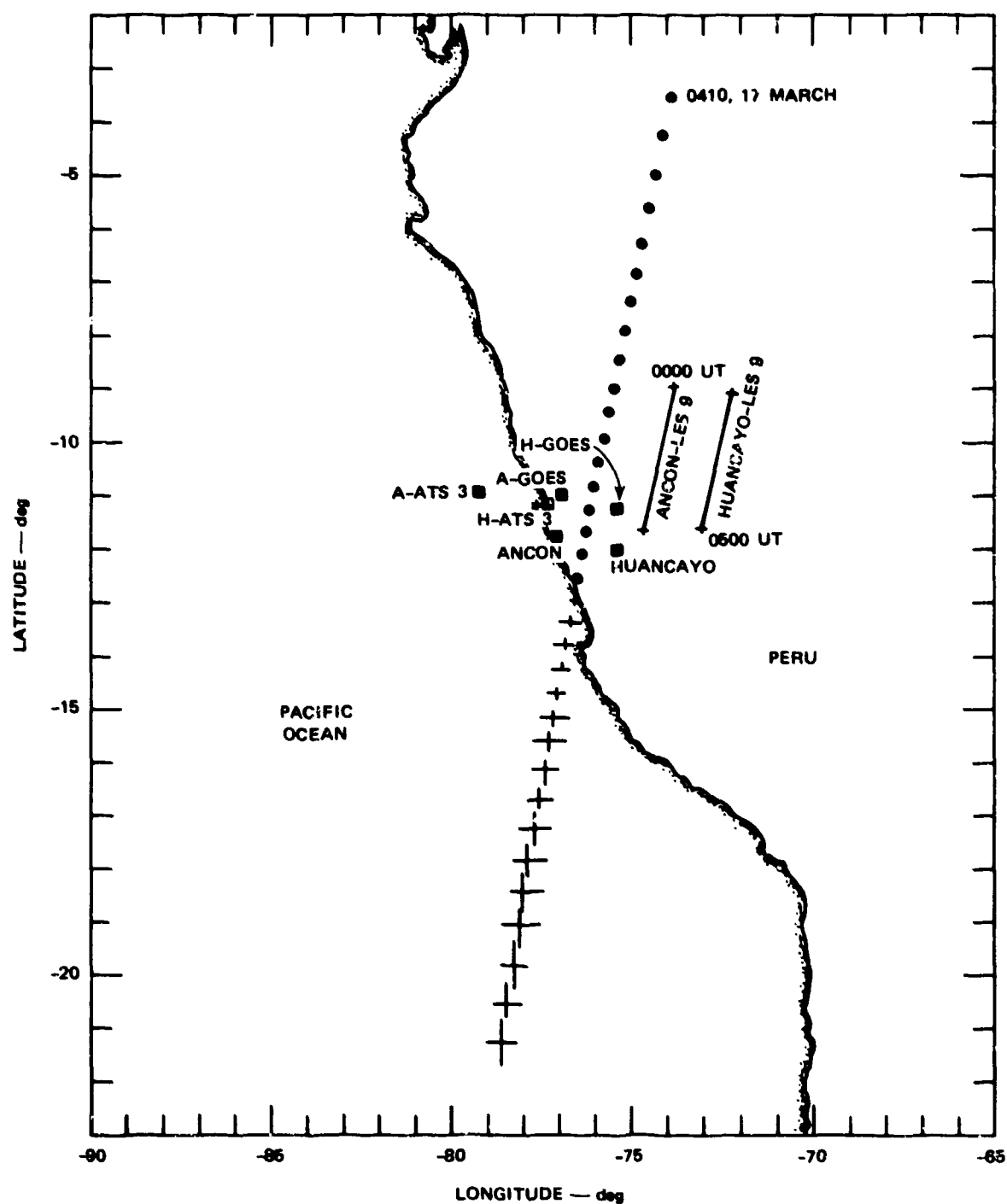
FIGURE 45 CASE STUDY 1 INTERSECTION POINTS FOR COORDINATED OBSERVATIONS
OF GEOSTATIONARY SATELLITES AND RELATED WIDEBAND PASS TRACK,
ILLUSTRATING GEOGRAPHIC EXTENT OF BOTH DATA FORMS

79

scintillation records will help describe the lifetime of irregularity structures. The Jicamarca radar data will, of course, also contribute to such a study.

Some general observations about the Wideband data from the campaign period are possible, as follows:

(1) The daytime data are uniformly very quiet, although day-time scintillations are most probable in March.

(2) Scintillations observed at night are characterized as extremely strong or very quiet.

(3) The spatial boundaries of the disturbed regions are sharp, as shown by patches of intense activity in a very quiet background.

(4) Scintillations are observed for many nights in sequence interspersed with periods of several quiet nights.

(5) Wideband passes do not always reveal activity when it is present in the form of moving patches.

(6) The expected strong seasonal variation in scintillation activity is confirmed by the Wideband data.

The sequence of active and quiet days suggests that some mechanism either builds or suppresses irregularities over a period of days. The geomagnetic field may be such a coupling mechanism. A rough comparison with magnetic activity shows a possible anticorrelation between AK for College, Alaska, and maximum UHF scintillation index, S_4, at Ancon, Figure 46. (The College AK index was used since the planetary index Ap is not yet available.) When magnetic acti· · was high around March 9 through 11, scintillations were suppressed; when magnetic activity was lower between March 15 and 24, scintillations were enhanced. The graph illustrates that severe magnetic activity may suppress the scintillation mechanism for several days, and, conversely, continued low magnetic activity allows its full development. The present analysis is preliminary. The currently unavailable magnetic data (AE, DST, and Huancayo magneto-grams) should be examined in connection with the appropriately segmented but complete data set from Ancon.

Study of the equatorial/equinoctial coordinated data set has progressed beyond the routine processing to the beginnings of compari-sons. Initial correlative work will focus on three case study days.
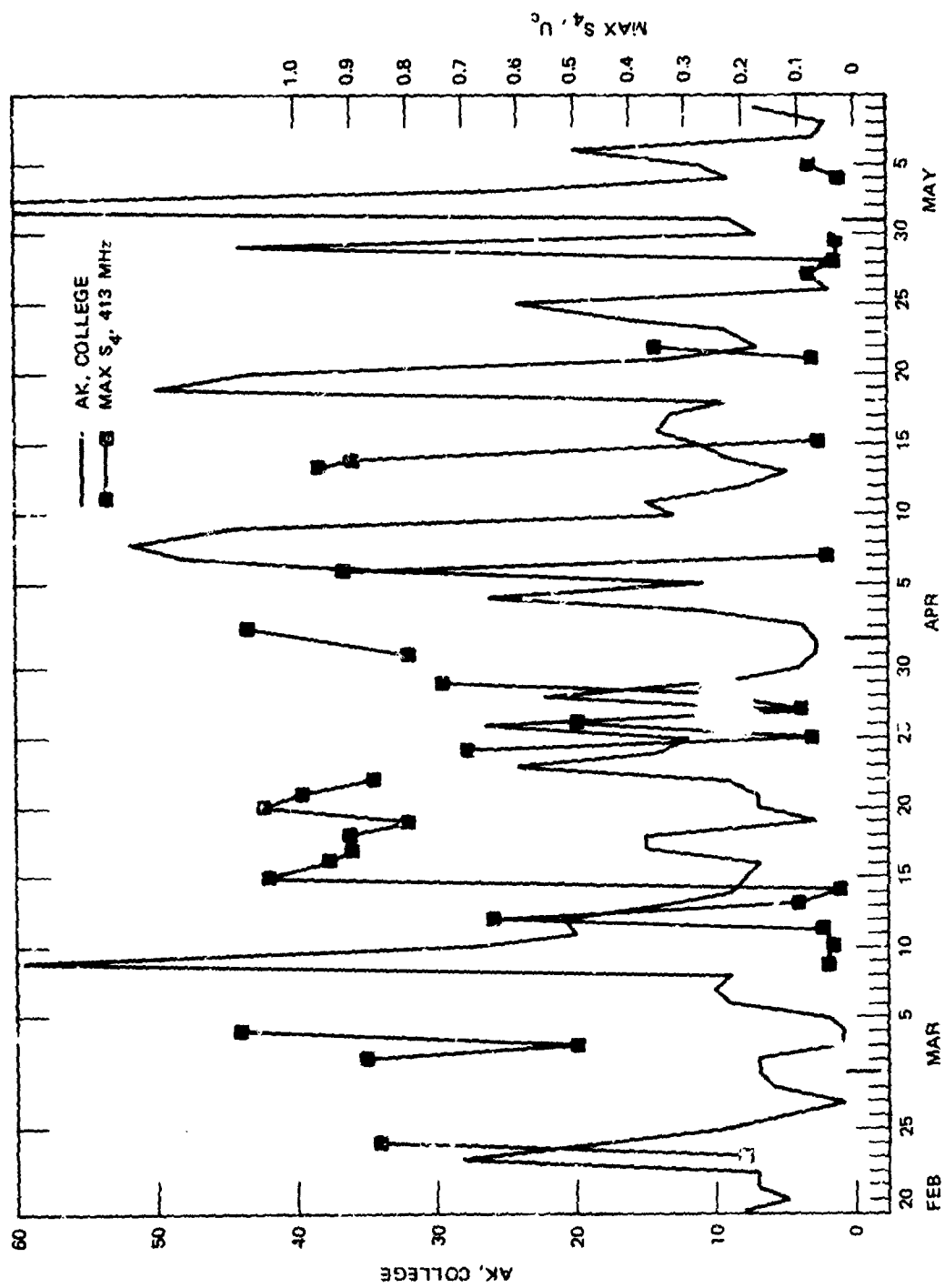
80

FIGURE 46   MAGNETIC ACTIVITY, AK FOR COLLEGE AND ANCON SCINTILLATION LEVEL, MAXIMUM S₄ AT UHF
COMPARED TO DATE

81

Already an enhanced view of the disturbed ionospheric region is at hand through the combination of orbiting and geostationary satellite data. Relating scintillations to magnetic activity and other similar physical measures may be fruitful in exposing the operational mechanisms behind equatorial scintillations. An encouraging start on the analysis of the special data set has been made.

VI CONCLUDING REMARKS

Additional data taking at the equatorial stations during the active months should help clarify the complicated seasonal dependence of the scintillation activity. Moreover, the additional data will provide more examples of gigahertz scintillation for detailed propagation studies.

Continued operation at the Poker Flat station will provide a larger data base of aurorally induced scintillation. The ramifications of the sheet model as well as the persistent exceptions that occur when a sharp TEC boundary is present need further study. In this regard, a second Wideband receiver using only one UHF and the VHF signals could be remotely located from the Poker Flat station to verify that the intense local scintillation enhancements are purely geometrical effects.

Finally, a considerable amount of work remains in studying in detail the development of intense-amplitude scintillation, its structure, and its frequency dependence. Closely related to this task is the conversion of the temporal frequency variations to true spatial irregularity structures. This demands a knowledge of both the anisotropy and drift of the irregularities. The interferometer analysis is the key to unambiguously resolving these elements.

The work must be pursued in close collaboration with other experimental data, theoretical work, and systems analysis. Ultimately one seeks a self-consistent model that can relate a simple parameterization of the irregularity structure and strength to the phase and amplitude scintillation that is actually observed.

REFERENCES

Armstrong, J. W. and W. A. Coles, "Analysis of Three-Station Inter-planetary Scintillation," J. Geophys. Res., Vol. 77, p. 4602 (1972).

Briggs, B. H., G. S. Phillips, and D. H. Shinn, "The Analysis of Observations on Spaced Receivers of the Fading of Radio Signals," Proc. Phys. Soc. London, B, Vol. 63, p. 106 (1950).

Fremouw, E. J., C. L. Rino, and R. C. Livingston, "A Two-Component Model for Scintillation," in Proc. Symp. Cospar Satellite Beacon Group, 1-4 June 1976, Boston University, Boston, Mass. (1976).

Gossard, E. E., D. B. Sailors, and V. R. Noonkestor, "Guide to Computation and Use of Cross Spectra in Geophysics and Radio Physics," Technical Document 136, Naval Electronics Laboratory Center, San Diego, Calif. (1967).

Phillips, G. J. and M. Spencer, "The Effects of Anisometric Amplitude Patterns in the Measurement of Ionospheric Drifts," Proc. Phys. Soc. London, B, Vol. 68, p. 481 (1955).

Rino, C. L. and E. J. Fremouw, "The Angle Dependence of Single Scattered Wavefields," submitted to J. Atmos. Terr. Phys. (1977).

DISTRIBUTION LIST

DEPARTMENT OF DEFENSE

Assistant Secretary of Defense
CMD, Cont, Comm & Intell
    ATTN: M. Epstein
    ATTN: J. Babcock

Director
Command Control Technical Center
    ATTN: C-312, R. Mason
    ATTN: C-650, W. Heidig
    ATTN: C-650, G. C. Jones

Director
Defense Advanced Rsch. Proj. Agency
    ATTN: Nuclear Monitoring R   ..ch
    ATTN: Strategic Tech. Office

Defense Communication Engineer Center
    ATTN: Code R820, R. L. Crawford
    ATTN: Code R410, James W. McLean

Director
Defense Communications Agency
    ATTN: Code 810, R. W. Rostron
    ATTN: Code 1018, Major Rood
    ATTN: Maurey Raffensperger
    ATTN: Code 480

Defense Communications Agency
WWMCCS System Engineering Org.
    ATTN: R. L. Crawford

Defense Documentation Center
12 cy ATTN: TC

Director
Defense Intelligence Agency
    ATTN: W. Wittig, DC-7D
    ATTN: DT-1B

Director
Defence Nuclear Agency
    ATTN: STVL
    ATTN: DDST
3 cy ATTN: TITL, Tech. Library
3 cy ATTN: RAAE
    ATTN: TISI, Archives

Dir. of Defense Rsch. & Engineering
    ATTN: S&SS (OS)

Commander
Field Command
Defense Nuclear Agency
    ATTN: FCPR

Director
Interservice Nuclear Weapons School
    ATTN: Document Control

Director
Joint Strategic Tgt. Planning Staff, JCS
    ATTN: JLTW-2
    ATTN: JPST, Captain G. D. Goetz

DEPARTMENT OF DEFENSE (Continued)

Chief
Livermore Division, Fld. Command
Defense Nuclear Agency
    ATTN: FCPRL

Director
National Security Agency
    ATTN: John Skillman, R52
    ATTN: Pat Clark, W14
    ATTN: Frank Leonard

OJCS/J-3
    ATTN: WWMCCS Eval. Ofc., Mr. Toma

DEPARTMENT OF THE ARMY

Commander/Director
Atmospheric Sciences Laboratory
U.S. Army Electronics Command
    ATTN: DRSEL-PL-SY-S, F. E. Niles

Chief C-E Services Division
U.S. Army Communications Cmd.
    ATTN: CC-OPS-CE

Commander
Harry Diamond Laboratories
    ATTN: DRXDO-RB, Robert Williams
    ATTN: DRXDO-NP, Francis N. Wimenitz
    ATTN: DRXDO-TI, Mildred H. Weiner
    ATTN: DRXDO-NP, Cyrus Moazed

Director
TRASANA
    ATTN: ATAA-SA
    ATTN: ATAA-TAC, LTC John Hesse
    ATTN: TCC, F. Payan, Jr.

Commander
U.S. Army Comm-Elec Engrg. Instal. Agy.
    ATTN: EED-PED, Ward Nair
    ATTN: EED-PED, George Lane

Commander
U.S. Army Electronics Command
    ATTN: DRSEL-PL-ENV, Hans A. Bomke

Commander
U.S. Army Foreign Science & Tech. Ctr.
    ATTN: R. Jones
    ATTN: P. A. Crowley

Commander
U.S. Army Materiel Dev. & Readiness Cmd.
    ATTN: DRCLDC, J. A. Bender

Commander
U.S. Army Missile Command
    ATTN: DRSMI-YTT, W. G. Preussel, Jr.

Commander
U.S. Army Nuclear Agency
    ATTN: MONA-WE, J. Berberet

DEPARTMENT OF THE ARMY (Continued)

Commander
U.S. Army SATCOM Agency
    ATTN: Document Control

DEPARTMENT OF THE NAVY

Chief of Naval Operations
    ATTN: OP 943, LCDR Huff

Chief of Naval Research
    ATTN: Code 461

Commander
Naval Electronic Systems Command
Naval Electronic Systems CMD Hqs
    ATTN: NAVALEX 034, T. Barry Hughes
    ATTN: PME 117
    ATTN: PME 117-T, Satellite Comm. Project Off.

Commanding Officer
Naval Intelligence Support Ctr.
        N: Mr. Dubbin, Stic 12

Commander
Naval Ocean Systems Center
    ATTN: Code 0230, C. Baggett
    ATTN: William F. Moler
3 cy ATTN: Code 2200
    ATTN: R. Eastman

Director
Naval Research Laboratory
    ATTN: Code 5430, Satellite Comm.
    ATTN: Code 7701, Jack D. Brown
    ATTN: Code 5400, HG Comm, Dir. Bruce Wald
    ATTN: Code 5465, Prop. Applications
    ATTN: Code 7700, Timothy P. Coffey
    ATTN: Code 5460, Electromag. Prop. Br.

Commander
Naval Space Surveillance System
    ATTN: CAPT J. H. Burton

Naval Space System Activity
    ATTN: A. B. Hazzard

Officer-in-Charge
Naval Surface Weapons Center
    ATTN: Code W4501, Navy Nuc. Prgms. Off.

Director
Strategic Systems Project Office
    ATTN: NSSP-2722, Fred Wimberly
    ATTN: NSP-2141

DEPARTMENT OF THE AIR FORCE

Commander
ADC/DC
    ATTN: DC, Mr. Long

AF Geophysics Laboratory, AFSC
    ATTN: PHD, John P. Mullen
    ATTN: LKB, Kenneth S. W. Champion
    ATTN: OPR, James C. Ulwick
    ATTN: OPR, Alva T. Stair
    ATTN: SUOL, Rsch. Library
    ATTN: PHP, Jules Aarons
    ATTN: PHD, Jurgen Buchau

DEPARTMENT OF THE AIR FORCE (Continued)

Commander
ADCOM/XPD
    ATTN: XPQDQ

AF Weapons Laboratory, AFSC
    ATTN: DYT, Capt L. Wittwer
    ATTN: SUL
    ATTN: DYC, John M. Kamm

AFTAC
    ATTN: TN
    ATTN: TF/Maj Wiley

Air Force Avionics Laboratory, AFSC
    ATTN: AAD, Wade Hunt
    ATTN: AAB, H. M. Hartman
    ATTN: AAD, Allen Johnson

Headquarters
Electronic Systems Division/XR
    ATTN: XRC, Lt Col J. Morin
    ATTN: XRE, Lt Michaels

Headquarters
Electronic Systems Division/YS
    ATTN: YSEV

Headquarters
Electronic Systems Division, AFSC
    ATTN: Jim Deas

Commander
Foreign Technology Division, AFSC
    ATTN: NICD Library
    ATTN: NTD, B. L. Ballard

HQ USAF/RD
    ATTN: RDQ

Commander
Rome Air Development, AFSC
    ATTN: ETEI, A. Lorentzen

SAMSO/MN
    ATTN: MNNL, Lt Col Kennedy

SAMSO/SK
    ATTN: SKA, Lt Maria A. Clavin

SAMSO/SZ
    ATTN: SZJ, Major Lawrence Doan

SAMSO/YA
    ATTN: YAT, Capt L. Blackwelder

Commander in Chief
Strategic Air Command
    ATTN: ADWATE, Capt Bruce Bauer
    ATTN: XPFS, Maj Brian G. Stephan
    ATTN: NRT

Commander
Rome Air Development Center, AFSC
    ATTN: V. Coyne, OCSE
    ATTN: EMTLD Doc. Library

DEPARTMENT OF ENERGY

University of California
    ATTN: Tech. Info. Dept. L-3

DEPARTMENT OF ENERGY (Continued)

Sandia Laboratories
    ATTN: Doc. Con. for A. Dean Thornbrough,
        Org. 1245
    ATTN: Doc. Con. for D. A. Dahlgren, Org. 1722
    ATTN: Doc. Con. for W. D. Brown, Org. 1353
    ATTN: Doc. Con. for J. P. Martin, Org. 1732

Los Alamos Scientific Laboratory
    ATTN: Doc. Con. for R. F. Taschek

OTHER GOVERNMENT AGENCIES

Department of Commerce
Office of Telecommunications
    ATTN: L. A. Berry
    ATTN: William Utlaut
    ATTN: G. Reed

NASA, Goddard Space Flight Center
    ATTN: ATS-6, Ofc. P. Corrigan

National Oceanic & Atmospheric Admin
    ATTN: C. L. Rufenach
    ATTN: Richard Grubb
    ATTN: Joseph H. Pope

DEPARTMENT OF DEFENSE CONTRACTORS

Aerospace Corporation
    ATTN: F. A. Morse, A6 Rm 2407
    ATTN: F. E. Bond, A1 Rm 5003
    ATTN: S. P. Bower
    ATTN: SMFA for PWW
    ATTN: T. M. Salmi
    ATTN: Irving M. Garfunkel
    ATTN: V. Josephson
    ATTN: J. E. Carter, 120 Rm 2209
    ATTN: D. P. Olsen, 120 Rm 2224E
    ATTN: Norman D. Stockwell

Analytical Systems Engineering Corp
    ATTN: Radio Sciences

The Boeing Company
    ATTN: Glen Keister
    ATTN: D. Murray

Brown Engineering Company, Inc.
    ATTN: Romeo A. Deliberis

University of California at San Diego
Marine Physical Lab of The Scripps
Institute of Oceanography
    ATTN: Henry G. Booker

Charles Stark Draper Laboratory, Inc.
    ATTN: J. P. Gilmore, MS 63
    ATTN: D. B. Cox

Computer Sciences Corporation
    ATTN: H. Blank

COMSAT Laboratories
    ATTN: R. R. Taur

Cornell University
Department of Electrical Engineering
    ATTN: D. T. Farley, Jr.

DEPARTMENT OF DEFENSE CONTRACTORS (Continued)

ESL, Inc.
    ATTN: C. W. Prettie
    ATTN: James Marshall
    ATTN: V. L. Mower
    ATTN: J. Roberts

Ford Aerospace & Communications Corp.
    ATTN: J. T. Mattingley, MS X22

General Electric Company
Space Division
    ATTN: M. H. Bortner, Space Sci. Lab.

General Electric Company
TEMPO-Center for Advanced Studies
    ATTN: B. Gambill
    ATTN: Tim Stephens
    ATTN: Mack Stanton
    ATTN. DASIAC
    ATTN: Warren S. Knapp
    ATTN: Don Chandler

General Electric Company
    ATTN: F. A. Reibert

General Research Corporation
    ATTN: John Ise, Jr.
    ATTN: Joel Garbarino

Geophysical Institute
    ATTN: T. N. Davis
    ATTN: Neal Brown
    ATTN: Technical Library

GTE Sylvania, Inc.
Electronics Systems GRP-Eastern Div.
    ATTN: Marshal Cross

Harris Corporation
Harris Semiconductor Division
    ATTN: Carl F. Davis, MS17-220

HSS, Inc.
    ATTN: Donald Hansen

University of Illinois
Department of Electrical Engineering
    ATTN K. C. Yeh

Institute for Defense Analyses
    ATTN: J. M. Aein
    ATTN: Ernest Bauer
    ATTN: Joel Bengston
    ATTN: Hans Wolfhard

Int. Tel. & Telegraph Corporation
    ATTN: Technical Library

Jaycor
    ATTN: S. R. Goldman

Johns Hopkins University
Applied Physics Laboratory
    ATTN: John Dassoulas
    ATTN: Document Librarian
    ATTN: Thomas Potemra

Linkabit Corporation
    ATTN: Irwin Jacobs

DEPARTMENT OF DEFENSE CONTRACTORS (Continued)

Lockheed Missiles & Space Co., Inc.
ATTN: Dept 60-12
ATTN: D. R. Churchill

Lockheed Missiles and Space Co., Inc.
ATTN: Richard G. Johnson, Dept 52-12
ATTN: Martin Walt, Dept 52-10

M.I.T. Lincoln Laboratory
ATTN: Mr. Walden, X113
ATTN: Lib. A-082 for David M. Towle
ATTN: D. Clark
ATTN: James H. Pannell, L-246

McDonnell Douglas Corporation
ATTN: N. Harris
ATTN: George Mroz
ATTN: William Olson
ATTN· J. Moule

Mission Research Corporation
ATTN: M. Scheibe
ATTN: Steven L. Gutsche
ATTN: F. Fajen
ATTN: P. Fischer
ATTN: Dave Sowle
ATTN: R. Bogusch
ATTN: R. Hendrick

The Mitre Corporation
ATTN: C. E. Callahan
ATTN: J. C. Keenan
ATTN: G. Harding
ATTN: Chief Scientist, W. Sen

Pacific-Sierra Research Corp.
ATTN: E. C. Field, Jr.

Photometrics, Inc.
ATTN: Irving L. Kofsky

Physical Dynamics, Inc.
ATTN: E. J. Fremouw

Physical Dynamics, Inc.
ATTN: Joseph ⌄. Workman
ATTN: A. Thompson

The Rand Corporation
ATTN: Cullen Crain
ATTN: Ed Bedrozian

DEPARTMENT OF DEFENSE CONTRACTORS (Continued)

R & D Associates
ATTN: Bryan Gabbard
ATTN: Forrest Gilmore
ATTN: William B. Wright, Jr.
ATTN: William J. Karzas
ATTN: Robert E. Lelevier

Raytheon Company
ATTN: Barbara Adams

Science Applicat' .ns, Inc.
ATTN: Daniel A. Hamlin
ATTN: Curtis A. Smith
ATTN: E. A. Straker
ATTN: D. Sachs
ATTN: Lewis M. Linson
ATTN: Jack McDougall

Science Applications, Inc.
ATTN: Dale H. Divis

SRI International
ATTN: Donald Neilson
ATTN: Charles L. Rino
ATTN: David A. Johnson
ATTN: L. L. Cobb
ATTN: Walter G. Chesnut
50 cy ATTN: M. Baron
ATTN: Walter Jaye
ATTN: Ray Leadabrand
ATTN· G. Smith
ATTN: Alan Burns
ATTN: R. C. Livingston
ATTN: M. D. Cousins
ATTN: B. C. Fair

System Development Corporation
ATTN: E. G. Meyer

Tri-Com, Inc.
ATTN: Darrel Murray

TRW Defense & Space Sys Group
ATTN: R. K. Plebuch, Ri-2078
ATTN: Robert M. Webb, R1-2410

Visidyne, Inc.
ATTN: J. W. Carpenter
ATTN: Charles Humphrey